UNIVERSITY OF CATANIA

DEPARTMENT OF CHEMICAL SCIENCES

INTERNATIONAL PhD IN CHEMICAL SCIENCES – XXXI CYCLE

NOEMI BELLASSAI

Surface Plasmon Resonance Imaging Biosensors for Cancer Diagnosis: Detection of Circulating Tumor DNA

PhD Thesis

Tutor:

Prof. Giuseppe Spoto

PhD Coordinator:

Prof. Salvatore Sortino

Abstract

This doctoral thesis focused on the realization of Surface Plasmon Resonance Imaging (SPRI) biosensor for the rapid, simple and label-free detection of single point mutations in the KRAS gene, standard actionable cancer biomarkers for colorectal cancer, in human plasma samples. Initially, the SPRI assay included the immobilization of specific peptide nucleic acid (PNA) probes onto the gold sensor to ensure the hybridization reaction of PNA-DNA complexes. The spatially controlled immobilization of PNA probes has been obtained by injecting PNA wild-type and PNA mutated solutions into a microfluidic system coupled to SPR sensor chip. The extremely low concentration of genomic DNA required an improvement of SPRI detection capabilities, by using functionalized gold nanoparticles to amplify the hybridization signal between target analytes and corresponding PNA probes. Three representative single-point mutations, gDNA G12D, G12V and G13D, have been successfully detected.

After preliminary results of nanoparticle-enhanced SPRI assay, a mixed-charge polymer based on Poly-L-lysine (PLL) polypeptide backbone modified with an anionic peptide, connected via a nonionic OEG spacer, has been synthesized in order to achieve control over the charge distribution of PLL-coated surfaces, and thus the antifouling property. The PLL backbone has been functionalized with different percentages (y%) of maleimide-OEG-NHS ester chains (PLL-mal(y%), from 13% to 26%), and the anionic oligopeptide CEEEEE, composed of one cysteine (C) and five glutamic acids (E), with a short sequence to limit the thickness of the mixed-charge polymer antifouling coating, has been attached to the maleimide units through the thiol–maleimide Michael-type addition. The grafting density has been varied to tune the balance of charged groups at polymer backbone. PLL-mal(y%)-CEEEEE surfaces have been characterized by water contact angle and polarization modulation infrared reflection-absorption spectroscopy (PM-IRRAS). Complementary acoustic (quartz crystal microbalance with dissipation, QCM-D) and plasmonic (surface plasmon resonance imaging, SPRI) techniques have been employed to monitor the adsorption of bovine serum albumin (BSA), used as standard protein solution, and diluted human plasma samples. Hence, a new nanoparticle-enhanced SPRI assay for circulating tumour DNA (ctDNA) detection in human plasma samples using PLL-mal(y%)-CEEEEE layer as the antifouling coating has been devised. The PNA probes and the anionic peptide have been attached to the maleimide units through the thiol–maleimide reaction using a microfluidic system coupled to SPR sensor chip. The analysis of ctDNA G12D target in diluted human plasma samples (5 pg μL^{-1}), collected from cancer patients and healthy donors, has been carried out using the conjugated AuNPs system, with a minimal sampling handling to avoid any contamination and disruption of the antifouling activity of PLL-mal(y%)-CEEEEE layer. The combined use of PLL-mal(y%)-CEEEEE as the antifouling layer with functionalized gold nanoparticles for the amplification of target detection overcomes the limiting factors related to the biosensor in the clinical field and offers an excellent ctDNA discrimination in the bloodstream at attomolar level.

Questo lavoro di tesi di dottorato si è concentrato sulla realizzazione di un biosensore per la rivelazione di mutazioni puntiformi della sequenza di DNA del gene KRAS, considerato un biomarcatore standard per il cancro al colon-retto, direttamente in campioni di plasma umano applicando una procedura rapida, semplice e senza l'uso di marcatori molecolari mediante la tecnica Surface Plasmon Resonance Imaging (SPRI). Inizialmente, il saggio SPRI ha previsto un primo step di immobilizzazione di sonde molecolari ad acido peptidonucleico (PNA) sul sensore di oro per garantire la reazione di ibridizzazione (complessazione) tra le molecole PNA-DNA. È stata ottenuta un'immobilizzazione delle sonde iniettando le soluzioni di PNA wild-type e PNA mutato spazialmente controllata mediante l'uso di un sistema microfluidico accoppiato al sensore SPR. La concentrazione estremamente bassa del DNA tumorale circolante nei fluidi biologici ha richiesto un aumento della sensibilità per la rivelazione di questo target con l'analisi SPRI, ottenuto mediante l'utilizzo di nanoparticelle di oro funzionalizzate per amplificare il segnale di ibridizzazione tra gli analiti target e le sonde PNA corrispondenti. In un primo momento, il saggio SPRI è stato testato in soluzione acquosa rivelando con successo tre mutazioni puntiformi del gene KRAS, gDNA G12D, G12V e G13D.

Dopo i primi risultati ottenuti con il saggio SPRI utilizzando le nanoparticelle di oro, è stato sintetizzato un polimero a carica mista costituito da Poli-L-lisina (PLL), un polimero con struttura cationica polipeptidica modificato con un oligopeptide a carica negativa legato al PLL mediante un gruppo oligo etilenglicole spaziatore, in modo da avere un maggior controllo sulla distribuzione di carica e quindi sulla proprietà antifouling della superficie funzionalizzata. Il polimero PLL è stato modificato con differenti percentuali (y%) di catene di maleimide-OEG-NHS estere e con un oligopeptide anionico CEEEEE, formato da un residuo cisteinico (C) e cinque acidi glutammici (E) con una lunghezza di sequenza piuttosto corta per minimizzare lo spessore del polimero antifouling sul sensore SPR. Il peptide CEEEEE è stato legato covalentemente alle unità maleimmidiche mediante la reazione di Michael tiolo-maleimmide. È stato investigato un ampio intervallo di densità di grafting (PLL-mal(y%), dal 13% al 26%) per regolare il bilancio di carica dei gruppi funzionali presenti nella struttura polimerica.

Le superfici funzionalizzate con PLL-mal(y%)-CEEEEE sono state caratterizzate mediante misure di angolo di contatto e di spettroscopia di assorbimento della riflessione nell'infrarosso con modulazione della polarizzazione (PM-IRRAS). Per monitorare l'assorbimento aspecifico delle proteine sulla superficie trattata con il polimero antifouling, sono state utilizzate due tecniche complementari, quali la microbilancia a cristalli di quarzo con dissipazione (QCM-D) e la risonanza plasmonica di superficie ad immagini (SPRI) valutando l'interazione aspecifica sia dell'albumina siero bovina (BSA), usata come proteina standard, sia di campioni di plasma umano a diverse concentrazioni.

Infine, il saggio SPRI per la rivelazione di frammenti di DNA circolante con mutazioni puntiformi legate al tumore (ctDNA G12D) è stato ottimizzato combinando l'uso delle nanoparticelle di oro con un sensore pretrattato con il polimero PLL-mal(y%)-CEEEEE per assicurare le proprietà antifouling e quindi la migliore discriminazione dell'analita di interesse direttamente nel plasma umano. Le sonde PNA e il peptide CEEEEE sono stati legati covalentemente alle unità maleimmidiche mediante la reazione di Michael tiolo-maleimmide sfruttando un sistema microfluidico accoppiato al sensore SPR. L'analisi del target ctDNA G12D (5 pg μL^{-1}) in campioni di plasma umano al 10%, provenienti sia da pazienti affetti dal tumore che da donatori sani, è stata eseguita attraverso un trattamento minimo del campione biologico, in modo da evitare qualunque tipo di contaminazione del campione e alterazione dell'attività antifouling del film PLL-mal(y%)-CEEEEE, utilizzando nanoparticelle di oro funzionalizzate per l'amplificazione del segnale SPR a seguito della reazione di ibridizzazione PNA-DNA. L'uso combinato del PLL-mal(y%)-CEEEEE, come polimero antifouling con nanoparticelle di oro funzionalizzate per la rivelazione del target di interesse supera i fattori limitanti legati all'applicazione dei biosensori in ambito clinico e diagnostico ed offre un'eccellente discriminazione per il DNA tumorale circolante nel flusso sanguigno con una sensibilità dell'ordine dell'attomolare.

Acknowledgements

The completion of this doctoral dissertation was possible with the support of several people. I would like to express my sincere gratitude to all of them.

Firstly, I am grateful to my supervisor Prof. Giuseppe Spoto for the continuous support of my PhD study and related research, for his patience, motivation, and immense knowledge. Prof. Spoto has always made himself available to clarify my doubts despite his busy schedules, and I personally consider it a great privilege to have attended my doctoral programme under his guidance and to have learnt from his research expertise.

My sincere thanks also go to Prof. dr. ir. Jurriaan Huskens, Professor of Molecular Nanofabrication group at the University of Twente in the Netherlands, who provided me with the opportunity to join his team as intern, and who gave access to the laboratory and research facilities. Without his precious support, it would not have been possible to conduct part of this PhD project. I have been delighted to have made his acquaintance, and his help supported me all the time of research and writing of this thesis.

Besides, I would like to thank Dr Roberta D’Agata for her insightful comments and encouragement which urged me to widen my research from various perspectives. With her experience and her love for the scientific research, she passed down to me the desire to persevere in my project during the doctoral studies.

A very special gratitude goes out to Prof. Carmelo Sgarlata for his valuable guidance, personal and scholarly inputs and consistent encouragement I received throughout all of my PhD experience.

I would like to thank the Horizon 2020 Health project “ULTRAPLACAD” (n. 633937) for financial support, and the Erasmus plus programme for the research stay at the University of Twente.

I thank my lab mates and friends in the University of Twente, Daniele Di Iorio and Jacopo Movilli, for the stimulating discussions, for their support during the research work at the University, and for all the fun we had during the internship in The Netherlands.

Also, I thank my colleagues and friends at the University of Catania Rossella Migliore, Dr Giusy Grasso, Dr Valentina Oliveri, Vanessa Jungbluth, Dr Valentina Giglio, Dr Maria Chiara Giuffrida and Mrs Tosto (the PhD secretary), who have all extended their support in a very special way. I gained a lot from their personal and scholarly interactions, their suggestions on my research programme.

Last but not least, I would like to thank my parents because I owe it all to them.

My mother, my life-coach, has always been keen to know what I was doing and how I was proceeding, although it is likely that she has not always grasped deeply what it was all about! She always joined with me whenever a significant momentous was reached but, obviously, she has not ever missed the opportunity to remind me never to neglect my health and my happiness before the academic job.

My father has always encouraged me in difficult situations during these years by passing me down his calm and patience. Many Thanks!

I am also grateful to my other family members and friends who have supported me along the way.

Thanks for all your encouragement!

Ringraziamenti

Vorrei esprimere la mia più sincera gratitudine a tutti coloro che mi hanno sostenuto nella realizzazione di questa tesi di dottorato.

In primo luogo, vorrei ringraziare il mio tutor Prof. Giuseppe Spoto per aver continuamente incoraggiato i miei studi e le mie ricerche scientifiche all’interno del programma di dottorato, per la sua pazienza, motivazione e immensa conoscenza. Il Prof. Spoto si è sempre messo a disposizione per chiarire i miei dubbi nonostante i suoi impegni e, personalmente, considero un grande privilegio aver frequentato il mio programma di dottorato sotto la sua supervisione e aver imparato molto dalla sua esperienza di ricerca scientifica.

Un sincero ringraziamento va al Prof. dr. ir. Jurriaan Huskens, professore del gruppo di Molecular Nanofabrication presso l'Università di Twente nei Paesi Bassi, che mi ha dato l'opportunità di unirmi al suo team come studente con libero accesso al suo laboratorio e alle strutture di ricerca. Senza il suo prezioso supporto non sarebbe stata possibile la realizzazione di parte di questo progetto di dottorato. Per me è stato un onore aver fatto la sua conoscenza e il suo prezioso aiuto mi ha accompagnato per tutto il tempo della ricerca e di scrittura di questa tesi.

Inoltre, vorrei ringraziare la dott.ssa Roberta D'Agata per i suoi perspicaci commenti ed incoraggiamenti che mi hanno spinto ad ampliare i miei studi in diversi ambiti. Con la sua esperienza e il suo amore per la ricerca scientifica, mi ha trasmesso il desiderio di perseverare nel mio progetto di ricerca.

Una speciale ringraziamento va al Prof. Carmelo Sgarlata per la sua preziosa guida, per gli input personali e accademici e per il costante incoraggiamento che ho ricevuto durante tutta la mia esperienza di dottorato.

Desidero ringraziare il progetto Horizon 2020 “ULTRAPLACAD” (n. 633937) per il supporto finanziario e il programma Erasmus plus per il periodo di ricerca eseguito presso l'Università di Twente.

Ringrazio i miei colleghi di laboratorio e amici dell'Università di Twente, Daniele Di Iorio e Jacopo Movilli, per le discussioni stimolanti, per il loro sostegno durante il lavoro di ricerca presso l'Università e per tutte le divertenti esperienze che abbiamo vissuto durante lo stage in Olanda.

Ringrazio anche le mie colleghe e amiche dell'Università di Catania, Rossella Migliore, la dott.ssa Giusy Grasso, la dott.ssa Valentina Oliveri, Vanessa Jungbluth, la dott.ssa Valentina Giglio, la dott.ssa Maria Chiara Giuffrida e la signora Tosto (la segretaria del dottorato), che mi hanno mostrato il loro sincero sostegno in modo molto speciale. Ho ricevuto molto da loro grazie ai continui confronti, sia personali che lavorativi, e ai loro costruttivi suggerimenti sul mio programma di ricerca.

Infine, ma non meno importante, vorrei ringraziare i miei genitori perché devo tutto a loro.

Mia madre, il mio maestro di vita, ha sempre voluto sapere cosa stavo facendo e come stavo procedendo, anche se probabilmente non sempre capiva fino in fondo di cosa mi stavo occupando! Ha sempre gioito con me ogni volta che è stato raggiunto un obiettivo importante, ma ovviamente non ha mai perso l'occasione di ricordarmi di non trascurare mai la mia salute e la mia felicità davanti al mio lavoro accademico.

Mio padre mi ha sempre incoraggiato in situazioni difficili durante questi anni trasmettendomi la sua calma e la sua pazienza. Grazie infinite!

Vorrei ringraziare tutti i miei familiari e amici che mi hanno sostenuto lungo la strada.

Grazie per il vostro incoraggiamento!

Table of Contents

Introduction

Nowadays, healthcare represents a crucial challenge for the scientific community around the world. According to the latest World Health Organization (WHO) assessments, cancer is the most frequent cause of mortality worldwide.[1] Overall, there were 14.1 million new cases and 8.2 million deaths in 2012. The most commonly diagnosed cancers are lung (1.82 million), breast (1.67 million), and colorectal (1.36 million); while the most common causes of death are associated to lung cancer (1.6 million deaths), liver cancer (745,000 deaths), and stomach cancer (723,000 deaths), respectively.[2]

The capability to early diagnose a pathological condition and, at the same time, to improve the efficacy of therapeutic treatments is the main objective for biomedical research and pharmaceutical industries.

Nanotechnology promises an exceptional pathway for personalized medicine and for the enhancement of the person's health, through the development of molecular assay for the detection of specific genetic information, such as tumour-linked genetic alterations. Especially for cancer disorder, the real challenge of personalized medicine is to consider the evolution of the disease integrally by examining all primary tumour and metastatic sites, parting on the principle that tumours are heterogeneous at molecular level, including cellular morphology, gene expression, metabolism, motility, proliferation, and metastatic potential, and different samples of a tumour might yield different results. Heterogeneity can occur both between tumours of the same type in different patients (inter-tumour heterogeneity) as well as between cancer cells within a tumour (intra-tumour heterogeneity).[3] The standard analysis based on tissue biopsy would underestimate the complexity of the genomic overview of the tumour, and it would provide discordant information about the efficacy and possible acquired resistance after pharmacological therapy.

Above all, optical biosensors have been profiled as reliable and efficient analytical tools offering rapid, simple and highly sensitive detection of disease-related molecular biomarkers.

In order to accelerate the technology-transfer process of biosensors to the medical field, considerable research efforts must be addressed to create and optimize the biofunctionalization and the assay procedures, which permit reliable and accurate detection of relevant biomarkers directly in biological fluids and, essentially, avoiding any pretreatment of the sample. The development of versatile and fully optimized biosensor methodologies might indicate a breakthrough for early cancer diagnosis and, thereby, for personalized medicine.

Biosensors and biomedical devices require antifouling surfaces to prevent the non-specific adhesion of proteins or cells, for example, when aiming to detect circulating cancer biomarkers in complex natural media (e.g., in blood plasma or serum). The study of protein–inorganic surface interactions is crucial to the rational design of new tools for biomaterials science, biosensing, nanobiotechnology and nanomedicine. Nonspecific adsorption of proteins, well-known as protein fouling effect, can affect surface properties of biomaterials and trigger the degradation of devices operating in contact with biological fluids. When a solid comes in contact with a body fluid such as blood, plasma or serum, a layer of proteins is formed on the surface of the solid material within a time frame of seconds to minutes. For sensors, this may cause functional device interference, possibly preventing the detection of biological targets available at low concentrations in complex media (down to the ng L^{-1} region, or a difference of nine orders of magnitude).[4,5] This, unfortunately, may lead to the occurrence of “false positive” results due to the incorrect interpretation of the biosensor response as originating from an unaffected binding event.[4,6] On the other hand, “false negative” results might also occur if analyte binding is prevented. Both these situations, understandably, create serious clinical dangers.[4]

To relieve this major technical difficulty to biosensor development in early cancer diagnosis using real clinical samples, more intensive research efforts have to be dedicated to engineer antifouling coatings capable of reducing or, ideally eliminate, non-specific adsorption of blood-borne proteins.[4,5] It has become abundantly clear that the educated design and development of antifouling/biocompatible materials for bioanalytical and biomedical applications require a prior detailed understanding of how proteins adsorb onto surfaces.

From the abovementioned, this PhD Thesis has aimed at designing and evaluating an innovative biosensor methodology improving the performance of nanoplasmonic biosensors in the early clinical diagnosis of cancer disease. Specifically, the main objectives outlined for this work involve:

1) Assessment and optimization of biofunctionalization strategies that improve the analytical features of the assay in terms of selectivity and reproducibility;
2) Design of methodologies for prevention and minimization of protein fouling, coming from complex biological matrices such as human plasma;

3) Validation of the accuracy and reliability of the proposed strategies with the nanoplasmonic biosensors employing real clinical samples.

This research project was performed in collaboration with Prof. dr.ir. Jurriaan Huskens' group, at the Molecular Nanofabrication group, University of Twente, Enschede (The Netherlands) as visiting Erasmus PhD student.

Chapter I

Biosensors for Medical Diagnostics

This chapter describes the role of biosensor devices as diagnostic tools in the clinical field. After a brief review of biosensor technologies, plasmonic and mechanical biosensors are defined, pointing out their advantages and limitations for the clinical practice. Special attention is given to the properties and requirements of the biorecognition layer to achieve optimal biosensor performance, especially SPR and QCM-D platforms, for biomarkers detection in early cancer diagnosis.

I. Biosensors for Medical Diagnostics

Diagnostics play a crucial role in medicine for the successful prevention and monitoring of disease progression. Modern medicine relies heavily on the biomolecular information for diagnosis process, which includes the detection and identification of the pathology, the definition of its burden and stage, and the choice of more suitable pharmacological treatment. Moreover, monitoring of the therapeutic response and continuous follow-up of pathologies or physiological states, during and after treatments, are critical aspects to improve patient's health.

Nowadays, clinical diagnosis is based on highly sensitive and specific laboratory assays such as cell culture methods, polymerase chain reaction (PCR) or enzyme-linked immunosorbent assays (ELISA), which are broadly applicable to different classes of biomolecules and were designed to be highly efficient for processing relatively large numbers of samples. These conventional methods involve laborious, multi-step and time-consuming procedures such as 1) the complex sample protocol; 2) the slow turnaround time (days for DNA sequencing, hours for PCR-related approaches),[7] 3) relatively large volume input requirements (approximately 1 mL of biofluids),[8] 4) the introduction of potential sources of bias owing to sample contamination and PCR errors,[9,10] 5) relatively high costs per analysis. Additionally, these medical diagnostic technologies require fully equipped laboratories and specialized personnel to perform the analysis, curbing the accessibility of these techniques to large centres and often at the expense of lower speed of analysis.

More recently, microarray technology is offering a highly efficient option for simultaneous identification and determination of a broad range of biomolecules. Microarray substrate is composed of regular patterns of DNA sequences or proteins, attached to a solid support, able to bind complementary nucleotide sequences, to detect mutations or relevant protein biomarkers in a sample using fluorescence labels. Although this technology began in the 1980s, recent advances in nanomaterials and nanofabrication techniques improved the multiplexing capabilities as well as the detection sensitivity.[11-14] Nanoarray technology proposes accurate, rapid and high-throughput screening, widely used to investigate and profile the fundamental causes of numerous human diseases and to design new therapeutic drugs.

Most promising alternative solutions for diagnosis or therapy monitoring of relevant diseases, such as allergy, celiac and diabetes diseases, neurological disorders or cancer, are expected from biosensor devices, which can offer rapid and reliable biomedical analysis,[15] by employing low sample volumes with minimum pretreatment. Biosensors would represent exceptional analytical tools for the effective clinical diagnosis as well as for better comprehension of the molecular mechanisms involved in the pathophysiology, by revealing new biomarkers useful for the evaluation of appropriate pharmaceutical treatments.

In this context, the analysis of tumor-linked genetic alterations has been used for diagnostic, prognostic and therapeutic purposes to obtain rapid and accurate cancer somatic mutation profiling. Different drugs have been used as interfering agents to slow down the proliferation of cancerous cells, and it has been demonstrated that their efficacy is related to the oncogenic mutation status of patients.[16,17] The presence or absence of specific genomic alterations indicates if the pharmacological treatment will effectively limit the spread of cancer thus improving patient survival rate. A similar testing prior to treatment serves as a useful tool for precision medicine.[18] The monitoring of oncogenic mutations is not only helpful before the therapy, but it is also relevant during and after the pharmaceutical treatment to assess the developed drug resistance and cancer recurrence.[19-21]

Initially, standard clinical protocols have been applied to evaluate the genetic tumour mutation status through the direct sampling of cancerous tissue with biopsy or surgical resection.[22] However, that approach shows limiting factors such as its invasively, inherently clinical risks, potential surgical complications and high costs.[21] Multiple or serial biopsies are often impractical and some tumors are not always available in the surgical section. Additionally, the analysis based on a single biopsy might increase the risk for seeding cancerous cells to new sites, and it would underestimate the complexity of the genomic overview of a tumour by providing discordant information about the efficacy and possible acquired resistance after pharmacological therapy.[23]

The molecular analysis would allow detecting de novo mutations which confer resistance, or mutations following the clinical treatment which may be sensitive to alternative targeted therapies. At the same time, the development of this molecular assay would enhance the monitoring of cancer patients during specific treatment, as well as the therapeutic resistance of tumour cell clones.

In light of this difficulty, early diagnosis and monitoring of pathological conditions, especially for cancer disease, through molecular biomarker analysis by biosensor platforms would significantly improve prognosis and survival rates, reducing disease burden and helping social development, opening the door to a global healthcare access.

The next section offers a complete description and classification of the biosensors also used as clinical diagnostic tools for cancer biomarkers detection.

I.2. Biosensors

I.2.1. Definition and Classification

According to the International Union of Pure and Applied Chemistry (IUPAC), a biosensor is a self-contained integrated device, able to provide specific quantitative or semi-quantitative analytical information using biosensing receptors and a transducer with a digital output.[24] The biorecognition layer, typically comprised of enzymes, antibodies or nucleic acids (DNA or RNA sequences), cells or other biomaterials, is specifically projected to interact with the target in a sample, and it is responsible for the biosensor selectivity. Also, synthetic molecular recognition elements are used for analyte detection and analysis. Those include nanomaterials or membrane structures such as molecular imprinted polymers (MIPs), aptamers, phage display peptides, binding proteins and synthetic peptides as well as metal oxides materials. When the receptor selectively recognizes a particular biological molecule through specific reactions, physicochemical variations in the medium, or on the surface, are measured by the transducer and converted into discrete or continuous signals (Fig. 1).[25]

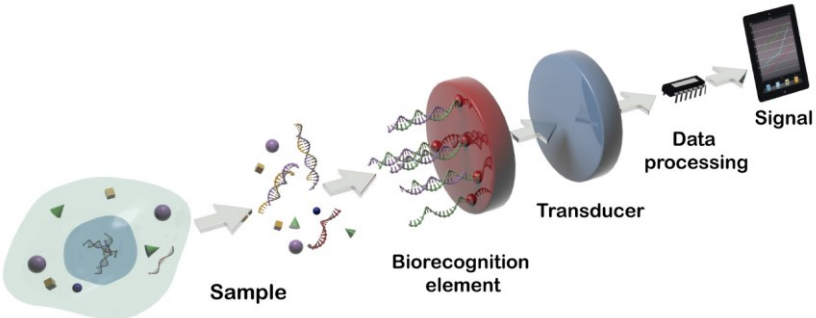

Figure 1. Schematic representation of a biosensor device. The specific biological receptor recognizes the specific analyte in the sample; the transducer measures the interaction analyte-receptor, the data processing system and the final signal can be detected. Adapted from Ref.26.

The design and integration of biosensors offer unique features to enhance the existing analysis. The combination of the bioreceptor layer with the transducer in a single device allows the rapid detection of the target analyte with high sensitivity and selectivity. Furthermore, biosensors could ideally overcome relevant disadvantages of conventional techniques, such as the need of analyte extraction or purification or the use of additional equipment for signal read-out (e.g. UV-VIS spectrometer, microscope, etc.) which requires specialized personnel.

Biosensors can also detect biological interactions in real time letting the evaluation of the affinity and kinetics of the interaction and, thereby, clarifying the biochemical mechanisms involved in the disease.[27] Biosensors also benefit from notable versatility for the measurement of a wide range of analytes just by selecting the appropriate biological receptor. Recent advances in nanofabrication further give interesting opportunities for biosensor miniaturization, high-throughput and low-cost production.[28,29] Biosensor platforms exhibited exceptional capabilities to develop into portable and user-friendly devices used at doctor's office or patient's home.[30,31]

Considering the nature and properties of the biochemical interaction, biosensors can be classified into two main categories: catalytic biosensors and affinity biosensors.

In **catalytic biosensors**, the recognition event involves a (bio)chemical reaction, catalyzed by the biomolecular receptor, which converts a substrate in the sample in a product (Fig. 2 (a)).[32] Most typical biocatalytic elements are enzymes, cellular organelles, microorganisms or tissues. The analyte is chemically transformed by the biorecognition element in a product detected by the transducer, such as proton concentration, light or heat emission, the release of ammonia or oxygen gasses. Catalytic biosensors have extremely high specificity and rapid response times, but they have problems related to the activity and stability of the biorecognition element.

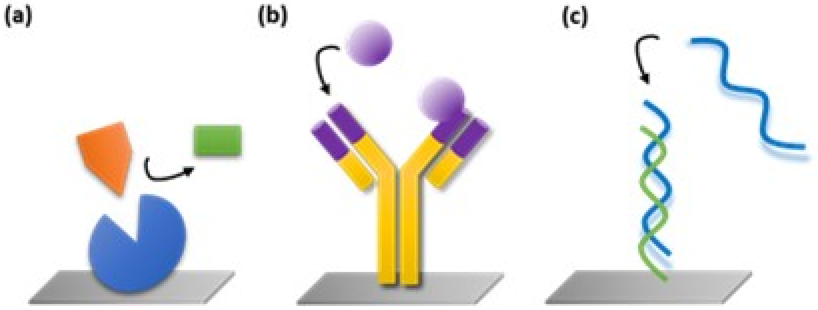

Figure 2. Main examples of biosensors depending on the biorecognition element: (a) enzymatic biosensor (catalytic), (b) immunosensor (affinity) and (c) DNA biosensor (affinity).

Affinity biosensors work through the conformational recognition between the analyte and its specific receptor leading to an equilibrium reaction.[33] The change of mass or variations in optical or electrical properties detected by the transducer can be used to estimate the interaction analyte-receptor. Usually, immunosensors are the representative example of affinity biosensors, where the interaction occurs between an antigen and its antibody (Fig. 2 (b)). DNA biosensors are also increasingly employed, and they are based on the specific interaction between complementary oligonucleotide chains (Fig. 2 (c)). In most systems, the high affinity between the analyte and the bioreceptor bestows the elevated sensitivity and specificity.

Biosensors can be also classified in relation to the transducer used in the detection for example, electrochemical, mechanical, optical, piezoelectric, thermometric or magnetic transducers.

The **electrochemical biosensors** are the most used ones in the clinical field owing to their excellent analytical features, simple and efficient production and unique miniaturization properties. In these systems, the transducer determines the electrochemical changes in the medium triggered by the biomolecular interaction.[34] Normally, the electrochemical biosensors use catalytic bioreceptors (e.g. enzymes), which provide high sensitivity and selectivity through amplification or labeling step which entails extra pretreatment or processing. Furthermore, since the detection mechanism is based on variations of the electrochemical properties, the inherent changes in biological fluids, for example, pH or ionic strength, lead to relevant interferences by deteriorating the biosensor performance.[35]

In **mechanical biosensors,** the biochemical interaction is detected by changes of mass on the surface of the transducer.[36] The acoustic-wave and nanomechanical biosensors are considered as the main examples of mechanical biosensors. In acoustic-wave devices, also indicated as piezoelectric biosensors, the transducer is a quartz crystal microbalance without a centre of symmetry, where the crystal is inserted between two electrodes carrying an alternating electrical field.[37] Changes of mass on the surface produce variations of the acoustic wave frequency which are transduced to measurable signals. Nanomechanical biosensors measure changes of mass by using micro or nanocantilevers as transducers.[38] The biological interaction arising on the surface of the cantilevers may either produce a nanomechanical deflection or variations in the vibration frequency which can be measured and quantified. Mechanical biosensors have attractive features such as label-free detection, multiplexing capabilities and thermal stability.[39] Nevertheless, the mechanical nature of the sensing mechanism is the main limitation for sample handling or when working in liquid environments.[40]

Optical biosensors measure the biological interactions by variations of the optical properties of the propagated light, such as intensity, wavelength, refractive index or polarization.[41,42] Optical sensors can be classified into two categories: bio-optrodes and evanescent wave sensors. In the bio-optrodes, the light is addressed, generally with an optic fiber, to the evaluation chamber where the biomolecular interaction induces a variation of the light properties (absorption, fluorescence, refractive index, bioluminescence or dispersion). These sensors usually utilize optical labels, such as dyes or fluorescent molecules. Conversely, the evanescent wave biosensors are based on electromagnetic (EM) wave defined in dielectric and/or metals, which can result in either a localized or propagating EM mode (Fig. 3). A part of the EM mode enters into the external medium, developing a so-called evanescent field, which acts as a probe to measure the refractive index (RI) variations due to for example a biological interaction without any label for the sensing. Interferometers, resonators or plasmonic biosensors are typical examples of evanescent wave biosensors.[43,44]

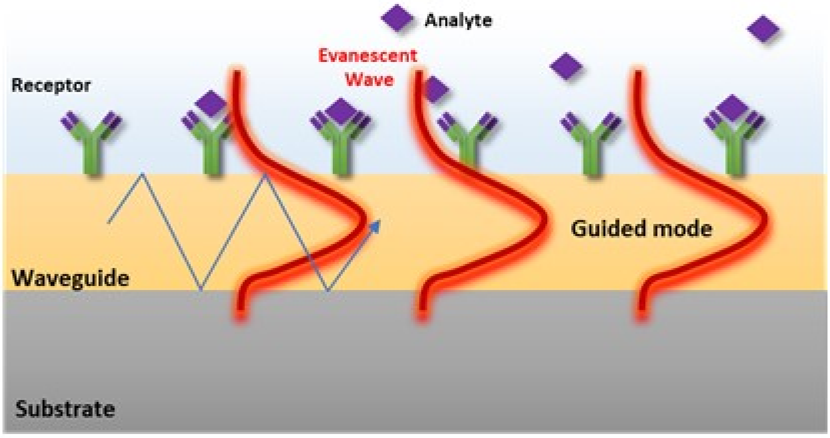

Figure 3. Schematic representation of the sensing principle of an evanescent wave biosensor.

Optical detection has long been a powerful tool for biomedical applications. Optical sensors based on bio-recognition events pose some unique advantages over other analytical methods. For example, the light beam produces much less interference to biological events compared with electronic, electrochemical or magnetic signal sources. Optical signals are immune to electromagnetic interference, capable of performing remote sensing and providing multiplexed detection within a single device. Moreover, the selectivity of the biological sensing element offers the opportunity for the development of highly specific devices for real-time analysis in complex mixtures, without the need for extensive sample pre-treatment or large sample volumes.

The optical biosensor format may involve direct detection of the analyte of interest or indirect detection through optically labelled probes, and the optical transducer may detect changes in the absorbance, luminescence, polarization, or refractive index. Some optical techniques, such as fluorescence, have intrinsic amplification in which a single label can lead to a million photons. Surface-enhanced techniques such as surface-enhanced Raman scattering (SERS) from molecules located near metallic nanoparticles allow sensing of small concentrations and the ability to recognize specific analytes in the sample. Additionally, some optical techniques, such as Surface Plasmon Resonance (SPR) and null ellipsometry, are zero- or black-background techniques: the only source of the signal is due to the presence of the analyte species, thereby enabling high-sensitivity measurements. More recently, SPR-based methods have demonstrated to be a powerful tool for the simple, rapid and cheap nucleic acids and proteins detection.[45-48] Large efforts have been paid during the last decade with the aim to develop even more sensitive and specific devices for the direct detection of genomic DNA. For example, surface plasmon resonance (SPR) biosensors have been employed for highly sensitive detection of DNA sequences,[49-51] revealing an attomolar concentration for non-amplified human genomic DNA with point mutations.[52]

In the following section, the physic-chemical properties of plasmonic and mechanical biosensors and their benefits for the development of potential devices for cancer biomarkers diagnosis in the clinical field will be described.[53-57]

I.3. Surface Plasmon Resonance (SPR)

SPR is a quantum optical-electrical phenomenon arising from the interaction of light with the free electrons at the metal surface.

Under certain specific resonance wavelength of light, the energy carried by photons is transferred to collective excitation of electrons, called *plasmons*.[58] Surface plasmons are strongly localized electromagnetic waves that propagate along the interface between the metal and the ambient medium and decay exponentially with penetration distance into an emergent dielectric medium.

The concept of plasmon begins with Maxwell's theory: the free electrons of a metal are treated as an electron liquid (density of about 10^{23} cm^{-3}) called "plasma". Electron density fluctuations propagate through the volume of a metal with a characteristic frequency given by:

$$\eta\omega_p = h\sqrt{\frac{4\pi ne^2}{m_e}} \qquad \textbf{Eq. 1}$$

where *p* is the frequency associated to plasmon oscillations, *n* is the free electron density of the material, *e* is the electron charge, and m_e is the effective mass of an electron. When the plasma is excited by an external source with a frequency equal to *p*, electrons collectively and coherently oscillate in the metal.[59]

Electrons can generate coherent fluctuations called surface plasmons (SPs). They are confined between a metallic surface and a medium with dielectric constant ε_2 and then vanish both sides of the metal surface. Surface plasmon waves are p-polarized and are described by a wave vector K_x parallel to the x direction, with an energy equal to 2.28 eV for gold surface:

$$K_x = \frac{\omega}{c}\sqrt{\frac{\varepsilon_1\varepsilon_2}{\varepsilon_1 + \varepsilon_2}} \qquad \textbf{Eq. 2}$$

where $\varepsilon_1 = \varepsilon_1' + i\varepsilon_2''$ *is* the complex dielectric constant of the metal, and ε_2 is the dielectric constant of the medium.

The wave vector (K_x) related to SPs always is higher than the wave vector of light (K_{light}) having the same energy $\hbar\omega_p$ and travelling through the medium ε_2:

$$K_{light} = \frac{\omega}{c}\sqrt{\varepsilon_2} \quad \textbf{Eq. 3}$$

For plasmon excitation by a photon to take place, the energy and the momentum must both be conserved during the photon-plasmon coupling. This condition is verified when the wave vector K_{light} and K_x are equal in magnitude and direction for the frequency of both waves. The direction of the wave vector is the direction of the wave propagation, while its magnitude depends on the dielectric constant of media at the interface.

As can be deduced easily, even from the dispersion curve below (Fig. 4), the equations (2) and (3) can never equalize, thereby it is not possible to obtain a resonant coupling with surface plasmons by irradiation direct metal with electromagnetic radiation.

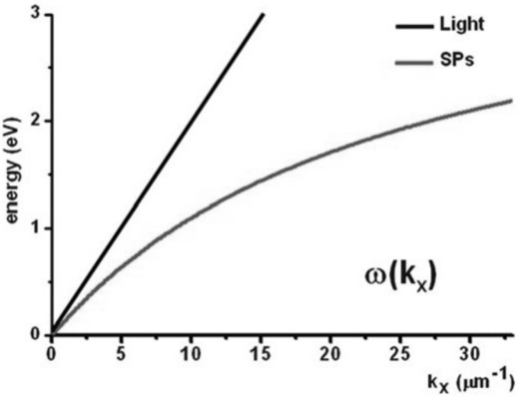

Figure 4. Plasmon dispersion curves (right) and straight dispersion of a radiation (left) that propagates in a medium. The vertical axis is scaled as ω (eV). The straight solid line in the figure shows the light line $K_x = {}^{\omega}/_{c}\sqrt{\varepsilon_2}$

Furthermore, from the analysis of the graph, it shows that for the same energy surface plasmons always have a wave vector with greater module than that of the light radiation. Therefore, the excitation of the surface plasmon needs particular coupling with the incident radiation.

The most commonly used methods for surface plasmon excitation exploit the attenuated total reflection (ATR) effect. Among the main experimental configurations, Kretschmann geometries (Fig. 5) represents a useful method for satisfying the resonance coupling.[60]

ATR configurations increase the wave vector of the radiation travelling through an optically denser medium. For example, Kretschmann configuration uses a prism (ε_{pr}) with a thin (about 50 nm for gold) metallic layer (ε_1) on one side.

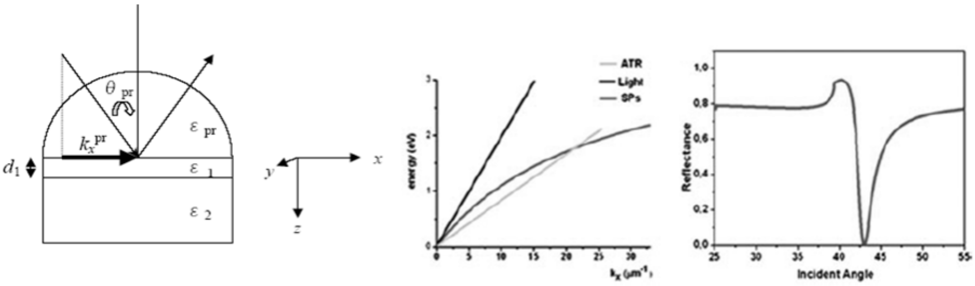

Figure 5. Configuration of the Kretschmann geometry (left); the dispersion relation of photons in a coupling prism and SPR curve for SF10 (nD1.723) |gold (50 nm, 1D0.1726Ci3.4218)|air(nD1.0) for collimated white light source (830 nm) (right).

Through Snell's law, it is possible to determine the angle of incidence θ of light beam:

$$\sin\theta = \frac{\varepsilon_1}{\varepsilon_{pr}} \qquad \textbf{Eq. 5}$$

If θ angle is equal to Eq.5, an evanescent wave is produced in the reflection point. Its intensity diminishes exponentially with penetration distance. The module of vector wave is equal to:

$$K_{pr} = \frac{\omega}{c}\sqrt{\varepsilon_{pr}}\, sen\,\theta \qquad \textbf{Eq. 6}$$

The resonance condition (Eq. 7) is satisfied when a p-polarized light beam hits the prism on a side opposite to the thin metal layer. This match produces plasmonic coupling between K_{pr} and SP wave K_x, and a drop in intensity of reflected light is observed (ATR condition) (Fig. 5, right).

$$K_{pr} = K_x \Rightarrow \frac{\omega}{c}\sqrt{\varepsilon_{pr} sen\,\theta} = \frac{\omega}{c}\sqrt{\frac{\varepsilon_1\varepsilon_2}{\varepsilon_1+\varepsilon_2}} \qquad \textbf{Eq. 7}$$

Any change of the ε_2 value caused by chemical or physical effects modifies the matching condition, and a shift in the energy position of the minimum of the reflected light (reflectance dip) is observed.

The magnitude of this shift is quantitatively related to the magnitude of the dielectric constant change (simply related to the refractive index) of the medium in contact with the metal surface.

Consequently, the SPR phenomenon can be applied to the study of processes that occur near the surface: for example, molecular interactions that occur at the interface between the metal film and the external medium. Such a distinguishing property is the basic principle which makes the surface plasmon resonance useful as a biosensor.[61-63]

The surface for SPR experiments is generally composed of a layer of gold (45 nm) deposited on a glass support with a chromium adhesive layer (5 nm).[64] The choice of gold, a metal sensor, depends on many factors such as major resistance to oxidation and other atmospheric contaminants and is sufficiently reactive to establish a surface chemistry with a wide variety of biomolecules. Also, gold is noble metal with a low imaginary part $i\varepsilon_2''$, that allows reducing the dissipation and, consequently, to obtain a narrower reflectance dip.

A surface plasmon resonance biosensor can measure the binding between target analyte molecules and receptor molecules immobilized on the gold surface. During the receptor/analyte binding event, the shift of the dip in the spectrum of reflected light is monitored over time, and kinetics information about biomolecules interactions are collected.

SPR has the potential to investigate interactions between antigens and antibodies, nucleic acid sequences and their complementary strands, and substrates and enzymes with no need for labeling of the interacting components. The kinetic events at the metal surface, displayed as a sensorgram (Fig. 6), can be investigated by monitoring the SPR signal change as a function of time. Generally, three phases can be defined during SPR experiment: the association phase where the analyte interacts with the surface bound receptor; the dissociation phase in which the analyte interaction is termed. A steady-state condition is reached when the association rate equals the dissociation rate.

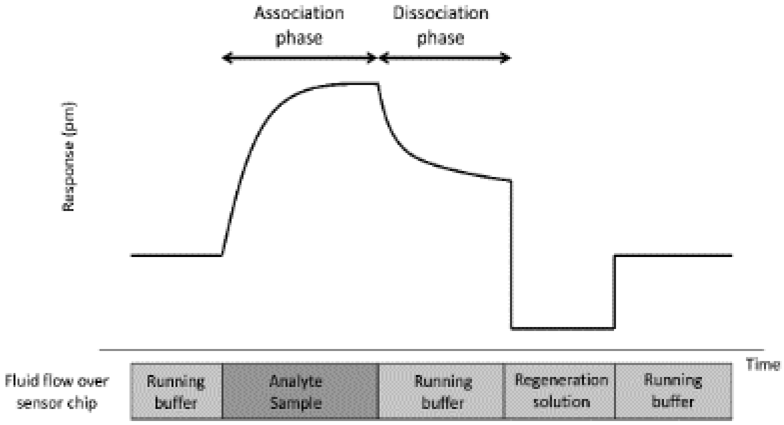

Figure 6. A pictorial description of the receptor-analyte interaction: the analyte is captured by receptors immobilized on the sensor surface. A sensorgram with the steps of an analysis cycle is also shown.

It also needs to observe how the system response is proportional to the concentration of the analyte in the solution. Therefore, the SPR technique can be used as a quantitative technique. The sensitivity of this method is such as to detect the amount of analyte up to the order of nanograms. Moreover, the interaction between analyte and receptor can be monitored through dynamic studies and binding forces. Thanks to the analysis of SPR experiments for the interaction of biomolecules, the association and dissociation rate constants (k_a) and (k_d) can be determined. Also, their ratio allows defining the affinity constant ($K_A = k_a/k_d$ or $K_D = k_d/k_a$) for the equilibrium reaction. This information is acquired by different mathematic approaches, such as linear regression, for the measurements obtained by sensogram.[65]

I.3.1.Surface Plasmon Resonance Imaging (SPRI)

The physical principle of Surface Plasmon Resonance Imaging (SPRI) is similar to the SPR methodology, but it takes another step forward. SPRI combines typical advantages of the traditional SPR in terms of real-time analysis, no label requirements and high sensitivity, with those associated to an imaging system such as the easy coupling with microfluidic devices, the high spatial resolution and the possibility to adopt an array-compatible detection approach. It was tested for the first time in 1988 by Knoll and Rothenhäusler; however, during the last two decades, it has been further developed for the study of interactions between systems such as DNA/DNA, RNA/DNA, protein/DNA, RNA/protein, antibody/antigen. [66-69]

SPRI measures spatial differences in the intensity of the reflected light (expressed as percentage of reflectivity %R) at a fixed angle and wavelength.[70] In detail, SPRI platforms based on a Kretschmann configuration employ a p-polarized light beam to hit a prism/thin gold film assembly at a fixed incident angle. The intensity of the reflected light is detected through a 2D detector (CCD), to generate an SPR image. The spatially resolved surface functionalization of the metallic SPRI surface allows detecting in real time parallel interaction events.[71-73]

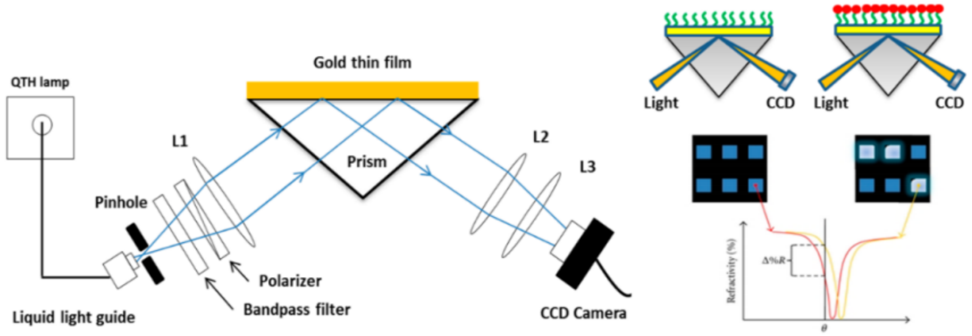

Figure 7. The general principle of surface plasmon resonance imaging (SPRI). (Left) The analyte-ligand interaction shifts the SPR curve towards a higher angle (red to orange (Right)). Due to the measurement confinements (fixed wavelength and angle of incidence θ), changes in the reflectivity (Δ%R) at a single spot of the array can be simultaneously detected. Adapted from Ref.74.

The spatial contrast in an SPR image derives from the heterogeneity in the dielectric constant, owing to differences in refractive index or film thickness at different positions within the surface. If an analyte adsorbed has a refractive index different from that of the buffer solution, the phenomenon on the surface can be detected with a spatial resolution by controlling changes in the reflected light intensity.

For small modifications in the SPR angle, the variations in reflected intensity are proportional to changes in the effective refractive index, thickness or surface coverage of a monolayer on the SPR-active surface.[75] The proportionality factor can be determined by determining SPRI intensity versus angle curves from different points of an SPRI surface. Either side of the minimum show nearly linear regions. These latter are referred to as “linear regions” or “high-contrast angles”, where the slope is high and remains constant. If the angle of incidence is set in correspondence with the linear region on the left side of the minimum, the reflectivity decreases when the minimum shifts to higher angles; if the intensity of reflected light is monitored at an angle in the linear region on the right side of the minimum, the measured reflectivity increases. The relationship remains linear for variations in reflectivity by 20%; for variations in the larger the curve becomes non-linear indices of refraction and it could have a saturation of signal.

SPRI system allows simultaneous and independent measurements on different points of the same sensor surface. In addition, the sensor surface can be observed in real time, thereby highlighting the force of SPRI, along with other advantages such as inherent optical sensitivity and instrumentation simplicity.

Moreover, the possibility to monitor simultaneously the kinetic curves; the use of a minimum volume of analyte in contact with different areas of sensor surface at the same time; the measurement of multi-analytes makes SPRI-method a potential candidate for the optimal construction of biosensors.

However, to take full advantage of this approach, a precise control of both the patterning of biomolecules onto the SPRI sensor surface, as well as the control of the analyte flow is obliged. In this perspective, microfluidic devices offer an SPRI-compatible convenient mean for both using small amounts of sample solutions as well as for checking the patterning of different biomolecules.

Laminar flow of fluids is induced by microscale conditions,[76] and the method with which liquids are put in contact with the SPRI sensor surface is optimized.[77] The use of microfluidic devices significantly diminishes the experiment duration and the sample utilization. In addition, diffusion distances, nonspecific interactions, and instrument drifts by internal signal referencing are reduced, thus allowing a better control over reaction conditions. [78,79]

I.3.2. Applications of SPR-based Biosensors

A wide range of applications has been developed for the use of SPR biosensors in the biomedical field. First of all, SPR has been used as a powerful tool to examine interactions between biomolecules based on affinity binding analysis of a variety of bonds, including antibody-antigen,[80] ligand-receptor kinetics,[81,82] enzyme-substrate reaction,[83] and epitope mapping.

SPR technique is often used as a complementary method to analyse conformational changes study rather than as a primary technique. This application has been used to monitor structural transition in protein-small molecule interactions,[84] proteins under diverse environmental conditions,[85] or impacts on apoptosis inducers.[69]

Another extension of SPR-based detection applications is its use in point mutation detection of unamplified genomic DNA, evaluated for the first time by using plant, bovine and human genomic DNAs.[86]

The limits suffered by SPR for the parallel detection of different probe/target interactions are overcome by SPR imaging.[87] The possibility to detect unamplified genomic DNA by using an SPRI-based multiplexed assay has been first shown by detecting the testis-specific protein, Y-encoded, (TSPY) gene located in the Y chromosome of the human genomic DNA.[88]

The enhanced sensitivity required, when unamplified genomic DNA is going to be detected, has encouraged efforts for innovative strategies for the amplification of transducer signals after the DNA detection. To achieve this aim, the use of nanoparticles has been widely investigated in combination with optical or electrochemical transducers.

Nanotechnology offers unique opportunities for creating highly sensitive innovative biosensing devices and ultrasensitive bioassays. Moreover, nano-sized devices generally allow for a faster response because mass transport occurs over smaller distances. Biointerfaces based on nanomaterials are particularly suitable for the development of improved the DNA detection assays.[89] Among metallic nanostructures nanomaterials, gold nanoparticles (AuNPs) have been so far the most useful and extensively examined for improved DNA detection, thanks to their intriguing electronic and optical properties.[77]

Also, the rise of sensitivity by using gold nanoparticles depends on three main factors: (i) an increase of the absolute mass in each binding event, (ii) a rise in the bulk refractive index of the analyte, and (iii) coupling between the Localized Surface Plasmon (LSP) of metallic nanoparticles and SPR of the sensing film.

The resonant excitation of LSPs is determined by the size, the shape, and the surrounding dielectric environment of the plasmonic nanostructure. Moreover, to achieve a successful and reproducible detection of biological targets using nanomaterials, the as-synthesized nanomaterials must be well dispersed in aqueous solution, with minimal to no aggregation, and nonspecific binding to biomolecules or substrates.

There are many published works in the literature for the detection of cancer biomarkers using SPR-based techniques.[90-92] Among the tumour-related genetic aberrations, DNA methylation represents an interesting biomarker for cancer diagnosis, because linked to tumour progression.[93] Methylation level of circulating tumour DNA (ctDNA) has been detected by SPR using, in this case, a single-stranded oligonucleotide capable to hybridize methylated DNA target by two inverted recognition ends (molecular inversion probe, MIP).[54]

In 2006, Li et al. developed a combination of surface hybridization, surface ligation and nanoparticle amplification for single-nucleotide polymorphism (SNP) genotyping in the BRCA1 gene,[94] which is one of the two major genes (BRCA1 and BRCA2) reported to be connected to breast cancer susceptibility. These two tumour suppressor genes are involved in repairing the DNA double-strand breaks that are responsible for breast cancer. Therefore, the identification of BRCA mutations is of a great relevance for prospective interventions and treatments for breast cancer patients. By using nanoparticles with oligonucleotides complementary to the ligation probe DNA aiming at enhancing the SPR signal, single mismatches of BRCA1 were successfully detected at concentrations as low as 1 pM.

More recently, a powerful tool for biosensing has been achieved by localized SPR (LSPR) approach,[95-97] where metallic nanostructures with plasmonic properties are associated with designed probes and surface architectures for ultrasensitive assays. In detail, LSPR platform has been employed for the ultrasensitive and simultaneous detection of different cancer biomarkers, namely tumour-specific mutations (E542K and E545K) and ctDNA methylation of PIK3CA gene (phosphatidylinositol-4,5-bisphosphate 3-kinase catalytic subunit alpha gene, PIK3CA).[55] This biosensor offered considerable performances in relation to sensitivity, combining the use of PNA-probe sequences for ctDNA mutations with a specific anti-5-methylcytosine monoclonal antibody (mAb) immobilized onto gold nanoparticles for the targeting of the ctDNA methylation.

Another improvement for SPR technology has been given thanks to recent studies about surface chemistry of SPR-biosensor. For example, the selectivity of the hybridization reaction with the target complementary sequence has been increased by using the surface immobilized peptide nucleic acid (PNA) probes for the detection of a single point mutation in unamplified genomic DNA.[98-100]

The surface modification, for the hybridization step, with suitable synthetic probes such as PNAs demonstrated a high rise of the detection specificity and sensitivity. Unique structural and hybridization qualities of PNAs make them superior to DNA as sequence-specific hybridization probes. PNAs are DNA mimics, in which the negative phosphate-deoxyribose backbone is substituted by a neutral N-(2-aminoethyl) glycine linkage. These synthetic probes interact with their complementary DNA sequence with a stronger binding, more quickly and more specifically than the analogous DNA.[101] The absence of the coulombic repulsion, established between the two negatively charged strands in DNA, lends the above mentioned special properties for PNA probes. PNA complexes are more thermally stable than DNA complexes and, through the nature of their backbone, less susceptible to biological degradation by nucleases, proteases, and peptidases.[102]

I.4. Quartz Crystal Microbalance (QCM)

Quartz crystal microbalance (QCM) is a nanogram sensitive technique that utilizes acoustic waves produced by oscillating a crystal quartz plate to determine the mass absorbed onto the surface. The heart of QCM operation concerns quartz's inherent property of piezoelectricity. This latter is generated by the electric charge that accumulates in certain solid materials (such as crystals, like quartz, certain ceramics, and biological matter such as bone, DNA and various proteins)[103-105] in response to applied mechanical stress. By applying alternating electric fields to the crystal, a swapping expansion and contraction of the crystal structure are induced. In today's most common QCMs a circular piece of quartz is sandwiched between two metal electrodes.

The quartz is generally handled using the so-called "ATcut" to give favourable properties relating to stability (low-temperature coefficients and a purely shear mode of oscillation). When a sufficient AC voltage is applied with a frequency close to the resonant frequency (f_0), the resonance is excited of the particular crystal. The resonant condition of the QCM occurs when the standing wave, produced by the alternating expansion and contraction, is an odd integer of the thickness of the quartz plate. Resonant frequencies of typical QCMs are on the order of MHz and the tradeoff between the frequency (relating to sensitivity) and the thickness (relating to usability) of QCMs is that the higher the resonant frequency the thinner the crystal. The common frequency (f_0) of 5 MHz has a corresponding thickness of ≈ 330 μm. QCMs became widely employed as mass balances only after the theory and experiments relating a frequency change of the oscillating crystal to the mass adsorbed on the surface had been demonstrated by Sauerbrey.[106] This linear relationship between frequency change (Δf) and mass adsorbed (Δm) is given by:

$$\Delta m = \frac{C}{n} \Delta f$$

where n is the harmonic number and:

$$C = \frac{t_q \rho_q}{f_0}$$

with t_q being the thickness of quartz, and ρ_q being the density of quartz and equals ≈ –17.7 Hz ng/cm^2 for a 5 MHz crystal.

There are three assumptions that must be satisfied for the Sauerbrey relationship to hold:

1. The adsorbed mass must be small relative to the mass of the quartz crystal;
2. The mass adsorbed is rigidly adsorbed;
3. The mass adsorbed is evenly distributed over the active area of the crystal.

Liquid application of QCM technology multiplied the number of potential applications dramatically including biotechnology and, in particular, biosensor applications.[107] The problem of the QCM to manage many liquid applications was that the liquid phase often incorporated viscous and elastic contributions to the frequency change and thus violated the assumption of the Sauerbrey equation, affirming that the mass adsorbed must be rigidly adsorbed. This difficulty encouraged the development of new methods for characterizing mass deposits with dissipative losses due to their viscoelastic property, and the elaboration of another theory for interpreting this new data.

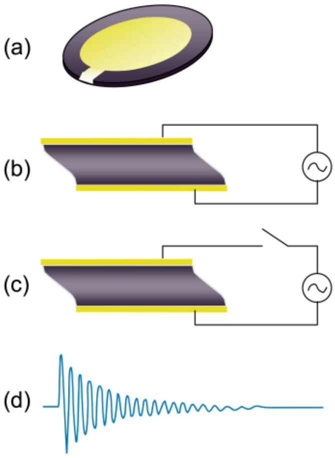

Figure 8. Description of the main components in QCM-D. (a) Typical QCM-D sensor with Au electrodes. (b) Quartz crystal with alternating current applied across electrodes. (c) Short-circuiting the alternating current. (d) The oscillatory decay as the quartz disk comes to rest. The frequency of the oscillating crystal, shown in (b), is related to the total oscillating mass adsorbed on the surface, while the energy dissipation, shown in (c), is related to the viscoelastic properties of the oscillating mass. Thus, changes in adsorbed mass of, for example, a rigid protein provide a change in frequency, but for viscoelastic masses such as biomacromolecules, there is a change both in frequency and dissipation. Adapted from Ref.108.

I.4.1. Quartz Crystal Microbalance with Dissipation (QCM-D)

Two main processes for dealing with the dissipation (*D*), due to viscoelastic film adsorption, control the reduction of a crystal's oscillation after a rapid excitation close to the resonant frequency (since the decay rate is proportional to the energy dissipation of the oscillator) or impedance analysis.[109]

QCM with dissipation monitoring (QCM-D) measures the voltage of oscillatory decay after a driving power is switched off in such a way as to ensure that the quartz oscillation has a value close to the series resonant mode.[110] The amplitude declines over time depending on the properties of the oscillator and the contact medium. The decay voltage, i.e., the output voltage amplitude as a function of time, with a frequency given by f_0 is blended with a reference frequency (f_R) and filtered with a low-pass band filter. This latter imparts an output frequency (f) based on the difference between f_R and f_0. This frequency difference is fit to an exponentially damped sinusoidal, $A(t)$, according to:

$$A(t) = A_0 e^{t/\tau} \sin(2\pi f t + \alpha)$$

where $f = f_0 - f_R$. The dissipation parameter is given by:

$$D = \frac{1}{\pi f \tau}$$

and is dimensionless, expressed as:

$$D = \frac{1}{Q} = \frac{E_{dissipated}}{2\pi E_{stored}}$$

with Q the quality factor, $E_{dissipated}$ the energy dissipated during one oscillatory cycle and E_{stored} the energy stored in the oscillating system. Resolution of frequency and dissipation in liquids is on the order of ± 0.1 Hz and 1×10^{-7}, respectively, with approximately one order of magnitude better in air or vacuum.

Typical *f* and *D* responses for protein, vesicle, or cell adsorption are on the order of 10 – 100 Hz and 1 – 10 ($\times 10^{-6}$) of dissipation units. For viscoelastic films greater than 100 nm thick, these responses are typically an order of magnitude higher. The QCM-D approach allows for determining *f* and *D* values at multiple harmonics (n = 3, 5, ...) of a resonant frequency in succession on the millisecond timescale.

The multiple harmonic data allows for treating the experimental data with a theory to extract meaningful parameters such as mass, thickness, density, viscosity, or storage modulus. The viscoelastic data permits a broader characterization of systems that do not hold the linear Sauerbrey relationship between Δf and Δm and makes QCM-D more than a simple mass balance. Moreover, associated solvent or water content of adsorbed films can be measured by comparing the mass measured using QCM-D with that of complementary techniques such as Ellipsometry or Surface Plasmon Resonance.[107]

I.4.2. Applying QCM-D technique to Biomolecular Studies

For the biomolecular applications, the dissipation parameter and the subsequently extracted viscoelastic parameters are critical for many efforts. For instance, in cellular adsorption studies, the simple QCM frequency and Sauerbrey equation would significantly undervalue the adsorbed mass of cells, since the shear wave of the oscillating quartz is reduced before even reaching the middle of the cell. The frequency penetration depth (in the z-direction away from the sensor surface) depends on the material and typically is on the order of 250 nm in water.[111] When the adsorbed mass is viscous and sufficiently soft, the system does have not the same oscillation of the crystal plate (i.e., for cell adsorption), and the internal friction (due to the deformation) in the adlayer, and thus to dissipation, is confirmed. In this case, only the dynamic mass (mass associated with water or coupled mass) is calculated. The intensity of the oscillation is directly proportional to the viscosity of the adsorbate. Therefore, monitoring cell adsorption needs using the dissipation parameter to entirely characterize the adsorption of a viscoelastic cellular structure. On the other hand, the adsorption of a small, rigid protein, although associated coupled water, may be accurately measured by controlling only frequency changes and fitting these to the Sauerbrey relation.

Usually, as the size and structural flexibility of the adsorbed molecules increase, the importance of measuring the dissipation also increases. Combined f and D measurements along with the appropriate theory can provide a way to test for a linear relationship of the simple Sauerbrey model. Furthermore, by plotting Δf versus ΔD information about the confirmation of the adsorbed materials may be extracted and to obtain the so-called reaction fingerprint described. Also, by monitoring both Δf and ΔD it is possible to quantify and separate the viscoelastic variables relating to the shear viscosity and storage modulus of the adsorbed materials. In addition. to measure both mass and viscoelastic properties of adsorbed films, one of the major advantages of QCM-D as an analytical technique is the flexibility in the choice of substrate. Basically, several materials are able to cover the QCM-D sensor chip achieving a thin layer (≈ nm to µm range). This property is important to realize specialized surfaces, monitored stepwise during preparation, obtaining particular sensors that can be used as sensor platforms for studying further biomolecular interactions. This provides a huge development platform for biological-based studies.

I.4.3. An example of QCM-D application: protein adsorption

Protein adsorption to biomaterial surfaces often plays a role in biocompatibility and can affect adverse effects are generated by the biomaterial leading ultimately to the body rejecting the implant. One of the major applications of the QCM-D is to measure the amount of protein adsorbed onto different surfaces and to understand if the material resists or promotes protein adsorption. This initial protein adsorption step can later mediate the cellular response. Therefore, adsorption of extracellular matrix proteins that can promote cell attachment, and subsequent compliance of the biomaterial, are important properties for possible biosensors. Fibronectin, an extracellular matrix protein, has been adsorbed onto layer-by-layer polymer films for developing new biomaterial coatings and then used for subsequent cell spreading measurements.[112]

Adsorption of laminin, another cell adhesive protein, has been adsorbed onto surfaces with varying surface chemistries for biomaterial development, drug delivery and diagnostics.[113] Collagen, an additional extracellular matrix protein, adsorption has been also measured on different polyester surfaces that have been hydrolyzed.[114] Three studies looked at the blood plasma protein bovine serum albumin (BSA) and additional serum proteins from fetal calf serum to promote the cellular adhesion onto either biodegradable 3-D polycarbonate scaffolds,[107] polystyrene- and UV-exposed polystyrene, or to avoid the cellular adhesion onto polyethylene glycol coatings on nanostructured SiO_2 surfaces.[108] Protein coatings of BSA and mucin have been tested to detect the effectiveness as a protective overcoat for biomaterials in terms of preventing unwanted interactions, but also promoting cellular adhesion.[115,116] Biomaterial coatings for anti-inflammatory activity have been developed using an embedded protein in a layer-by-layer architecture that allowed the protein to keep its activity. On the other hand, unwanted protein adsorption, such as that responsible for blood clotting, should be reduced in order that biomaterials do not induce clotting. Secondary selection of polymeric biomaterial candidates for fibrinogen adsorption (a protein involved in blood clotting) has been carried out to find which material had the lowest amount adsorbed and was, therefore, the best candidate for potential blood contacting medical devices.[107]

A wide variety of properties related to biosensor development by QCM-D were investigated over the past few years. The development of the magnetic-based labelling material for biosensors of a specific serum protein has been achieved using magnetic particles and assay performance by QCM-D and optical microscopy.[117] Surface development of polyethylene oxide modified surfaces and their protein resistance has been shown by QCM-D for potential use in nanostructured biosensors.[108]

A new approach for immobilizing transmembrane proteins onto surfaces for potential surface biosensor development using a proteoliposome multilayer structure was described.[118] Similarly, these examples demonstrate a way to selectively orient a membrane protein onto a functional membrane.[108,119] Bioassay development typically needs understanding the physical processes occurred between the analyte to be sensed and the sensor itself. For this reason, Au nanoparticle-protein interactions have been characterized in this application.[120] Also, antibody-antigen interactions for potential diagnostic autoimmune assays have been studied with QCM-D in this example.[121]

Central studies of protein adsorption phenomena to better comprehend protein–surface interactions have been another area with several publications. Here, adsorption of R-lactalbumin (types I and III), BSA, haemoglobin, myoglobin, cytochrome c, R-casein, and lysozyme onto model anionic citrate surfaces as a function of salt, pH, solvent, and surface conditions have been analyzed. Fouling of membrane filters for the purification of whey proteins has been examined by testing the adsorption properties of the most common whey proteins, β-lactoglobulin, onto the most common filter material, polyethersulfone. Besides just looking at fundamental adsorption processes of proteins, conformational changes of adsorbed proteins can be investigated after formation including processes such as swelling and hydration.[108]

Small molecule-protein interactions have been measured by QCM-D in a number of different studies. In this example,[122] QCM-D was used to elucidate the details of how estrogen receptors can play a role in differentially regulated genes by examining the conformation of estrogen receptor–DNA complexes.[123] Protein-polysaccharide interactions (important due to their implications to many biological processes) are another area that has been studied by QCM-D; specifically, details about the interaction between the polysaccharide pectin and BSA at varying ionic strengths have experimented.[108]

Chapter II

Circulating tumour DNA as Liquid Biopsy for Cancer

This chapter aims to comprehensively assess the diagnostic, prognostic, and predictive potential of ctDNA as a minimally invasive liquid biopsy for cancer patients. I also present an overview of current advances in the analytical sensitivity and accuracy of ctDNA analysis methods in body fluids, offered by innovative PCR-free biosensing technologies, as well as biological and technical challenges, which need to be resolved for the integration of ctDNA analysis into routine clinical practice. Among all somatic mutation forms in ctDNA, KRAS gene mutations could be an ideal candidate as prognostic and predictive biomarker for many cancer diseases.

II. An Overview of Liquid Biopsy in Cancer Diagnosis

Over the last decade, several studies have been carried out for the molecular biomarker analysis in tumour diseases by using bodily fluids.

The liquid biopsy, also known as fluid biopsy or fluid phase biopsy, consists of the detection of tumour-derived materials (e.g., cells or nucleic acids) obtained in a minimally invasive or non-invasive way through the sampling of body fluids, such as blood, plasma, serum, urine, pleural effusion, or cerebrospinal fluid.[124,125] The examination of cancer biomarkers by liquid biopsy might be used for initial diagnosis, determination of prognosis, elucidation of cancer predisposition, and predicting response to (targeted) therapy.[126,127] Through the non-invasive sampling, liquid biopsy would be more practical for real-time monitoring of disease progression than standard tissue biopsy. Moreover, the development of reliable, reproducible, and highly sensitive techniques associated with it, makes the fluid biopsy an attractive method for early cancer diagnosis.[21]

Standard clinical protocols for the evaluation of oncogenic mutations are usually based on tissue biopsy, which consists of sampling cells from the human body by puncturing organs with the use of a small-gauge needle.[22] Although tissue biopsies offer the possibility to examine the structure and the features of invasive lesions associated with the tumour, the proliferative activity of cancer cells, and the interactions between neoplastic cells and their microenvironment, this procedure represents a significant barrier for the easy and frequent monitoring of oncogenic mutations. In addition, needle biopsy can potentially introduce clinical risks for the patient, is costly and the patient’s compliance with this procedure is variable given its invasive nature as well as discomfort. A number of technical limitations have been also associated with this approach,[21] the most important of which is represented by the difficulty in accounting for tumour cells heterogeneity with the standard biopsy snapshot approach.[128] In fact, individual tumours consist of different sub-populations which are individually sampled with great difficulty by needle biopsy.[23] Other important technical limitations are that seeding tumour cell to other sites following tissue biopsy is possible and that tumours are sometimes not accessible for tissue biopsy.

The above-mentioned limitations have prompted the development of new methods for the harvesting of cancer biomarkers in a simpler and more convenient way compared to tissue biopsy. Liquid biopsy has emerged as a potential complement to traditional biopsy techniques for early cancer diagnosis.[21] Specifically, biological fluids are sampled to monitor the level of cancer biomarkers available in the chosen medium.

Peripheral blood and blood-derived products such as plasma and serum have been so far the most widely investigated media for liquid biopsy.

Different analytes with potential implications for cancer diagnosis and treatment have been found in blood. Those include circulating tumour cells (CTCs),[129] circulating membranous structures (microvesicles, exosomes) containing molecular biomarkers,[130] circulating free nucleic acids[21] (cfNAs. i.e., circulating cell-free DNA, RNA and microRNA[131]) and proteins[132,133] (Fig. 9).

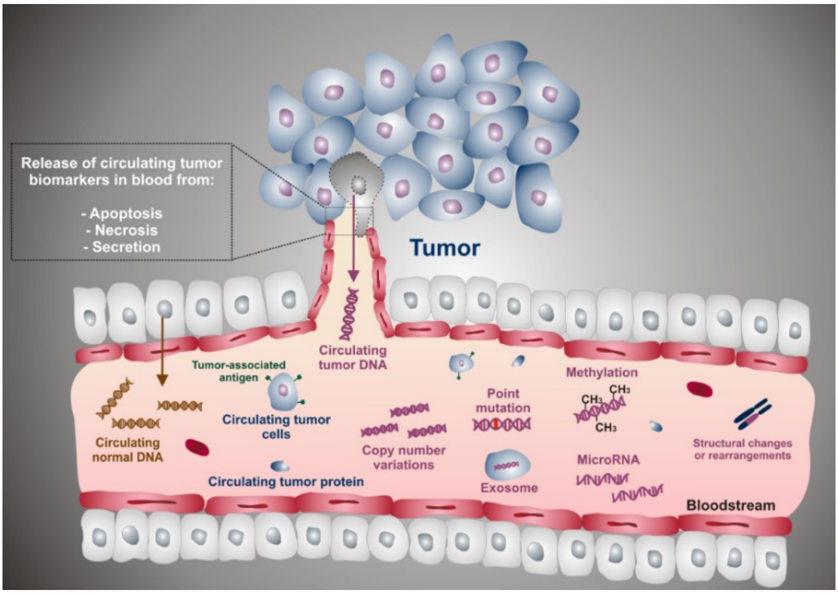

Figure 9. Schematic representation of cancer biomarkers, cells and membranous structures in circulating blood. ccfDNA is released from healthy, inflamed or diseased (cancerous) tissue from cells undergoing apoptosis, necrosis and secretion. ccfDNA can be extracted from a blood sample and, as shown in the figure, genetic mutations in the DNA released from cancerous tissue detected and quantified. From Ref.134.

In this context, circulating cell-free DNAs (ccfDNAs. i.e. DNA released from both normal and tumor cells) and circulating tumor DNA (ctDNA. i.e. DNA released only from tumor cells) offer a number of advantages which have attracted an enormous attention over the last five years resulted in CE-IVD tests available on the market starting from 2015.[135] In addition, a blood-based test for ctDNA detection has been marketed by Pathway Genomics in September 2015.[136]

The assay reached the US market with no previous U.S. Food and Drug Administration's (FDA) clearance or approval, a procedure that caused concern at FDA.

Gaining regulatory approvals from national and international agencies represents an important step toward the application of the liquid biopsy in clinical practice. So far only one assay detecting CTCs in the blood (CellSearch® CTC, Veridex, LLC) was FDA cleared in 2004 for the monitoring of patients with metastatic breast, colorectal or prostate cancer on the basis of a liquid biopsy approach. The only FDA approved assay detecting ctDNAs is called ColoGuard (Exact Sciences). It spots colon cancer–linked ctDNA from the patient stool and received FDA approval in 2014.[137]

The very limited number of FDA cleared or approved assays for liquid biopsy testifies that the new approach for cancer early diagnosis and patient monitoring is mostly confined to basic and clinical research settings. However, efforts are focusing to entering the liquid biopsy IVD market which is expected to cross US$ 1 billion mark by the end of 2020,[138] as testified by both the $100 million funded GRAIL company launched by Illumina in January 2016 as well as by the commitment of other large companies such as Johnson & Johnson, Qiagen, and Roche.

II.2. The Origins of ccfDNA and ctDNA

The presence of ccfDNA, released from both normal and cancerous cells in the human circulatory system, was reported in 1948 by Mandel and Metais,[124] but only in 1977 Leon et al.[139] discovered that ccfDNA concentration is significantly higher in the serum of patients with cancer in comparison to healthy individuals.

The first example of clinical application for ccfDNA was reported in 1997 by Lo et al.,[140] when fetal DNA sequences in maternal plasma were identified and, subsequently, used for prenatal medicine, including sex determination,[141] studies of monogenic disorders[142] and non-invasive prenatal testing (NIPT) for aneuploidies such as Down syndrome (trisomy 21).

In the 1990s, Stroun and colleagues[143,144] declared that tumour cells could release their DNA into the blood (circulating tumour DNA, ctDNA),[145] by introducing first the concept of *liquid biopsy*.

In 1991, Sidransky et al.[146] demonstrated that ctDNA secreted by cell pellets of patients with invasive bladder cancer carried mutations in TP53 (which encodes p53), and this result led to the use of genomic analysis methods in liquid biopsies.

In the following decades, ctDNA was investigated as a prognostic or predictive marker,[147,148] and for cancer detection.[149] Such studies established the potential clinical use of ctDNA, for example, the detection of KRAS mutations in plasma as a potential prognostic marker in colorectal cancer,[150] although the variation of ctDNA levels during cancer development and progression was not yet clear.

In 1999, Vogelstein and Kinzler[151] presented the digital PCR (dPCR) method able to provide an accurate identification and absolute quantification of rare mutant fragments. Moreover, using beads in emulsions[152] and flow cytometry, dPCR technology allowed the quantification of the mutant allele fraction in the plasma of colorectal cancer patients at different stages.[153] Diehl, Diaz et al.[154] then demonstrated in 2008 that ctDNA is a highly specific biomarker of tumour dynamics and could indicate residual disease after the pharmacological treatment.

The development of next-generation sequencing-based techniques has simplified the analysis of the genome at a larger scale than previously possible. In 2012, deep sequencing of multiple genes in ctDNA was employed through panels of tagged amplicons for the identification and the monitoring of multiple tumour-specific mutations in a single assay directly in the plasma of cancer patients.[155] Shortly thereafter, whole-genome sequencing (WGS) of ctDNA in plasma was used for the detection of tumour-derived chromosomal aberrations,[156] focal amplifications[157] and gene rearrangements;[158] hence, hybrid-capture sequencing method, based on the hybridization of DNA target in solution through complementary DNA sequences bound to magnetic beads, was presented as a noninvasive method for the analysis of evolving genomic profile of mutations across the entire exome in cancer.[159]

Two hypothetical, but not mutually exclusive, mechanism triggering ctDNA release in blood have been identified and classified in passive and active processes. The passive mechanism consists of the release of nuclear and mitochondrial DNA after the destruction of apoptotic and necrotic cells.[9] Under normal physiological conditions, the levels of ccfDNA are lower owing to the phagocytes, which remove all of the apoptotic and necrotic debris.[160] Nevertheless, under specific pathological conditions (e.g., in a tumour mass or inflammation) the clearance does not occur efficiently, thereby leading to an accumulation of cellular debris, including DNA, that is then released into blood (Fig. 9).[161] Alternatively, the active mechanism for ctDNA release, studied in different tumour cell lines, could be considered a spontaneous phenomenon.[162] In fact, both CTCs and cancerous cells in micrometastatic deposits contribute to the secretion of ctDNA in the blood and its amount varies depending on the state and size of the tumour.

For this reason, by considering that the variation of total circulating DNA concentration in blood is related to many factors, such as the clearance, degradation and other physiological filtering events, observational studies have determined that ctDNA has a variable half-life in the circulation ranging from 15 minutes to several hours,[154,163-165] which makes ctDNA analysis a real-time snapshot of the disease burden. Through an exponential decay model and plotting the natural logarithm of ctDNA concentration against time, serial DNA measurements showed that some forms of circulating nucleic acids might survive longer than other cancer biomarkers. For example, ctDNA circulates in blood before CTCs, and this feature can be used for longitudinal disease monitoring (patient monitoring over time).[7] Indeed, studies comparing ctDNA and CTC levels in the bladder, breast and colorectal cancer patients demonstrated that ctDNA is often present in patients with no detectable CTC levels.[145, 166]

Hence, the analyses of ctDNA would allow a rapid and accurate detection of tumour-related genetic and epigenetic alterations if compared to other circulating cancer biomarkers. Those aspects are relevant for early cancer diagnosis and the progression of tumour burden. Furthermore, when the individual genomic profiles of a patient's tumour become more readily available, the use of ctDNA assays can be better exploited for personalized medicine and for monitoring treatment efficacy, improving clinical outcomes. In this context, there is a clear clinical need for novel diagnostic and molecular tools using liquid biopsies in oncology. Conventional sampling methods such as needle biopsies are exposed to procedural barriers in up to one in six biopsies,[167] complications in obtaining the sufficient quantity and quality of biomolecular material for genomic profiling (reported failure rates range from <10% to >30% of cases),[168,169] and sampling biases that result from tumour heterogeneity.[170-174]

The detection and monitoring of cancer disease based on body fluid markers often lack specificity,[175] and has limited resolution (in terms of both time and space) if the patients are exposed to ionizing radiation in diagnostic imaging.[176] Recent advances in ctDNA research underline the potential applications of liquid biopsies at each stage of patient management. These potential applications derive primarily from two types of information accessible through ctDNA analysis: quantification of disease burden and genomic analysis of cancer, which could be used to monitor disease burden and clonal evolution.

The increasing availability and reliability of techniques for PCR and high-throughput sequencing are facilitating novel high-sensitivity applications for ctDNA, the generation of large clinical data sets and a better understanding of the origins of both ccfDNA and ctDNA.

II.3. Approaches to ctDNA analysis

In spite of a long time elapsed since their discovery, properties of ccfDNA and ctDNA found in plasma and serum still pose some technical challenges for cancer detection and monitoring. For instance, the first difficulty arises from ccfDNA and ctDNA low concentration and relatively small size. ccfDNA concentration in cancer patients is highly variable and is often increased compared to healthy individuals. Measured ccfDNA concentration is dependent on the adopted sample pre-treatment protocols and extraction kit used.[177,178]

Typically, median ccfDNA concentrations lower than 20 ng mL^{-1} are found in plasma obtained from cancer patients, while healthy individuals show lower median concentrations (lower than 7 ng mL^{-1} in plasma) with overlaps in concentration ranges for cancer patients.[179-183] ctDNA represents a fraction of the total ccfDNA in cancer patients with percentages depending on the cancer type and progression stage.[166] In general, a mean number of mutated DNA fragments (ctDNA) per millilitre ranging from a few units to 10^4 have been found in the plasma of cancer patients accounting for few unit percents of ccfDNA. Interestingly, a ctDNA trend showing better concordance to clinical progression than CTCs has been reported for metastatic breast cancer patients.[166] This evidence, although not conclusive,[184] might suggest that combined methods involving both ctDNAs and CTCs could be used to analyze tumour status and changes.[127] Even though the mechanism leading to ccfDNA and ctDNA release in blood is still not fully understood, cells death through apoptosis and necrosis are claimed as the main processes responsible for the release of fragments of cellular DNA into the blood. Fragment size ranges in length from a few hundred to a few thousand base-pairs. ctDNA fragments of about 145-180 bp are produced from cell apoptosis, while longer fragments (up to 10 kbp) are generated from cell necrosis.[185]

The mentioned ccfDNA and ctDNA properties depict limitations for sequencing approaches such as Sanger sequencing and pyrosequencing, which only distinguish mutant from normal alleles in ccfDNA down to 15% and 5%, respectively. Such detection capabilities do not suffice to detect tumour-derived mutant fragments in early stage cancer.[154,186] In contrast, next-generation sequencing (NGS)[187-189] or innovative polymerase chain reaction (PCR)-based detection approaches such as scorpion amplification refractory mutation systems (ARMS-Scorpion),[190] digital-droplet PCR,[166] pyrophosphorolysis-activated polymerization (PAP) assays,[191] beads, emulsion, amplification and magnetics (BEAMing)[154] and tagged-amplicon deep sequencing (TAM-Seq)[155] provide good possibilities for the quantification of mutant to normal circulating DNA ratio, with capabilities in discriminating mutant allele of at least 2% (Table 1).

Table 1. Overview of PCR-based methods for the detection of circulating tumour DNA in body fluids of cancer patients. From Ref.134.

Technique[a]	Tumour-specific aberration	Source	Detected mutant to wild-type ratio (%)	Ref.
Conventional PCR	KRAS, BRAF	Tissue	10 - 25	[192,193]
COLD-PCR	KRAS, BRAF	Tissue	2.5 - 12.5	[192,193,194]
ME-PCR	KRAS	Tissue	1.0	[195]
BEAMing	APC, PIK3CA, EGFR	Plasma	≥ 0.01	[154,153,196,197]
Next-generation sequencing WGS	Chromosomal alterations	Plasma	≥ 0.75	[156]
dPCR	TP53, EGFR, BRAF, KRAS	Plasma	≤ 1.0	[155]
ddPCR	EGFR, KRAS, BRAF / PIK3CA	Plasma	0.001– 0.5 / 0.01-2.99	[198,199,200] [201]
TAM-Seq	TP53, EGFR, BRAF, KRAS	Plasma	≤ 2	[155]
dPCR/TAM-Seq	PIK3CA/TP53	Plasma	0.1 / 0.14	[202]
SNPase-AMRS-quantitative PCR	BRAF, PTEN, NRAS	Plasma	0.0005	[203]

[a] COLD-PCR, co-amplification at lower denaturation temperature-PCR; ME-PCR, mutant-enriched PCR; BEAMing, beads, emulsion, amplification, magnetics; WGS, whole-genome sequencing; dPCR, digital PCR; ddPCR, droplet digital PCR; TAM-Seq, Tagged-Amplicon deep sequencing; ARMS, amplification refractory mutation system.

BEAMing, ARMS, and ddPCR approaches are used for the detection of extremely rare alleles when the mutation type and position are known. Other platforms, such as COLD-PCR and targeted resequencing using NGS platforms, can detect rare mutant allele even when the type and location of gene mutation are undefined. Targeted resequencing is becoming increasingly popular since it can easily accommodate larger panels of genes to cover the actionable mutations in cancer that have significant diagnostic, prognostic or therapeutic implications for a specific therapy. Initially, the inherent error rate of NGS platforms made it difficult to identify very rare alleles (<1%), but strategies using paired-end sequencing and background correction have enabled detection of allelic frequencies at or below 0.1%.[204]

Nevertheless, the above-mentioned technologies suffer from a combination of intrinsic limiting factors such as the slow turnaround time (days for DNA sequencing, hours for PCR-based approaches),[205] relatively large volume input requirements (1 mL of serum or plasma is typically needed for ctDNA purification)[178] and biases arising from sample contamination and PCR-induced errors.[206]

The complexity of the analytical protocol and not affordable cost per test represent other important barriers preventing the widespread use of some of the above-mentioned technologies in daily clinical practice.

Likewise, the ability to detect mutations in plasma should not be limited to a subpopulation of patients with very high mutant copy numbers in circulation. As described in Table 1, all of the analytical platforms report the gene mutation, containing a specific allelic frequency, compared to the wild-type DNA fraction. These technologies, relying solely on the allelic frequency without recording the number of mutations, have many limitations since the mutant allele concentration (that is, copies per millilitre)[207] is affected by wild-type DNA fraction not linked to the tumour. Therefore, it is also important to consider the mechanisms that influence the amount of wild-type DNA in circulation.

Other parameters, for instance, delays in blood processing, blood storage temperature, agitation of the sample and shipment can all cause wild-type ccfDNA release from lysed nucleated blood cells and then alter the mutant/normal ccfDNA ratio.[208] For the same reason, the plasma is often preferred over serum because of the potential for cell lysis during blood coagulation.[209]

To overcome these restrictions, efforts are paid to develop new technologies for the monitoring of ccfDNA and ctDNA.

In this context, biosensing platforms offer attractive alternatives to currently available systems, owing to currently available advanced possibilities for the sensitive, rapid and cheap target biosensing.[210] Signs of progress have been recently made in nucleic acid biosensing with improvements in biosensor fabrication and production quality which benefit of new methods for the design of optimized surface chemistry,[211] and highly efficient probes for nucleic acids detection[212,213] combined with methods for the enhancement of the detected signal.[214,215] While a few excellent reviews have given comprehensive summaries of the updated PCR-based processes for ccfDNA and ctDNA detection,[177,216] here I focus on some recent advances on PCR-free biosensing methods which are expected to benefit of the absence of PCR intrinsic biases and limitations.

Over the last ten years, PCR-free biosensing technologies have been investigated with the aim to obtain more stable, reliable and sensitive detection platforms to be used for clinical diagnostic applications. Above all, PCR-free detection of nucleic acids has been obtained by putting efforts into optimizing biosensor fabrication procedures and assay design.

Table 2 summarizes PCR-free biosensing technologies that demonstrated capabilities for circulating DNA detection, by exploiting electrochemical or optical signal transduction combined with nanostructured materials for the enhancement of the detected signal.

Table 2. Use and performances in circulating nucleic acid detection of different sensing platforms. From Ref.134.

Biomarker	Tumour type	Sample	Biosensor	Surface ligand	Detected target conc.	LOD[a]	Ref.
KRAS and BRAF mutations	Lung and melanoma cancers	Serum	Electrochemical	PNA	1 fg μL^{-1}-10^2pg μL^{-1} (RNA target)	1 fg μl^{-1} (RNA target)	[53]
ccfDNA	-	Serum	Electrochemical	N-doped MGA/GNS	1.0×10^{-21} - 1.0×10^{-16} g mL^{-1} (dsDNA)	0.42 (7) ng mL^{-1} (ccfDNA)	[217]
ccfDNA	Lung cancer	Serum	Confocal spectroscopy	-	-	320 bp - 1000 bp (target size)	[218]
DNA methylation	Prostate, Breast Lung, Leukemia/ lymphomas, Colon cancers	-	SPR	ssDNA	100 - 400 nM (synthetic methylated target)	100 nM (synthetic methylated target)	[54]
PIK3CA gene mutations and methylation	Colon, breast, liver, stomach and lung cancers	Serum	LSPR	PNA	50-3200 fM (dsDNA)	50 fM (dsDNA)	[55]
EGFR gene mutation	Lung cancer	Saliva/ Plasma	EFIRM	ssDNA	0.1% detected mutant to WT ratio-	-	[56]

[a] LOD, Limit of Detection.

Appropriately designed molecular assays, with a high analytical sensitivity, able to detect rare allelic variants in ctDNA represent the crucial aim for early cancer diagnosis and personalized medicine, especially in clinical situations where ctDNA levels are below optimal levels for the detection of cancer mutations. Both electrochemical and optical transductions, when used with nanostructured-materials, show great potential for the development of PCR-free biosensing approaches. Likewise, further studies should be dealt with by producing very low-cost biosensing devices and by developing simplified assays to detect circulating tumour biomarkers in less than one hour. In addition, performances in terms of discrimination between mutated and normal alleles should be specifically investigated. In fact, among the different examples here discussed, only one reported on the detected mutant to wild-type ratio (0.1%).[56]

II.3.1. KRAS gene mutations as cancer biomarkers in liquid biopsy

ctDNA detection has been proved more sensitive and accurate at tracking tumour disappearance, spread and recurrence than protein biomarker detection when dealing with breast and bowel cancers, respectively.[145, 166] False positives should be minimized by analysing ctDNA because they are outlined by mutations and other genomic changes which are hallmarks of cancer cells.

Among all somatic mutation forms in ctDNA, members of the RAS (rat sarcoma viral oncogene homolog gene) gene family are often mutated in different cancer diseases, and there is an increasing requirement to determine the RAS mutation status of tumors for many causes: to detect cancers,[219,220] determine tumor burden,[220] guide treatment,[221-223] and monitor response.[224,225]

Some 20% of human tumours have activating point mutations in RAS, most frequently in KRAS (about 85% of the total, Fig.10), then NRAS (about 15%) and HRAS (less than 1%).[226] Specific RAS genes are mutated in different malignancies: KRAS mutations are prevalent in pancreatic, colorectal, endometrial, biliary tract, lung, and cervical cancers; NRAS and HRAS mutations predominate in melanoma and bladder cancer, respectively.[227,228]

In 1994, mutated KRAS sequences were first detected in the plasma cfDNA of patients with pancreatic cancer by PCR with allele-specific primers.[229] For each patient, the KRAS mutation found in the plasma was identical to that located in the patient's tumour, thereby confirming that the mutant DNA fragments in the plasma were of tumour origin.

KRAS mutation status is also a predictive marker for treatment with epidermal growth factor receptor (EGFR) inhibitors.[230] KRAS, acting downstream of EGFR, is an important component in EGFR signalling cascade. Activating mutations of KRAS confer resistance to anti-EGFR antibody therapy with drugs, such as cetuximab and panitumumab.[221,222,231]

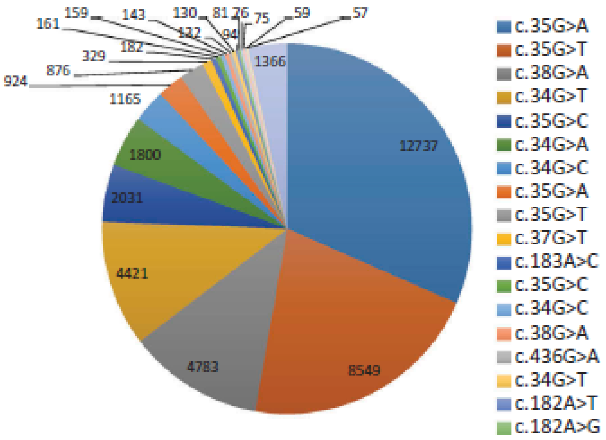

Figure 10. Data from the COSMIC database for the KRAS mutations in colorectal cancer. The first 6 mutations account for >95% of those identified. From Ref. 232.

Mutations in KRAS gene have a significant role in carcinogenesis.[233] Mutations found most frequently in KRAS gene of cancer cells are located at positions 12 and 13 of exon 2 and less frequently in codons 59 and 61 (exon 3), and codons 117 and 146 (exon 4).[234,235] Those mutations are close to the GTP binding site. Allelic mutations result in amino acid variations, namely Gly to Asp, Ala, Arg, Ser, Val, or Cys in codon 12 and Gly to Asp in codon 13.[236] Somatic missense mutations at positions 12, 13, and 61 cause disorder of the intrinsic GTPase activity of the KRAS protein, resulting in reductions in GTP hydrolysis capacity. Mutations in codons 12 (Fig. 11) or 13 are known to produce conformational changes in KRAS protein. In detail, a mutation in codon 12 of KRAS gene causes the encoded KRAS protein to "freeze" in its active state for a much longer duration than its non-mutated counterpart.[237] Mutations resulting in the substitution of amino acids 117 and 146 reduce the nucleotide affinity of KRAS protein, thereby affecting the rate of GDP/GTP exchange.

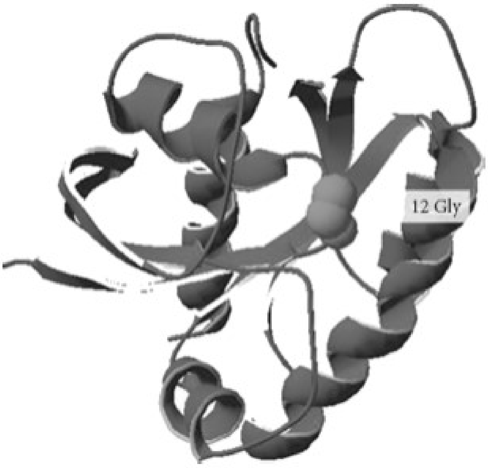

Figure 11. the position of codon 12 in KRAS molecule. Wild-type amino acid at codon 12 is shown in green. Form Ref. 238.

The appearance of RAS mutations in faeces, urine, or blood can provide an early warning of cancer but could also be used to confirm cancer in patients with positive faecal occult blood tests (FoBTs).[137,239]

The expanding clinical need for RAS mutation testing has been matched by an expanding number of methods for its determination.[240-242] Mutations in RAS genes were firstly identified by DNA sequencing, and in some instances, Sanger sequencing can still be very useful, though it tends to have lower analytical sensitivity than other methods.[243,244] Knowledge of the mutations and the identification of hot spots in the genes, which lead to their activation, allowed the design of simple PCR-based methods for mutation detection with analytical sensitivity (equating to 1%), low cost, and rapid lead time. Pyrosequencing allowed cheap and simple sequencing to reach a mass market, and became a popular technology in many molecular pathology labs, gaining new slants of life when it became clear that the detection of NRAS mutations in colorectal cancer is required to guide anti-EGFR therapy. The need to measure RAS and other genes simultaneously using small amounts of DNA is a good combination with NGS methods and is becoming increasingly widespread.

The least expensive tests tend to be PCR based, while NGS is currently higher-priced, even if NGS costs are falling and the automation is raising.

An interesting approach, which would outperform the ctDNA analysis, could be the use of PCR-free or NGS-free biosensing technologies for the detection of KRAS gene mutations in order to optimize costs, sampling biases, pre-analytic and post-analytic factors and obtain a complete diagnostic pathway with accurate results to patients and their doctors.

Chapter III

Antifouling Materials for Biosensing Applications

In this chapter, the mechanisms of antifouling materials were firstly discussed, including both theories (hydration and steric hindrance) and factors affecting the antifouling properties (molecular structures and self-assembled monolayer (SAM) architectures, surface charges, and molecular hydrophilicity). Then, the most recent advances in antifouling materials for biosensors were systematically reported, highlighting the advantages and disadvantages of their use in biological fluids. These materials included poly (ethylene glycol)/oligo (ethylene glycol) (PEG/OEG)-based materials, single amino acids, peptides and peptoids, polysaccharide-based materials, and zwitterionic compounds. Finally, the prospective research directions in the development of new non-fouling materials were discussed using modified Poly-L-lysine polymers.

III. Nonspecific Protein Adsorption

III.1. Protein – surface interaction

The study of protein–inorganic surface interactions is crucial to the rational design of new tools for biomaterials science, biosensing, nanobiotechnology and nanomedicine. Such interactions are responsible for the biocompatibility of materials used in different fields, such as tissue engineering,[245,246] biosensors,[247,248] and blood-contacting devices.[249,250]

Nonspecific adsorption of proteins can affect surface properties of biomaterials and trigger the degradation of devices operating in contact with biological fluids. Specifically, for biosensors, this phenomenon may cause functional device interference, possibly preventing the detection of biological targets available at low concentrations in complex media.[5, 251]

Biomaterial surfaces may be chemically treated to form antifouling layers capable of reducing or, ideally eliminating, the fouling effect due to nonspecific protein adhesion.[5,251,252] In this context, a better comprehension of multiple factors affecting the process of protein adsorption is required in order to design the most advantageous antifouling material without altering the performance of the biomaterials.

Proteins are complex biopolymers composed of various amino acid monomers which, due to the unique nature of their side-chain, show numerous properties such as hydrophobicity/hydrophilicity, polarity, acidity/basicity and charge.[253] The amino acid sequence and three-dimensional arrangement determine the protein function (e.g. metabolic, signalling, architectural) and interaction with the external environment. Proteins are amphipathic, surface-active macromolecules with heterogeneous, adaptable shell that can display high affinity for virtually any type of man-made surface.[253] Several comprehensive reviews have been published to deal with this topic of protein-material interaction from both a theoretical and experimental perspectives.[254-256]

When the surface of an exogenous (artificial) material is exposed to proteins, such as those found in biological fluids (e.g. blood), many interactions take place.[256,257] One of the first events often overlooked is the spontaneous adsorption (nanoseconds timescale) of water molecules and ions to form a water/electrical double layer.[258] Shortly (within seconds),[259] proteins migrate from the bulk solution towards the surface via convection/diffusion, where they absorb through a combination of multiple van der

Waals, hydrogen bonding, electrostatic and hydrophobic forces.[260] Once a protein is adsorbed on the surface, to optimize the energy of interaction and in response to their environment can eventually assume altered conformational states and interact with surfaces in multiple ways of various strength.[253]

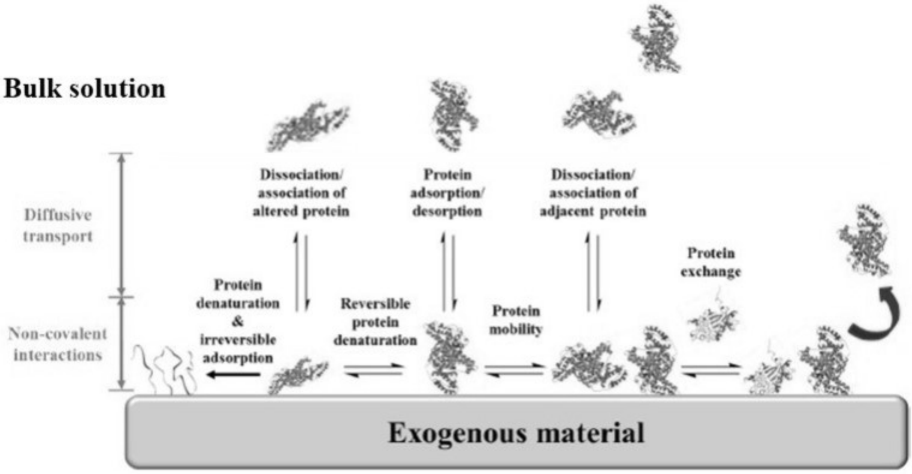

Figure 12. Schematic representation of protein adsorption onto artificial surfaces. Adapted from Ref. 260 and 261.

Obviously, the phenomenon of protein adsorption onto surfaces is a complex process. The latter is dynamic in nature and relies on the following time-dependent phases:

(i) migration from the bulk phase towards the surface;
(ii) random surface adsorption/desorption;
(iii) spreading through conformational changes (accompanied by a decrease in the rate of desorption);
(iv) exchange or irreversible adhesion and denaturation (Fig. 12).

Beyond the surface affinity, it is thus clear that the final composition of an adsorbed layer of proteins will be greatly affected by the various kinetic aspects of adsorption, which is unique to each (type of) protein competing for a surface spot. One important related parameter that describes the phase (i), depending on the protein size as well as bulk concentration, is the *diffusion coefficient*, values of which are given in Table 3 for the main proteins of blood plasma.[262]

Table 3. Molecular weight, concentration and diffusion coefficient of the main proteins in blood plasma. From Ref. 262.

Plasma Protein	Molecular weight (kDa)	Plasma concentration (mg mL^{-1})	Diffusion coefficient (10^{7} cm^{2} s^{-1})
Albumin	66	40	6.1
IgG	150	8-17	4.0
Transferrin	77	2.3	5.0
HDL	170	18	4.6
IgA	150	1-4	4.0
Complement 3	180	1.6	4.5
Fibrinogen	340	2-3	2.0
LDL	2000	2.0	2.0

Furthermore, a relatively limited series of parameters have been known to influence the protein adsorption, which is associated with:

(i) the nature of proteins relating to their morphology and flexibility, size and molecular weight, and charge/polarity strength;
(ii) the surface physicochemical properties (e.g. topography, electrostatic potential, surface energy);
(iii) the environmental conditions (e.g. pH, ionic strength and temperature).[256,263,264]

Empirical principles are shown in the literature.[258,265] For instance, it seems as though the larger a protein, the more likely it is to possess multiple adhesion sites hence readily adsorb to a surface. The same would hold true for proteins near their isoelectric point (the pH value at which a protein is electrically neutral).[253] About the surface properties, proteins would tend to display a higher affinity for hydrophobic surfaces than hydrophilic ones,[257,258,266] because the hydration layer coupled with the polymeric surface layers acts as a barrier to prevent the protein fouling. Moreover, the flexibility of the polymer chains reduces the nonspecific adsorption of proteins via steric exclusion mechanisms.[267]

The surface roughness also plays a role in the protein adsorption, where greater amounts of proteins adsorb on rougher surfaces.[268]

In relation to the environmental conditions, it would look like that the higher the temperature, the greater the rate of protein adsorption and the resulting amount of adsorbed proteins.[269]

As above-mentioned, the complexity of the mechanism of protein adsorption as well as the multiplicity of influencing parameters has to be controlled with extreme caution, because it could exist the possibility of finding equally compelling counter-examples. Probably, this apparent disagreement is due to the tendency of small proteins – with which most protein adsorption studies are performed – to form monolayers, whereas less investigated larger proteins have been experimentally shown to produce multilayers. Also, it is important to remark that blood proteins from different mammalian species may display different adsorption behaviour.[258]

Finally, different adsorbed protein orientations, conformations and packing can be obtained for a given protein-surface,[259] owing to the possible divergences in the multivariate, complex mechanism of the protein adsorption.[256]

III.2. Mechanism of Antifouling Surfaces

III.2.1. Hydration

Basic requirements to prevent the protein adsorption via hydrophobic and ionic interactions are a minimum interfacial free energy with water and zero surface charge. The fabrication of hydration layers, attached tightly to chip surfaces, is critical for antifouling, as they create a physical energy barrier that inhibits the adsorption of proteins and other contaminants.[270] When hydrophilic materials are exposed to bulk water, water molecules, residing on and/or penetrating into non-fouling materials, can be classified into two types of surface-bound waters formed by hydrogen bonding for hydrophilic materials, and by even more strongly electrostatic forces produced from ion solvation for zwitterionic materials.[270] Expulsion of water molecules from both surface and protein is the first and obligatory step to facilitate the protein adsorption by reducing free energy barrier arising from dehydration entropic effects.[258]

The highly hydrated polymeric films exhibit a good non-fouling property, hence, any decrease in the surface hydration might lead to the decrease of resistance to nonspecific protein adsorption. Since hydrogen bonds are relatively easy to break and reform, hydrophilic materials such as polyamide, mannitol, and Poly(ethylene glycol) (PEG) often are subjected to the transition from non-fouling to fouling behavior following the change in surface hydration[271,272] caused by the increase of packing density,[270] the rise of temperature[273] and hydrophobicity, when copolymerized with hydrophobic monomers.[274,275] On the other hand, in zwitterionic polymers including polypeptides, betaine and its derivatives, phosphorylcholine and its derivatives, the electrostatic forces play a role in the reduction of the protein fouling.[276] These materials combine with water by ionic solvation to form a hydration layer resistant to proteins adsorption and cells adhesion.

Zwitterionic materials containing both positive and negative charged units can bind water molecules even more strongly and stably via electrostatically induced hydration, as compared to those hydrophilic materials to achieve surface hydration via hydrogen bonding. Hence, materials with more strongly ionic solvation fall into the scope of searching for non-fouling materials.

The strength of surface hydration is primarily determined by the physicochemical property of materials, such as steric hindrance, molecular weight, surface charge, surface chemical components, and the geometric properties of the surface packing, including thickness, density, and conformation or architecture.[277,278] The hydration of zwitterionic groups could be easily compromised and the increase of nonspecific protein adsorption can be induced at certain experimental conditions, such as very low ionic solution, very large molecular weight, extremely high or low packing density, or low temperature.[270]

III.2.2. Steric hindrance

Aside from surface hydration, chain flexibility plays also an important role in protein resistance. When protein approaches the surface, the compression of the polymer chains causes a steric repulsion to resist protein adsorption due to an unfavourable decrease in entropy.[279] Especially in long-chain polymers, the steric hindrance, caused by soft long chains, contributes to the resistance of nonspecific protein adsorption. The latter hypothesis indicates that, when the proteins come up to an antifouling surface modified with long-chain polymers, the proteins squeeze the polymer, which generates a steric hindrance and higher entropy that discourage the adsorption to the surface.

Molecular details of the surface are of great importance to protein adsorption. Self-assembled monolayers (SAMs) are well suitable platforms to study the adhesion of proteins at the molecular level. Nanoscale surface properties can be precisely controlled via varying the abundance, type, and spatial (both normal and lateral) distribution of tail groups of the SAMs.

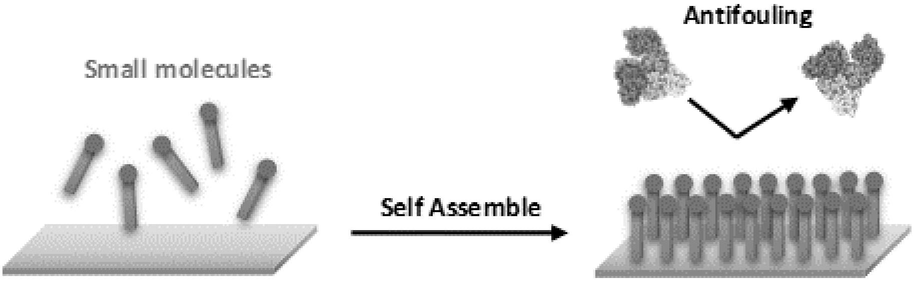

Figure 13. Schematic formation of antifouling coatings of self-assembled monolayers (SAMs).

Four common features for those surfaces resisting to the protein adsorption are summarized:

(i) Hydrophilic behaviour;
(ii) Electrically neutral composition;
(iii) Presence of hydrogen bond acceptors;
(iv)The absence of hydrogen bond donors.

However, this generalization does not explain the performance of all non-fouling surfaces, especially carbohydrates terminated SAMs. For instance, a SAM terminated with mannitol groups only containing H-bond donor can prevent the adsorption of several proteins and the attachment of cells onto the functionalized surface, and a similar effect was recorded for a SAM presenting oligo (ethylene glycol) (e(EG)$_n$OH and e(EG)$_n$OCH$_3$, n = 3 – 6) groups.[280] This result also indicates that the formation of tightly bound water via hydrogen bonds between interfacial waters and surfaces does not necessarily require H-bond acceptors materials, rather than H-bond forming materials. Both nanoscale surface structural and chemical properties of SAMs affect the adhesion of the proteins, including the adsorption kinetics, the adsorption isotherm, and the morphology of the proteins on surfaces.

Surface hydration is often used to interpret the non-fouling behaviour of the short-chain SAMs because the strongly bound water molecules on the topmost part of SAMs are the only source of large repulsive forces to repel the protein adsorption. While the chain flexibility, connected to the steric hindrance, plays a tiny role in protein resistance due to tightly packed density and short rigid chains. Nonetheless, for the long-chain polymer, both surface hydration (i.e. water barrier) and chain flexibility (i.e. steric repulsion) contribute to the surface resistance to nonspecific protein adsorption.

III.2.3. Surface charges

The density and distribution of the surface charges on polymers can influence the electrostatic interactions between the polymers and water molecules, as well as those between polymers and proteins. This effect can involve the hydration layer and the adsorption of fouling matters on the surface. The surface charge density clearly affects the antifouling capacity of materials. Nevertheless, as for hydrophilicity, no definite correlations can be found between the surface charge density and the fouling effect.

Numerous efforts have been carried out to reduce fouling by incorporating ionizable functional groups.[281] In most cases, the surfaces are negatively charged, but attempts have recently been made to develop positively charged membranes. Similar to the negatively charged surface membranes, the positively charged membrane surfaces work as barriers for co-ions (cations) due to the dominance of the exclusion mechanism.[282] For instance, the positively charged membrane surface exhibited repulsion against positively charged proteins.[283]

Counter-charged terminal groups of different valence and various protonation/deprotonation forms have been realized to obtain nonspecific protein-resistant mixed SAMs.[284] It is demonstrated that the excellent non-fouling surfaces can be readily constructed from mixed positively and negatively charged components of equal valence in a wide range of thiol solution compositions. Results showed that a single compact layer of balanced charged groups with a crystalline structure can resist the adhesion of proteins, but the conformational flexibility is not required for protein resistance of a surface. Hence, the hydration layer formed on the mixed SAMs plays a dominant role in surface resistance to nonspecific protein adsorption.[270]

Multilayers, that assume a particular surface charge, can adsorb biomolecules with the opposite charge, and the surfaces of the opposite charge to proteins have been considered more effective at promoting the adhesion of proteins. An addition of salt can reduce the electrostatic interactions, the adsorption of proteins can decrease on the oppositely charged surface because the surface charge is screened by salt, thus demonstrating that only the electrostatic interactions are responsible for the adhesion of proteins.

Finally, recent experiments propose that the addition of zwitterionic material, lending an overall charge neutrality on the surface, can be more effective for the antifouling surface as compared to the conventional positively or negatively charged membrane surface.[285]

III.3. Antifouling Materials

Antifouling materials are classified according to the chemical composition of the hydrophilic polymer. Common materials are based on poly (ethylene glycol)/oligo (ethylene glycol) (PEG/OEG)-based materials, single amino acids, peptides and peptoids, polysaccharide-based materials, and zwitterionic compounds. The reduction of the protein adhesion may prevent or at least minimize the adverse reactions caused by nonspecific adsorption such as coagulation, complement activation, platelet adhesion, leukocyte adhesion and activation and the foreign body response.[254,286]

Three different generations of antifouling polymers have evolved and have been extensively studied: 2-hydroxyethyl methacrylate (HEMA)-based polymers, PEGylated-based polymers and zwitterionic-based polymers. The chemical structures of these polymers are depicted in Figure 14.

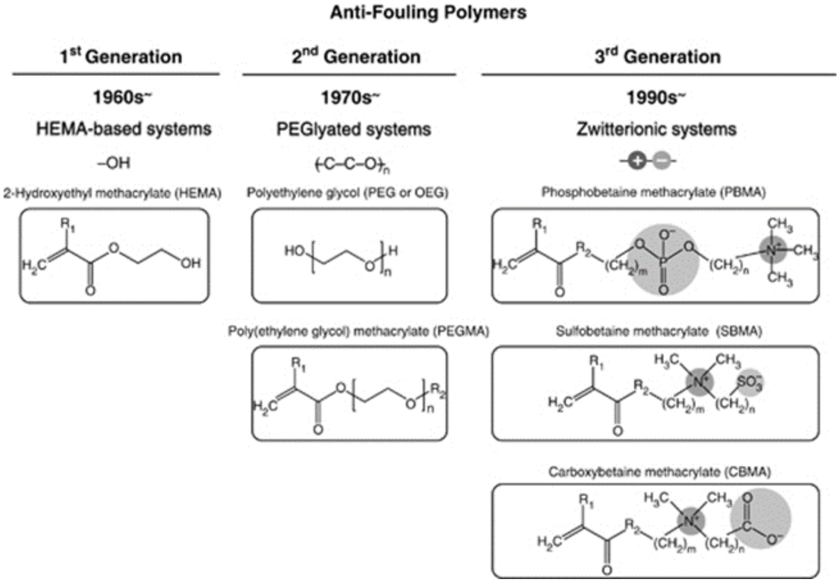

Figure 14. Evolution of antifouling materials. Form Ref. 287.

III.3.1. HEMA – based systems

The first-generation materials, which derived their fouling resistance from their hydrophilicity, have been polymerized from neutral hydroxy-functional methacrylate (HEMA) monomers.

PolyHEMA contains many hydroxyl functional groups (-OH), which can make hydrogen bonds with water and with each other,[287] and subsequently form a tightly bound hydration layer to resist biomolecules adsorption. However, a number of studies reported a poor antifouling performance of polyHEMA-based materials in undiluted human blood serum and plasma.[288] When these hydrophilic materials are in contact with complex media, none of them keeps their non-fouling properties, most likely due to the complex physicochemical interactions between proteins and surfaces. Dense hydrophilic poly(2-hydroxyethyl methacrylate; PHEMA) brushes also possess excellent biocompatibility, physical properties and excellent protein repellency.[289] PHEMA graft chains can become highly extended and oriented to physically exclude the protein molecules from the entire brush layer.

III.3.2. Polyethylene Glycol (PEG) polymer

Polyethylene glycol (PEG) is a linear polymer with repeat unit $–CH_2–CH_2–O–$. PEG is crystalline and is soluble in water at room temperature. PEG (especially PEGs of molecular weight above 2000) arises in solution at a temperature known as the cloud point. The cloud point depends generally on solution conditions such as ionic strength and PEG concentration.[290] For instance, under high ionic strength condition (buffer containing 0.6 M K_2SO_4), the cloud point of around 60°C has been observed.[291] PEG is considered to be non-toxic and has been used for the modification of protein drugs by so-called PEGylation.[290]

Two mechanisms have been proposed to explain the protein resistant properties of PEG attached to a surface. The first process implicates the flexibility and mobility of PEG chains. The flexibility is based on the conformational freedom of the –C–C–O– backbone of PEG owing to unrestricted rotation around the C–O bonds. This mechanism is usually indicated as *"excluded volume – steric repulsion"* (Fig. 15). When the protein moves closer the PEG-modified surface, the biomolecule compresses the flexible PEG chains. This latter involves an entropy loss generating a repulsive interaction, thus effectively pushing the protein away from the surface.[292]

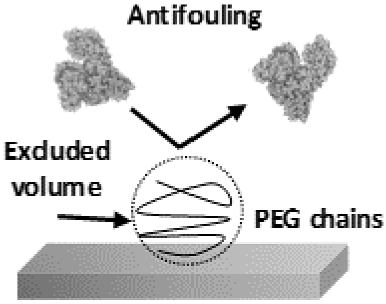

Figure 15. Excluded volume-steric repulsion of proteins by PEG.

The second process is related to the low interfacial energy at the PEG-water interface, and the skill of the PEG chains to bind water tightly (hydrogen bonding). Each ethylene glycol repeating unit in the PEG backbone can strongly bind to one water molecule, bridging the ether oxygen along the 72 helical PEG chains.[293] This unique interaction between the water and the PEG chain results in the formation of a highly hydrated layer and ultimately leads to a steric hindrance to the approaching protein molecules.[270] Based on this mechanism, also referred to as *"osmotic repulsion"*,[279] the proteins stay off the surface via the water barrier.

Different surface modification techniques have been used with PEG chains ranging from physical adsorption (coating) to covalent grafting to chemisorption. When PEG is covalently grafted or chemisorbed to the surface by its end group, three surface regimes may be differentiated depending upon PEG density.[294] If the density is low, PEG molecules will be in a random coil conformation giving the so-called "mushroom regime", where PEG chains do not overlap and there are empty spaces between them. As the density increases, PEG chains cannot maintain the random coil state and must enlarge to have an arrangement. At higher density when the distance between PEG chains is smaller than the radius of gyration, the chains will be more completely extended, and the surface is in the "brush regime" (Fig. 16).

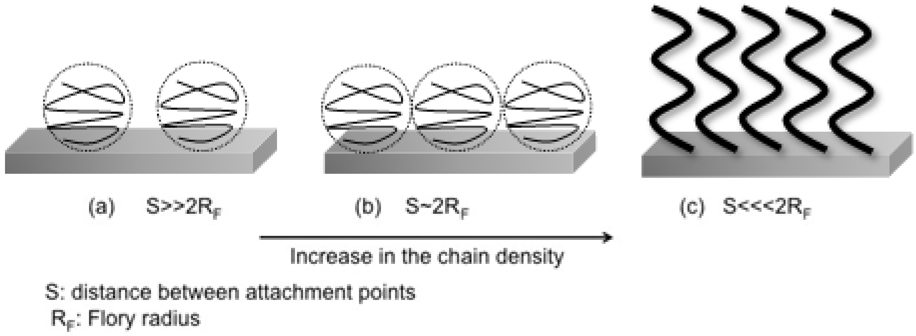

Figure 16. Illustration of PEG polymers after surface grafting of PEG monomer. The PEG conformation on the surface, determined by the chain density, changes from non-overlapping "mushrooms" to fully extended "brushes". Adapted and redrawn from Ref. 295.

Furthermore, to improve the antifouling properties of PEG polymers many research groups studied the modifications of the PEG/OEG chains via changing the length, size and morphology of the unit, the polymerization density, and the properties of the terminal group.[296,297]

Despite the attraction of PEG compounds as an antifouling agent, low surface densities[298] and susceptibility to oxidative damages or transition metal ions[299,300] limit the antifouling capabilities of PEG-based materials in long-term applications. Additionally, it has been shown that reactive oxygen species, produced by PEG polymers, might modulate the cell response.[301] For these reasons, alternate hydrophilic polymers such as polyglycerols,[302] polyoxazolines,[303] polyamides,[304] and naturally occurring polysaccharides have been evaluated for antifouling applications.[305]

III.3.3. Zwitterionic polymers

Zwitterionic materials have emerged as promising candidates for advanced antifouling/biocompatible materials, because of their high hydration capacity and electroneutrality.[306,307] Zwitterionic polymers exhibit balanced anionic/cationic groups on their molecular chains, which make them highly hydrophilic and antifouling while maintaining overall charge neutrality.[305,306] Moreover, zwitterionic polymers show higher stability to oxidation than PEG polymers,[289] making them a valid alternative to the widely used PEG-based materials.[307]

A critical factor determining non-fouling properties of polyzwitterionic materials is to control both uniformity of charge distribution and charge neutrality of two oppositely charged moieties on the surface. Such factors can be controlled either by using zwitterionic units,[308-312] or, more easily, by mixing positively and negatively charged moieties in mixed-charge self-assembled monolayers (SAMs),[308,313] polymer coatings,[314] or hydrogels.[315]

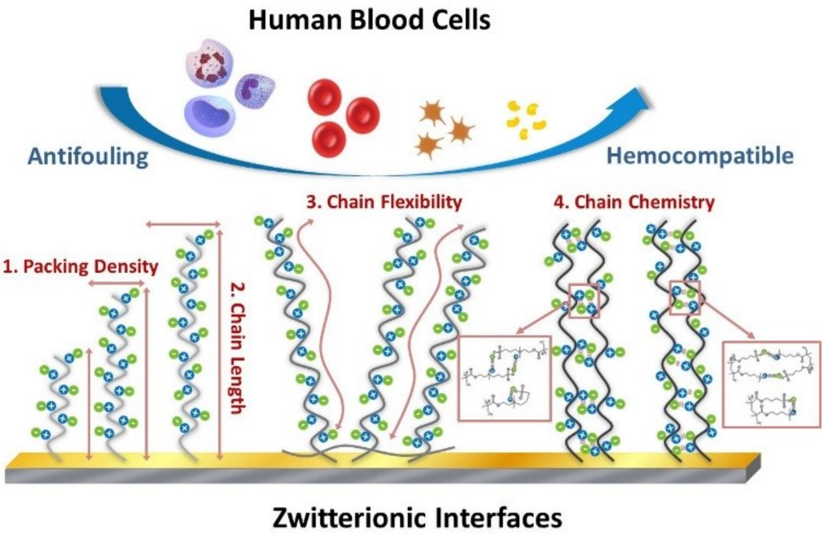

Figure 17. Molecular design of zwitterionic interfaces for excellent hemocompatibility. Adapted from Ref. 287.

Simple methods for the surface functionalization with zwitterionic compounds via covalent bonds would allow solving the limitations linked to the atom-transfer radical polymerization (ATRP),[316] and surface-initiated photoiniferter-mediated polymerization (PIMP).[317,318]

Polyzwitterionic materials can be classified according to the chemical composition of monomer units. Common zwitterionic polymers are based on phosphorylcholines,[276] betaines,[319] and polypeptides/peptoids,[320] widely applied to biosensors.

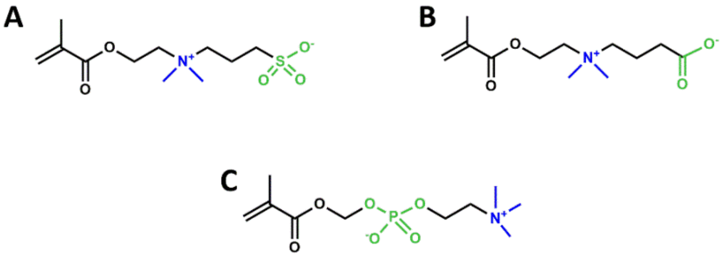

Figure 18. Chemical structures of three types of zwitterionic monomer: (A) sulfobetaine methacrylate, SBMA; (B) carboxybetaine methacrylate, CBMA; (C) phorylcholine methacrylate, PCMA.

Phosphorylcholine (PC)–based zwitterionic polymers showed good effectiveness for anti-adsorption of proteins and cells due to the hydration reaction. For instance, it was discovered that phosphorylcholine could prevent the fouling effect by fibrinogen and cells through the realization of an antifouling layer of polymeric epoxy resin-polyethersulfone-phosphorylcholine.[321] Many publications related to PC materials have been performed with methacryloyloxyethyl phosphorylcholine (MPC)-based polymers, which can be successfully grafted onto various substrates via free-radical polymerization methods.[289] Anyway, MPC could not be widely used in the antifouling performance because it is moisture sensitive and difficult to synthesize and manage.

Other zwitterionic groups, such as sulfobetaine (SB) and carboxybetaine (CB) have been developed recently thanks to good biocompatibilities and potential antifouling applications.[322]

Densely packed poly (sulfobetaine methacrylate) (polySBMA)-grafted surfaces have also been reported to be completely resistant to the adsorption of plasma proteins, including human serum albumin, gamma globulin, fibrinogen, and lysozyme, even at low ionic concentrations.[298,323]

Along with poly(SBMA) coatings, carboxybetaine–methacrylate (poly(CBMA)) brushes have been prepared, and both zwitterionic polymer brushes (poly(SBMA) and poly(CBMA)) grafting surfaces reported clearly a reduced adhesion of fibrinogen to a level comparable to that on par with PEG-based coatings.[324] The high resistance of the plasma protein adsorption from poly(CBMA), as well as its unique anticoagulant activity, makes poly(CBMA) attractive because of its unique versatility for immobilizing ligands, such as proteins and antibodies, onto the carboxyl groups.[270] So, this dual functional features of polyCBMA would make it useful for the design of antifouling surfaces for biosensors and medical applications.

III.3.4. Special Zwitterionic Materials: Peptide and Peptoid

Unlike PEG compounds, the peptides represent a second-generation biodegradable material for antifouling SAMs thanks to their exceptional resistance to the proteins. Naturally occurring biomolecule such as amino acids, peptides, and polysaccharides are also commonly used in the development of innovative antifouling materials since they have a protease resistance property, precise control of molecular weight, and broad versatility of the side-chain composition.[289,325,326] One theory to explain the prevention of biofouling, through the peptide systems, is the structural conformation under physiological conditions.[327]

Many examples of antifouling materials based on peptide have been reported in the literature.[325,15,328] For instance, peptide-based ultrathin SAMs with an arbitrary sequence have been performed to study the interactions of proteins with these biomimetic surfaces. Although using peptides to fabricate a surface resistant to the adsorption of proteins is somewhat not logical, the resulting peptide SAMs exhibit resistance to nonspecific adhesion of proteins including streptavidin, bovine serum albumin (BSA), and fibronectin, which is comparable to the PEG-based SAMs.[298] Also, ultra-low fouling natural peptides, composing of negatively and positively charged residues, have been produced such as glutamic acid, aspartic acid, and lysine, in the form of either alternating or randomly mixed charge. Their natural high resistance to nonspecific protein adsorption is similar, yet again, to that of PEG-based materials.[287]

An innovative group of synthetic antifouling macromolecules have been studied to avoid the fouling effect in the biological environment for long-term applications. These peptidomimetic polymers are able to mimics polypeptides attached to biomaterial surfaces,[305] and consists of a short functional peptide domain containing alternate dopamine and lysine residues to adhere to surfaces. Also, these synthetic materials have an N-substituted glycine (peptoid) oligomer of variable length which has a protein-like backbone with side-chain derivatization on the amide nitrogen rather than to the α-carbons (as they are in amino acids). The methoxyethyl side-chains provide the fouling resistance to surfaces and resemble the repeat unit of PEG compound, resulting in excellent protein resistance.

Peptoid-based materials, as non-natural biomimetic polymers, can be tuned for their antifouling ability.[327,329] Using the sequence specificity of polypeptoids, many functionalities with the antifouling property can be incorporated in a single backbone. A library of such sequence-specific materials can be designed for optimizing the antifouling performance of these materials.

III.3.5. Hybrid, derivative and biomimetic materials

In many publications, several research groups reported hybrid surface peptide-based modifiers consisting of a Poly-L-lysine (PLL) polypeptide backbone partially grafted with different antifouling molecules, like PEG side-chains, through amine residues (Fig.19).[330-332]

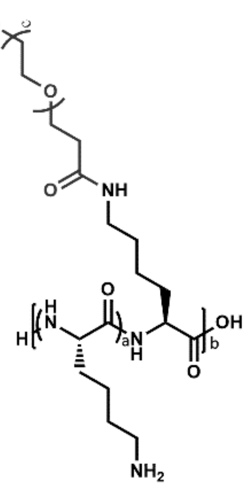

Figure 19. Example of the molecular structure of PLL grafted with PEG (PLL–g–PEG). Application for antifouling surfaces.

PLL is a versatile polymer composed of positively charged lysine amino acid as a repeat unit, which has attractive biochemical properties, including hydrophilicity, excellent biocompatibility and an acceptable degree of biodegradability.

Because PLL is positively charged at physiological pH, it can be easily adsorbed on a large variety of negatively charged substrates via electrostatic interactions, including glass,[333] metals,[334] polymers,[335] and metallic oxides.[336]

The physical adsorption of PLL polymer is comparable to that of other polyelectrolytes,[337] and, analogously to the proteins,[338,339] it occurs via two main steps: (i) diffusion of polyelectrolyte from the bulk solution and attachment of polyelectrolyte to the surface and (ii) rearrangement of polyelectrolytes in the adlayer. The latter step includes the intramolecular charge, the hydrogen bond redistribution and molecular aggregation, as reported in recent studies.[257,337] In fact, these steps could be mainly controlled by the electrostatic interaction between the polyelectrolyte and the substrate, and the electrostatic repulsion between the polyelectrolyte chains.[340,341] In this case, the adsorption rate and total attachment of the polymer depend on the functional charged groups of both PLL and the substrate, and accordingly, this process is sensitive to changes in pH, temperature, and ionic strength of the solution.[340,341]

PLL polymer can also be easily modified with nonionic side-chains (like PEG/OEG), thereby making it an ideal candidate for engineering biomaterial interfaces, such as surface coatings,[334,342] drug,[343] gene,[344] and protein[345] delivery platforms, and hydrogel scaffolds.[346]

The easy functionalization of PLL polymer with different functional groups allows having critical control over the biosensing interfaces by creating mixed monolayers with different functionalities.[347] For instance, antifouling materials could be performed by grafting the positively charged moieties of PLL polymer with negatively charged side-chains. The final result could be a mixed-charge polymer, with high resistance to nonspecific protein adsorption, by exploiting the combination of non-fouling properties of zwitterionic and polypeptide compounds.

Taken together, these key points emphasize the need to expand the understanding of the use of PLL polymer as antifouling material, thereby improving the surface modification strategies for biosensing applications.

PhD Thesis Aim

Considering the main advantages of biosensors for cancer diagnosis, especially by using molecular biomarker analysis through liquid biopsy, and the requirement of new antifouling materials for limiting the nonspecific protein adsorption from human blood samples, the aim of this PhD project consists of the realization of Surface Plasmon Resonance Imaging (SPRI) plasmonic biosensors for the detection of single point mutations in KRAS gene, standard actionable cancer biomarkers for colorectal cancer, in human plasma samples. The method has a high sensitivity, thus allowing to avoid any Polymerase Chain Reaction (PCR) amplification of the genetic material.

Initially, the immobilization of specific peptide nucleic acids (PNA) probes onto the gold SPR sensor chip surface has been optimized. PNAs show a structure similar to DNA with an electrically neutral polyamide backbone. This property makes stable the PNA-DNA complexes during the hybridization, thanks to the absence of electrostatic repulsion between negative charges of phosphate groups of DNA molecules. PNA probes have been designed to ensure the hybridization with ctDNA target sequences. Specifically, PNA KRAS exon 2 probes (namely Wild-Type (WT) and mutated (Mut) such as G12D, G12V and G13D) have been used. The spatially controlled immobilization of PNA probes has been obtained by injecting PNA WT and PNA Mut solutions into a microfluidic system coupled to SPR sensor chip.

The extremely low concentration of ctDNA requires an enhancement of SPRI detection capabilities. In this case, gold nanoparticles (AuNPs) have been used to amplify the hybridization signal between target analytes and corresponding PNA probes. In fact, AuNPs in SPRI measurements allows to achieve a higher sensitivity (10^{-15} - 10^{-18} M), thanks to plasmonic coupling generated onto the SPRI sensor and gold nanoparticles.

In order to optimize the nanoparticle-enhanced SPRI detection of genomic samples, aged (from 5 days to 2 months) DNA KRAS exon 2-conjugated AuNPs (AuNPs@oligoDNAKRAS conjugated AuNPs) have been tested against experiments aimed at detecting 5 pg μL^{-1} (≈ attomolar, aM) solutions of genomic DNA WT KRAS exon 2. I found that both fresh and aged conjugated AuNPs provide an excellent discrimination between WT and mutated DNAs.

After preliminary results of nanoparticle-enhanced SPRI assay for the detection of genomic DNA with single point mutations in KRAS gene exon 2, I performed the development of new mixed-charge polymer based on PLL modified with an anionic peptide, which are connected via a nonionic OEG spacer, in order to achieve control over the charge distribution of PLL-coated surfaces and thus antifouling character. The PLL backbone has been functionalized with different percentages (y%) of maleimide-OEG-NHS ester chains (PLL-mal(y%), from 13% to 26%), to study its effect on the antifouling properties. The anionic oligopeptide CEEEEE, composed of one cysteine (C) and five glutamic acids (E), has a short sequence to limit the thickness of the mixed-charge polymer antifouling coating, and the grafting density can be varied to tune the balance of charged groups at polymer backbone. Upon the adsorption of PLL-mal(y%) polymer on a gold surface, the anionic peptide CEEEEE has been attached to the maleimide units through the thiol–maleimide Michael-type addition, thereby creating the antifouling PLL-mal(y%)-CEEEEE polymer on the surface in a two-step process. PLL-mal(y%)-CEEEEE surfaces have been characterized by water contact angle and polarization modulation infrared reflection-absorption spectroscopy (PM-IRRAS). Complementary acoustic (quartz crystal microbalance with dissipation, QCM-D) and plasmonic (surface plasmon resonance imaging, SPRI) techniques have been employed to monitor the adsorption of bovine serum albumin (BSA), used as standard single-protein solution, and diluted human plasma samples.

Hence, I realized a novel nanoparticle-enhanced SPRI assay for ctDNA detection, carrying KRAS gene mutation, in diluted human plasma samples using PLL-mal(y%)-CEEEEE layer as antifouling coating. Initially, PNA WT and PNA Mut probes have been attached to the maleimide units through the thiol–maleimide Michael-type addition; therefore, the anionic peptide CEEEEE has been anchored to the free maleimide moieties by the above-described thiol–maleimide reaction, using a microfluidic system coupled to SPR sensor chip.

The analysis of ctDNA in diluted human plasma samples (at concentration 5 pg μL^{-1}), collected from cancer patients and healthy donors, has been carried out using AuNPs@oligoDNAKRAS, as previously described. The human plasma specimens with ctDNA targets have been treated with minimal sampling handling to avoid any sample contaminations and disruption of the antifouling activity of PLL-mal(y%)-CEEEEE layer. The dilution of the biofluid (10%) has been preferred in order to minimize the impact of non-specific adsorption on the SPR sensor. Although, this operation promises the detection of analytes at higher concentrations, the dilution of the complex medium could interfere with the analysis of lower concentration ctDNA or with targets with low affinity, which could be diluted below their limit of detection in the process. The combined use of PLL-mal(y%)-CEEEEE as antifouling layer with the functionalized gold nanoparticles for the enhancement of target detection overcomes the limiting factors related to the sample dilution, and offers an excellent ctDNA discrimination in the bloodstream at attomolar level, well below the typical concentration of ctDNA in cancer patients' blood at early-stage disease (nanomolar and picomolar concentrations).

Chapter IV

Materials and Methods

A description of the materials and procedures employed throughout this doctoral work is summarized. A detailed explanation of nanoparticle-enhanced SPRI assay is provided, followed by the nanofabrication protocol of the antifouling layer based on the mixed-charged polymers. Thereafter, the scheme of nanoparticle-enhanced SPRI assay for ctDNA detection, carrying KRAS gene mutation, in human plasma samples is provided. Also, a list of all chemical reagents, buffers and biological compounds is included. Finally, the chapter describes the biofunctionalization protocols and the different assay formats employed, whose results are presented in this dissertation.

IV. Materials and Methods

IV.1. Materials and Reagents

Reagents were obtained from commercial suppliers and used without further purification. Wild-type streptavidin (WT-SA) was purchased from Invitrogen (Italy). Nitrocellulose membrane filters were purchased from Whatman (UK). Trisodium citrate dihydrate, tetrachloroauric(III) acid, ethanol, dimethyl sulfoxide, sodium hydroxide solutions (10 M in water) and dithiobis(N)succinimidylpropionate (DTSP) were purchased from Sigma–Aldrich (Italy). Phosphate buffered saline (PBS) solutions at pH 7.4 (137 mM NaCl, 2.7 mM KCl, phosphate buffered 10 mM) were obtained from VWR (Italy). Biotinylated oligonucleotide DNA KRAS exon 2 (oligoDNA KRAS) (5'-CAAGTTTATATTCAGTCAT-BiotinTEG-3') was purchased from Thermo Fisher Scientific, Inc. PNA probes (PNA KRAS exon 2 wild-type (PNA WT), H-$(AEEA)_2$-CTACGCCACCAGCT-Gly-NH_2; mutated PNA (PNA Mut), such as: PNA KRAS exon 2 G12D (PNA G12D), H-$(AEEA)_2$-CTACGCCATCAGCT-Gly- NH_2; PNA KRAS exon 2 G12V (PNA G12V), H-$(AEEA)_2$-CTACGCCAACAGCT-Gly- NH_2; PNA KRAS exon 2 G13D (PNA G13D), H-$(AEEA)_2$-CTACGTCACCAGCT-Gly-NH_2) were provided by University of Parma (Prof. R. Corradini group). Genomic DNA samples for KRAS exon 2 for Wild-Type and G12D, G12V, G13D mutations (gDNA WT, G12D, G12V and G13D) were provided by Italian National Cancer Institute Regina Elena (Rome, Dr. P. Giacomini). SPRI gold chips were purchased from GWC Technologies (USA). Ultra-pure water (Milli-Q Element, Millipore) was used for all the experiments.

IV.1.2. PNA probe synthesis and surface immobilization

The PNA sequences were designed, synthesized by using automatic solid phase synthesis, purified and characterized as previously described.[348] An optimal surface probe density is needed in order to obtain consistent and reproducible SPRI results because an extremely dense surface decreases the sensitivity during the oligonucleotide hybridization step.

Gold chips (GWC Technologies, U.S.A.), previously functionalized with DTSP, were used to immobilize PNA WT and PNA Mut probes. The procedure adopted for gold chip functionalization consisted of the immersion of bare gold chip in a DTSP solution (4 mM in DMSO) for 48 h.[349] Modified chips were then carefully rinsed with ultrapure water and ethanol. PNA WT and PNA Mut probes were immobilized on DTSP-modified gold chips through the amine-coupling reaction between N-hydroxysuccinimidyl (NHS) ester ends of DTSP and the N-terminal group present at 5’-position of the 2-(2-aminoethoxy) ethoxyacetic acid (AEEA) linker. The spatially separated immobilization of PNA probes was obtained by injecting PNA WT and PNA Mut solutions (0.1 µM in PBS, flow rate 10 µL min^{-1}) into parallel microchannels in contact with the DTSP-modified gold surface. AEEA linkers were used to minimize surface effects caused by the steric hindrance of immobilized systems.

IV.1.3.SPRI apparatus and measurements

All the SPRI experiments were carried out by using an SPR imager apparatus (GWC Technologies, USA). SPR images were analysed by using the V++ software (version 4.0, Digital Optics Limited, New Zealand) and the software package Image J 1.32j (National Institutes of Health, USA). SPRI provides data as pixel intensity units (0 – 255 scale). Data were converted into percentage of reflectivity (%R), or Δ%R in the case of difference images, by using the formula:

$$\%R = 100 \times \frac{0.85\, I_p}{I_s}$$

where I_p and I_s refer to the reflected light intensity detected using p- and s-polarized light, respectively. The experiments were carried out by sequentially acquiring 15 frames averaged SPR images with 10 s time delay between them. Kinetic data were obtained by plotting the difference in percent reflectivity (Δ%R) from selected regions of interest (ROIs) of the SPR images as a function of time. The selected ROIs were chosen in order to include all the SPR chip area involved by the surface interaction experiment. All the SPRI experiments were carried out at room temperature.

A microfluidic device was used for the analysis: it was fabricated in poly(dimethylsiloxane) (PDMS) polymer through the well-established replica molding technique. The microfluidic device is constituted by six parallel microchannels (80µm depth, 1.4cm length, 400µm width) and circular reservoirs (diameter = 400 µm) at the ends of each channel. PEEK tubes (UpChurch Scientific) were inserted in the circular reservoirs to connect the PDMS microfluidic cell to an Ismatec IPC (Ismatec SA, Switzerland) peristaltic pump. The microfluidic device was built by fixing the PDMS mold on the SPRI gold chip surface. A refractive index matching liquid was employed to obtain the optical contact between the flow cell and the prism.

A precise cleaning procedure for the fluidic system was used for minimizing contaminations and memory effects. The fluidic system was rinsed with ultraclean water (37 °C, for 2 h) after each experiment, and with PBS buffer for at least 1 h before each experiment. Every 3 weeks the system is cleaned as follow: 0.5% sodium dodecyl sulfate (SDS) (10 min), 6 M urea (10 min), 1% acetic acid (10 min), 0.2 M $NaHCO_3$ (10 min), ultraclean water 37 °C (30 min), PBS buffer (at least 1 h). To avoid artefacts generated by contaminations of the PDMS microfluidic device, normal and mutated DNA samples have been linked on PNAWT and PNA Mut modified surfaces by loading each of them into nearby microchannels, different for each experiment.

IV.1.4. Synthesis and functionalization of gold nanoparticles

All glassware used in the in the preparation and storage of AuNPs were firstly cleaned with aqua regia (3:1 HCl : HNO_3), then in a bath of freshly prepared piranha solution (1:3 30% H_2O_2: 96% H_2SO_4) and finally rinsed thoroughly in ultra-pure H_2O prior to use.

Gold nanoparticles were synthesized by citrate reduction of $HAuCl_4{\cdot}3H_2O$ according to methods described elsewhere. 20 mL of trisodium citrate (38.8 mM) was quickly added with vigorous stirring to 200 mL of a boiling solution of $HAuCl_4{\cdot}3H_2O$ (1 mM). The colour of the solution changed from pale yellow to deep red in few seconds. A complete reduction of trisodium citrate was obtained after 6-8 min upon boiling. The solution was cooled to the room temperature and filtered through a 0.45 µm mixed cellulose ester membrane filter. To prevent aggregation of the colloids, all colloidal gold solutions were stored in the dark and refrigerated at 4 °C. Similar conditions assured nanoparticles stability for several months.

AuNPs were characterized by UV-vis spectroscopy (Versawave-Expedeon Microvolume spectrophotometer). The mean diameter of AuNPs is 14.1±0.4 nm, measured through TEM technique.[350]

AuNPs were conjugated to the 3’ end of oligoDNA KRAS with a modified protocol of Streptavidin (SA) adsorption approach, and stability control was monitored for the purposes of their application for a long time in SPRI experiments.

The final concentration of oligoDNA KRAS conjugated AuNPs stock solutions was obtained from UV-vis spectroscopy (ε_{528} = 2×10^{8} $M^{-1}cm^{-1}$). Conjugated AuNPs stock solutions for the SPRI ultrasensitive detection have been characterized by λ_{max} = 528±1 nm, with a range of concentration between 10 and 30 nM. Conjugated AuNPs for SPRI signal enhancement were obtained by diluting oligoDNA KRAS conjugated AuNPs stock solutions. The selection of an appropriate oligoDNA KRAS conjugated AuNPs final concentration is critical for the success of the experiments. The described experiments were conducted using 0.1 nM solutions (in PBS).

IV.1.5. Genomic DNA sample treatments

Before SPRI experiments, genomic DNA samples were fragmented by sonication (3 min, ELMA Transsonic T480/H-2), vortexing (1 min, IKA Vortex GENIUS 3), and denatured by heating at 95 °C for 5 min. Genomic DNAs, randomly cut by sonication, produced fragments between 300 and 2000 bp. It has been reported that fragments of about 400 bp are optimal to localize the fragment within the human genome with a high degree of statistical certainty.[351] The possibility of strands re-association was limited by cooling on ice the samples (1 min) before their introduction into the SPRI microfluidics device.

SPRI genomic DNA hybridization experiments were carried out in an ice bath by flowing 5 pg μL^{-1} solutions of fragmented, and denatured gDNA at flow rate 10 $\mu L\ min^{-1}$ for 30 min in two parallel microchannels in contact with the PNA modified surface. Solutions of 5 pg μL^{-1} gDNAs were freshly prepared from stock solutions of gDNAs at 500 pg μL^{-1} (lifetime 48 h) before the experiments to guarantee the SPRI responses useful for samples discrimination. After that, the gDNA samples not reacted with the complementary and non-complementary PNA probes were flushed away by flowing PBS buffer at 10 $\mu L\ min^{-1}$ for 10 min.

IV.1.6. Amplification of SPRI signals by functionalized gold nanoparticles

The SPRI signal for the discrimination of gDNA samples was amplified by injecting the functionalized AuNPs at 15 $\mu L\ min^{-1}$ for 20 min, and PBS buffer was flowing at the same flow rate for 5 min to remove the unreacted gold nanoparticles.

To estimate the direct hybridization of gDNA solutions (WT and mutated) on PNA WT and PNA Mut functionalized surfaces, the mean $\Delta\%R_{PNA\ Mut}/\Delta\%R_{PNA\ WT}$ ratio values were obtained by considering Δ%R values after 1500 s of adsorption of conjugated AuNPs for replicated experiments. The ratio considers SPRI responses (Δ%R) referred to the PNA Mut probe ($\Delta\%R_{PNA\ Mut}$) and the PNA WT probe ($\Delta\%R_{PNA\ WT}$), respectively when the same DNA target was detected.

IV.2. Materials and Reagents

Reagents were obtained from commercial suppliers and used without further purification. N-α-Fmoc-S-trityl-L-cysteine (Fmoc-Cys(Trt)-OH) and N-α-Fmoc-l-glutamic acid γ-tert-butyl ester (Fmoc-Glu(OtBu)-OH) were purchased from Merck Millipore (The Netherlands).

As the solvents for the automated solid-phase peptide synthesis (SPPS) using Multisyntech GmbH instrument, 1-Hydroxybenzotriazole hydrate (HOBt), to dissolve the amino acid solutions, 2-(1H-benzotriazole-1-yl)-1,1,3,3-tetramethyluronium hexafluorophosphate (HBTU), N,N-diisopropylethylamine (DIPEA), N-methyl-2-pyrrolidone (NMP), piperidine, dichloromethane (DCM) and methanol were purchased from Sigma-Aldrich. For the manual cleavage and precipitation trifluoroacetic acid (TFA), triisopropylsilane (TIPS), 1,2-ethanedithiol (EDT) and diethyl ether solvents were obtained from Sigma-Aldrich (The Netherlands). Milli-Q water with a resistivity >18 MΩ·cm was used in all experiments.

IV.2.1. Synthesis of oligopeptide CEEEEE

The oligopeptide Cys-Glu-Glu-Glu-Glu-Glu (or CEEEEE) was synthesized by SPPS using the Fmoc-Glu(OtBu)-Wang resin (Sigma-Aldrich, The Netherlands). The linker attached to the polystyrene core is a 4-hydroxybenzyl alcohol moiety, modified with glutamate (OtBu)-OH used as the first amino acid.

The protocol consisted of five cycles of synthesis using single coupling mode for the first cycle, then the double coupling mode was actuated to ensure the complete activation of carboxyl groups, indispensable for speeding up the reaction. In every cycle, one glutamic acid was attached to the peptide sequence and the last amino acid was a cysteine residue. The active ester group for the carboxyl groups was introduced as a phosphonium salt of a non-nucleophilic anion (hexafluorophosphate) using HBTU/HOBt coupling activation and DIPEA/NMP solution. Thoroughly, four vials of the peptide were prepared by weighing 50 mg of Fmoc-Glu(OtBu)-Wang resin per vial. Thereafter, the resin was filled with NMP for the swelling phase for 2 h. Fmoc-Cys(Trt)-OH (0.29 M) and Fmoc-Glu(OtBu)-OH (0.29 M) were dissolved in 0.30 M HOBt/NMP solution, and 0.26 M of HBTU solution in NMP solvent for the coupling activation of the amino acids. Before the addition of the single amino acids, during each cycle of synthesis 20% of piperidine in NMP was used for removing the Fmoc protection group of the last amino acid in the sequence. This cleavage step was replicated for five cycles of synthesis. The peptide was rinsed with NMP, DCM and methanol (three cycles for three hours); then, the product was dried overnight under vacuum.

The cocktail cleavage for CEEEEE was composed with 94.75% TFA/2.5% TIPS/0.25% EDT/2.5% Milli-Q water. During the cleavage, the peptide was gently stirred for 4 h to avoid breaking the resin. Subsequently, the resin was rinsed with TFA, and all of the organic scavengers were removed using the rotavapor.

For the precipitation, diethyl ether was added to the peptide, and the sample was collected after three/four centrifugation steps. Afterwards, the precipitate was dissolved and treated with the lyophilization, after that the lyophilized product stored under Argon flow to prevent the oxidation of the peptide.

The purification of CEEEEE was performed using high-performance liquid chromatography (HPLC) on Water (2535) setup equipped with analytical and preparative XBridge C18 columns. The peptide solution was dissolved in H_2O with 0.1% TFA and purified by gradient elution method (linear gradient from H2O (99%) to acetonitrile (ACN, 100%)). The retention time of the oligopeptide was 10 min. The oligopeptide was characterized by mass spectrometry (Fig. S1).

IV.2.2.Synthesis of poly-L-lysine-g-maleimide(y%) (PLL-mal(y%))

Phosphate buffered saline tablets (PBS, pH 7.4), and poly-L-lysine·HBr (PLL·HBr) (15–30 kDa) were purchased from Sigma-Aldrich. (NHS)-tetra(ethylene glycol)-maleimide (NHS-(OEG_4)-mal) and Zeba™ Spin Desalting Columns (7 kD MWCO, 5 mL) were purchased from Thermo Fischer Scientific. ^1H-NMR and ^{13}C-NMR spectra were recorded on a Bruker 400 MHz spectrometer. Chemical shifts were reported in ppm with tetramethylsilane as an internal standard.

PLL-mal(y%) with different percentages (y%) of maleimide (from 13% to 26%) were synthesized with a modified procedure of Duan et al.[352] (Fig. S2). PLL·HBr in PBS buffer (pH 7.0), at a concentration of 10 mg mL^{-1}, was dissolved in 1 mL of PBS (pH 7.4), in order to obtain a final pH of 7.2. The double stoichiometric ratio of NHS-OEG_4-maleimide ester was added in sequence to the mixture, under vigorous stirring, and reacted for 4 h at room temperature. Thereafter, the crude mixture was purified using Zeba™ spin desalting columns. For the filtration, 2.5 mL of the desired buffer (PBS at pH 7) at 1000 rpm for 2 min (twice) was added and removed via centrifugation and finally, the polymer solution was filtered. The treated solution was immediately freeze-dried overnight. Afterwards, an NMR spectrum was recorded in D_2O with 5 µL of 0.1 M HCl using the water suppression sequence: ^{1}H NMR (400 MHz D_2O, pH 6.5) δ [ppm] = 1.26–1.55 ((lysine γ-CH_2), 1.63-1.83 (lysine β, δ-H_2), 3.00 (free lysine, H2N-CH2), 3.16 (OEG-maleimide, C(=O)-NH-CH_2-), 4.29 (lysine backbone, NH-CH-C(O)-), 6.86 (maleimide -C(=O)-CH-CH-C(=O)-) (Fig. S3-S5).

IV.2.3. Monolayers of PLL-mal(y%) and coupling reaction with CEEEEE

Gold sensors were cleaned by Piranha solution with a ratio of 3:1 (96% H_2SO_4: 30% H_2O_2) for 1 min, then rinsed with Milli-Q water for 20 min. Thereafter, the surfaces were activated by UV–ozone (UV/Ozone ProCleaner Plus, Bioforce Nanosciences) for 30 min and dipped in PLL-mal(y%) 0.5 mg mL^{-1} for 30 min. After the washing step with Milli-Q water, PLL-mal(y%) sensors were immersed in CEEEEE 1.0 mM solution for 16 h.

Water contact angle. The wettability of functionalized PLL-mal(y%) and PLL-mal(y%)-CEEEEE surfaces were characterized by water contact angle measurements. Contact angles were measured on a Krüss G10 contact angle setup equipped with a CCD camera. Each value was calculated as an average over three samples. Moreover, from each sample, at least three contact angle measurements have been taken and the average calculated. All measurements have been done with Milli-Q water, at room temperature.

PM-IRRAS measurements. Polarization modulation infrared reflection-absorption spectra (PM-IRRAS spectra) were recorded on PLL-mal(y%) and PLL-mal(y%)-CEEEEE surfaces with Nicolet FT-IR 6700 abs a TOM optical module (Thermo Scientific) equipped with a Photo Elastic Modulator (PEM, Hinds Instruments). Spectra were recorded with the p-polarized light incident at 82° relative to the surface normal, with the PEM wavenumber 1500, 2100 or 2900 cm^{-1}. 200 scans with a resolution of 4 cm^{-1} at room temperature were collected in each experiment. (Fig. 29, Fig. S6-S7).

IV.2.4. Immobilization of PLL-mal(y%)-CEEEEE monolayer and antifouling measurements by SPRI technique

Immobilization of PLL-mal(y%)-CEEEEE monolayer. A precise cleaning procedure for the fluidic system was used for minimizing contaminations and memory effects. The fluidic system was rinsed with ultraclean water (37 °C, for 2 h) after each experiment, and with PBS buffer for at least 1 h before each experiment.

SPRI gold sensors were rinsed with Milli-Q water, ethanol and dried under N_2 for few seconds. Thereafter, the surfaces were activated using UV-ozone for 30 min. The immobilization of the PLL-mal(y%) polymer in PBS buffer 0.01 M, containing 0.150 M NaCl, pH 7.4 was performed on the surface at 20 µL min^{-1} as flow constant rate for 15 min. PLL-mal(y%) polymer immobilization was followed by the washing step with the same PBS buffer for 10 min. Then, 1.0 mM of oligo CEEEEE in PBS buffer 0.01M pH 7.5 was immobilized at the same flow rate for 1 h and 10 min until the visible plateaux of oligo CEEEEE binding on PLL-mal(y%) film.

Antifouling measurements. The antifouling properties were assessed in adsorption studies by SPRI technique using BSA solutions (1.0 mg mL^{-1} and 50.0 mg mL^{-1}) in PBS buffer 0.01 M pH 7.4 as the standards (Table S4). An initial baseline was established by flowing PBS buffer for 5 min. Freshly prepared BSA solutions were flowed for 10 min to attain the adsorption plateaux. Then, PBS buffer was flowed through the system for 15 min to remove loosely attach protein and establish a final stable baseline. SPRI antifouling experiments were carried out using a flow rate of 50 µL min^{-1}. The same procedure was followed when diluted commercial human plasma samples (5%, 10%, 33%, from Zen-Bio, Inc. SER-PLE200ML-CUSTOM) were used to test the antifouling activity in the real complex medium.

Quantification of non-specific protein adsorption. Protein adsorption for BSA standard solutions was quantified by measuring the variation of reflected intensity ($\Delta\%R$) in SPRI system, after the injection of the protein. The mass of adsorbate per unit area (ng cm^{-2}) was calculated from the equation described by Shumaker-Parry et al.,[75] where the specific density for BSA is ρ_{BSA} = 1.3 g cm^{-3}, the refractive index of BSA is n_{BSA} = 1.57 and the refractive index of PBS buffer is n_{PBS} = 1.33. The value for the decay length l_d was considered as 37% of SPR wavelength.[353] For human plasma samples, the mass of adsorbate per unit area (ng cm^{-2}) was calculated from the equation described by Shumaker-Parry et al.,[75] where the specific density for plasma protein is ρ_{PP} = 1.42 g cm^{-3}, obtained by the average of the specific density of single plasma proteins,[354] the refractive index of plasma protein is n_{PP} = 1.53,[355] and the refractive index of PBS buffer is 1.33. The value for the decay length l_d was considered as 37% of SPR wavelength.[353] The sensitivity factor for SPRI systems was s = 6009.28 %R/RIU, calculated from the slope of the SPRI calibration curve. The mass density of PLL-mal(26%) and CEEEEE layers was calculated using the equation described by Shumaker-Parry et al.,[75] where the refractive index of the functionalized-PLL polymer is $n_{PLL\text{-}mal}$ = 1.52,[356] and the refractive index of PBS buffer is 1.33. A refractive index of CEEEEE of n_{CEEEEE} = 1.44 was considered on the basis of the model described by Zhao H. et al.[357] Molar ratio of CEEEEE to PLL-mal(y%) for the evaluation of the coupling efficiency reaction was calculated by dividing the areal mole (nmol cm^{-2}) of CEEEEE and PLL-mal(y%). The areal mole of CEEEEE was obtained by dividing the mass density values of CEEEEE for the molecular weight of the peptide. The areal mole for each PLL-mal(y%) was calculated by dividing the mass density of PLL-mal(y%) for the corresponding molecular weight of PLL-mal(y%) repeat unit (e.g. MW PLL-mal(26%) = 879.15 g mol^{-1}, MW PLL-mal(22%) = 969.36 g mol^{-1}, MW PLL-mal(13%) = 1375.31 g mol^{-1}).

IV.2.5. Immobilization of PLL-mal(y%)-CEEEEE and antifouling measurements by QCM-D technique

QCM-D apparatus. QCM-D measurements were conducted on a Q-Sense-E4 instrument (Q-Sense, Sweden) with dissipation. QCM-D chips (AT cut, 5 MHz, 14 mm diameter) were cleaned using basic Piranha solution (H_2O MilliQ: 30%H_2O_2: 25%NH_4OH 5:1:1) for 5 min, then rinsed with Milli-Q water, dried with N_2 stream and treated with UV-ozone for 10 min. Thereafter, the sensors were placed in the fluid chambers.

Immobilization of PLL-mal(y%)-CEEEEE monolayers. The immobilization of the PLL-mal(y%) polymer in PBS buffer 0.01M, containing 0.150 M NaCl, pH 7.4 was performed at 50 µL min^{-1} as flow constant rate for 15 min. PLL-mal(y%) polymer immobilization was followed by the washing step with PBS buffer for 10 min. Thereafter, 1.0 mM of oligopeptide CEEEEE in PBS buffer 0.01M pH 7.5 was immobilized at the same flow rate for 1 h and 40 min until the visible plateaux of CEEEEE binding on PLL-mal(y%) film. All QCM-D experiments were carried out at a temperature of 25 °C.

Antifouling measurements. The antifouling property was assessed in adsorption studies using BSA solutions using the same procedure above described for SPRI measurements All the antifouling tests by QCM-D instrument were carried out using a flow rate of 100 µL min^{-1}. The same procedure was followed when diluted commercial plasma samples (5%, 10%, 33%, from Zen-Bio, Inc. SER-PLE200ML-CUSTOM) were used to test the antifouling activity in the real complex medium.

Quantification of non-specific protein adsorption. The differences in frequency, Δf, between the two baselines were attributed to the protein adsorption, and the adsorbed mass was analysed by Sauerbrey equation using Q-tools software package v.3.0.15.553 (Biolin Sci, AB) on an average of 50 experimental points. The fifth overtone was considered for all the data calculations. As described before, the molar ratio of

CEEEEE to PLL-mal(y%) for the evaluation of coupling efficiency reaction was calculated by dividing the areal mole (nmol cm^{-2}) of CEEEEE and PLL-mal(y%).

IV.3. Materials and Reagents

PNA KRAS exon 2 Wild-Type (PNA WT), SPDP-dPEG$_4$-CTACGCCACCAGCT-Gly-NH$_2$; PNA KRAS exon 2 G12D (PNA G12D), SPDP-dPEG$_4$-CTACGCCATCAGCT-Gly- NH$_2$ were provided by University of Parma (Prof. R. Corradini group). Genomic DNA samples for KRAS exon 2 for the Wild-Type and G12D mutation (gDNA WT and G12D) were provided by Italian National Cancer Institute Regina Elena (Rome, Dr. P. Giacomini). The TCEP Disulfide Reducing Gel was purchased by Thermo Fisher Scientific. The oligopeptide CEEEEE was obtained by Selleckchem Company (> 95% of purity grade). Commercial human plasma, from pooled healthy donors, was purchased by Zen-Bio, Inc. SER-PLE200ML-CUSTOM. Phosphate buffered saline (PBS) solutions at pH 7.4 (137 mM NaCl, 2.7 mM KCl, phosphate buffered 10 mM) were obtained from VWR (Italy). SPRI gold chips were purchased from GWC Technologies (USA). Ultra-pure water (Milli-Q Element, Millipore) was used for all the experiments.

IV.3.1. PNA probe synthesis and PLL-mal(26%)-PNA surface immobilization

The PNA sequences were designed, synthesized by using automatic solid phase synthesis, purified and characterized as previously described.[348] An optimal surface probe density is needed in order to obtain consistent and reproducible SPRI results because an extremely dense surface decreases the sensitivity during the oligonucleotide hybridization step.

The PNA WT and PNA G12D probe were modified with N-Succinimidyl 3-(2-pyridyldithio)propionate (SPDP) at 5’-position in order to protect the thiol group in PNA sequences, and four OEG units (dPEG$_4$) were used as linkers to minimize surface effects caused by the steric hindrance of immobilized systems. Initially, PNA WT and PNA G12D were deprotected through the TCEP Disulfide Reducing Gel by following the procedure for the reduction of thiol groups in bath format. Briefly, a volume of 40 µL of TCEP Disulfide Reducing Gel was added to a microcentrifuge tube, centrifuged at 1000 g for 1 min at 25 °C and the supernatant was removed and discarded. Thereafter, repeated twice, the TCEP gel was washed by adding 20 µL of PBS buffer, vortexing briefly to resuspend the gel and by centrifuging at 1000 g for 1 min at 25 °C. Then, the supernatant was removed and discarded, and 20 µL of PNA probes were added in two separate washed gel. After vortexing the tubes, the different solutions were incubated for 15 min at 25°C on a rotating wheel to keep the gel in suspension. After the centrifugation at 25°C for 1 min, the supernatant containing the thiol-PNA probes was collected. The final concentration of thiol-PNA probes was determined by UV-vis spectroscopy at 260 nm.

SPRI gold sensors were rinsed with Milli-Q water, ethanol and dried under N_2 for few seconds. Thereafter, the surfaces were activated using UV-ozone for 10 min, and the immobilization of the PLL-mal(26%) polymer in PBS buffer was immediately performed on the surface at 20 µL min^{-1} as flow constant rate for 15 min. PLL-mal(26%) polymer in excess was flushed away by flowing PBS buffer for 10 min.

PNA WT and PNA Mut thiol-probes were immobilized on PLL-mal(26%) modified surface by thiol-maleimide Michael-type addition. The spatially separated immobilization of PNA probes was obtained by injecting PNA WT and PNA Mut solutions (0.1 µM in PBS, flow rate 10 µL min^{-1}) into parallel microchannels in contact with the PLL-mal(26%) modified gold surface. Thereafter, in order to assemble the antifouling coating, 1.0 mM of oligo CEEEEE in PBS buffer was immobilized at the same flow rate for 40 min until the visible plateaux of oligo CEEEEE binding on PLL-mal(26%)-PNA layer.

IV.3.2. Genomic DNA sample treatments and discrimination ctDNA samples by functionalized gold nanoparticles

Before the hybridization of the complementary PNA probes, genomic DNA samples were spiked in diluted human plasma (10%) at the final concentration of 5 pg $µL^{-1}$ and centrifuged at 10000 rpm (4°C) for 10 min. Solutions of 5 pg $µL^{-1}$ gDNAs were freshly prepared from stock solutions of gDNAs at 500 pg $µL^{-1}$ (lifetime 48 h) before the experiments to guarantee the correct discrimination by SPRI signals. Thereafter, the ctDNA in human plasma samples were treated following the procedure described in Section IV.1.4. for gDNA solutions.

SPRI hybridization experiments were carried out in an ice bath by flowing 5 pg $µL^{-1}$ solutions of fragmented and denatured ctDNA at flow rate 10 µL min^{-1} for 30 min in two parallel microchannels in contact with the PLL-mal(26%)-PNA modified surface.

IV.3.3. Amplification of SPRI signals by functionalized gold nanoparticles

Gold nanoparticles were synthesized and functionalized as described in Section IV.1.3. The SPRI signal for the discrimination of ctDNA samples was amplified by injecting the functionalized AuNPs at 15 µL min^{-1} for 15 min, and PBS buffer was flowing at the same flow rate for 5 min to remove the unreacted gold nanoparticles.

To evaluate the direct hybridization of gDNA solutions (WT and G12D), the mean $\Delta\%R_{PNA\ G12D}/\Delta\%R_{PNA\ WT}$ ratio values were obtained by considering Δ%R values after 1000 s of the adsorption of conjugated AuNPs for replicated experiments. The ratio considers SPRI responses (Δ%R) referred to the PNA Mut probe ($\Delta\%R_{PNA\ G12D}$) and the PNA WT probe ($\Delta\%R_{PNA\ WT}$), respectively when the same DNA target was detected.

IV.3.4. Antifouling measurements by SPRI technique for control experiments

The antifouling properties of PLL(no mal) layer, PLL(no mal) layer with PNA probes (PLL(no mal)–PNA), and PLL(no mal) layer with PNA probes and CEEEEE peptide (PLL(no mal)–PNA–CEEEEE) was studied by flowing 10% of human plasma for 30 min and PBS buffer after 10 min at 10 µL min^{-1}. Hence, the antifouling activity of the other components of the layer, which are PLL-mal(26%) and PLL-mal(26%)–PNA, was examined and compared with the entire layer PLL-mal(26%)–PNA–CEEEEE by flowing 10% of human plasma for 30 min and PBS buffer after 10 min at 10 µL min^{-1}. Finally, the antifouling property of PNA–CEEEEE film was examined and compared with PLL(no mal)–PNA–CEEEEE and PLL-mal(26%)–PNA–CEEEEE layers, by flowing 10% of human plasma for 30 min and PBS buffer for 10 min at 10 µL min^{-1}. All diluted plasma samples were only centrifuged following the above-described procedure genomic DNA samples (Section IV.3.2.)

Chapter V

Results and Discussion

This chapter reports the experimental results obtained in this PhD project. Initially, a detailed description of the strategy adopted for the ultrasensitive detection of non-amplified genomic DNA (gDNA), with single point mutations in KRAS gene exon 2, using nanoparticle-enhanced SPRI assay was provided. After preliminary results of nanoparticle-enhanced SPRI assay for the detection of gDNA KRAS mutations, I performed the development of new mixed-charge polymer based on PLL modified with an anionic peptide suitable for medical diagnostics. The peptide chains were connected to the polymer via a non-ionic OEG spacer, in order to achieve control over the charge distribution of PLL-coated surfaces and thus antifouling character. Hence, I realized a novel nanoparticle-enhanced SPRI assay for ctDNA detection, carrying KRAS gene mutation, in human plasma samples using PLL-mal(y%)-CEEEEE layer as antifouling coating. The experimental data confirm the designed nanoparticle-enhanced SPRI assay for the detection of ctDNA in real samples would be able to discriminate the KRAS single point mutation from genomic sequences of healthy donors, directly in biological fluids at attomolar level.

V. Results and Discussion – part I

V.1. Development of nanoparticle-enhanced SPRI assay for gDNA KRAS mutations

Scheme 1 shows the strategy adopted for the ultrasensitive detection of non-amplified genomic DNA (gDNA), with single point mutations in KRAS gene exon 2, using nanoparticle-enhanced SPRI assay.

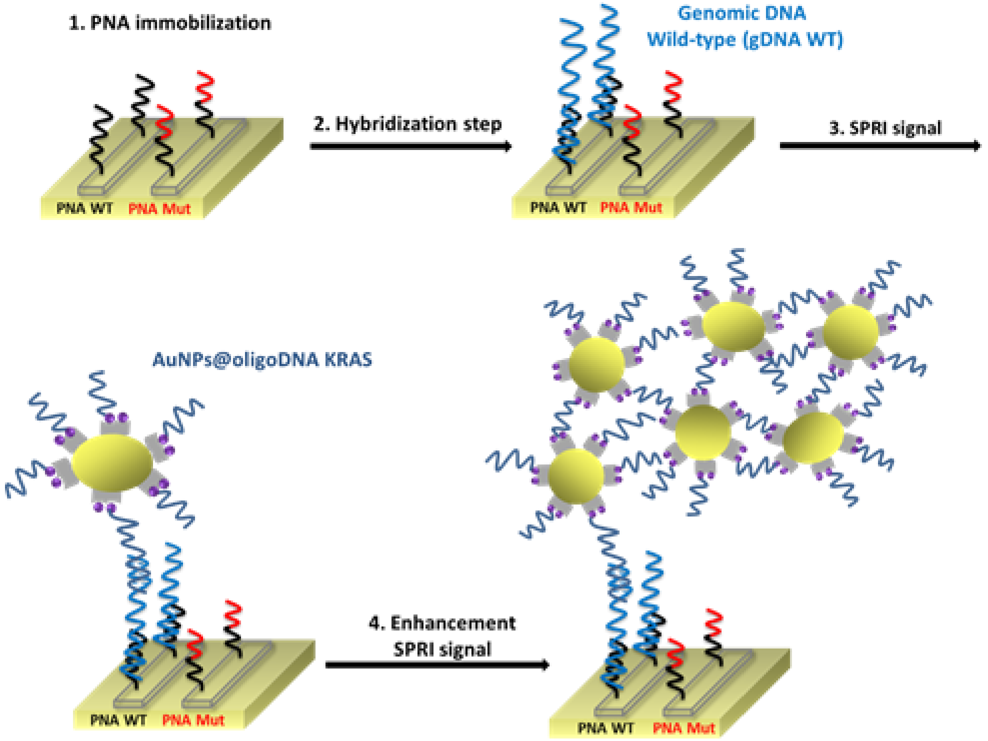

Scheme 1. Pictorial representation of nanoparticle-enhanced SPRI assay for the detection of gDNA KRAS exon 2: Wild-Type and mutated target. To simplify the representation only specific adsorbed DNA is shown. PNA WT and PNA Mut specifically recognize the wild-type and mutated genomic sequences, respectively.

First of all, an accurate control of the immobilization of PNA WT and PNA Mut (G12D, G12V, or G13D) probes onto SPR sensor has been preliminary performed (Scheme 1, step 1), in terms of the molecular probe density attached to the surface, to guarantee the successful gDNA detection. Steric hindrance caused by high surface density values, which are related to the change of percent reflectivity (Δ%R) over time, affects the following hybridization step, while too low surface density values limit the number of vacant sites for gDNA fragments anchoring.

Figure 20 shows representative SPR immobilization curves of PNA WT and PNA Mut (PNA G12D) probes on the gold substrate at concentrations of 0.1 µM.

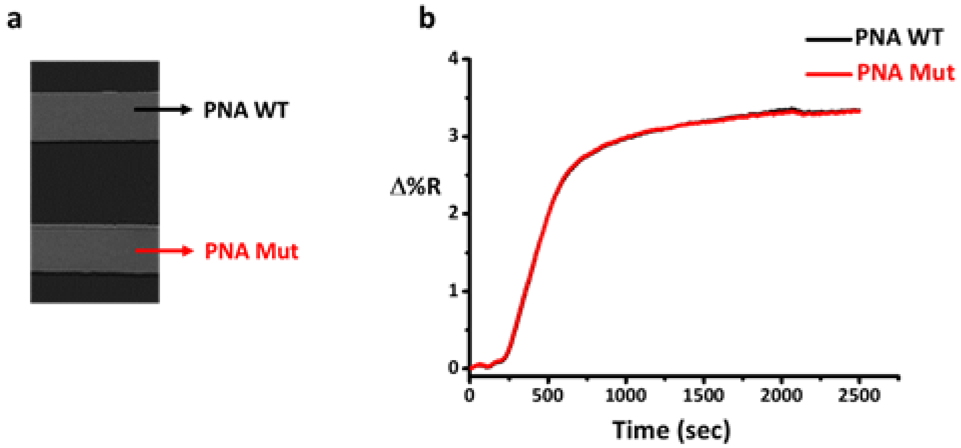

Figure 20. (a) Typical SPR difference image of immobilization of PNA probes in two parallel channels. (b) Representative SPRI curve, in percent reflectivity (Δ%R) over time, of the immobilization of PNA WT and PNA Mut (G12D) probes (0.1 µM in PBS, flow rate 10 µL min^{-1}).

As reported in Figure 20 (a), a homogeneous PNA immobilization was obtained when the reflectivity values, displayed in grayscale of SPR difference image, were similar for both PNA probes. Moreover, the optimal range of molecular probes density was determined between 2 and 3 Δ%R values by flowing PBS buffer after the PNA immobilization step (Fig.20 b).

The genomic DNA samples were extracted from blood samples of healthy donors and cancer patients and diluted to 5 pg µL^{-1} before the analysis.

Typical experiments were carried out by detecting multiplex responses using an SPRI microfluidic device assembled by six parallel channels. An exact volume of gDNA samples (300 µL) directly flowed into the SPRI device to allow the direct interaction of each of the three specimens with both PNA WT and PNA Mut functionalized surfaces (Scheme 1, step 2). Specifically, the design of SPRI experiments included control channels, where the direct hybridization between gDNA samples and corresponding PNA probes (i.e., for G12D mutation PNA WT/DNA WT or PNA G12D/DNAG12D) occurred and mismatch channels, where the binding between gDNA samples and PNA probes was not to be expected (i.e., PNA WT/DNA G12D or PNA G12D/DNAWT) (Fig. 21).

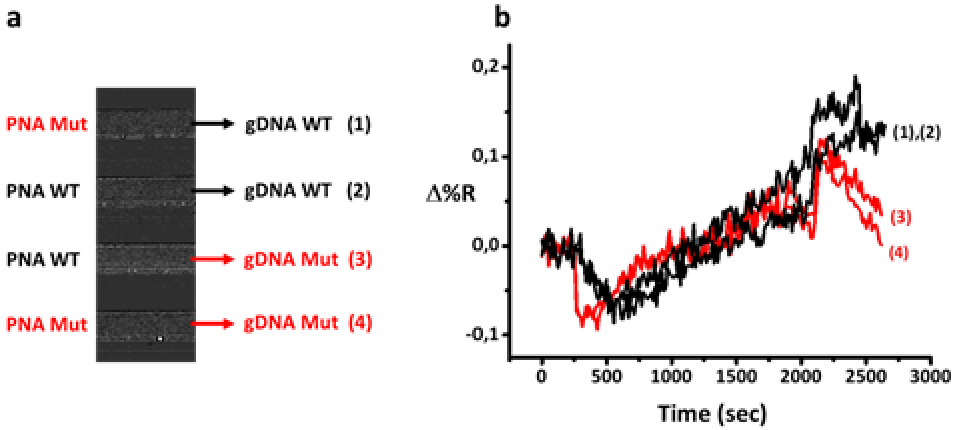

Figure 21. (a) SPR difference image of gDNA hybridization in control channels ((2),(4)) and mismatch channels ((1),(3)). PNA G12D and gDNA G12D were employed as PNA Mut and gDNA Mut, respectively. (b) Typical SPRI curves, in percent reflectivity (Δ%R) over time, of gDNA hybridization in control channels ((2),(4)) and mismatch channels ((1),(3)) using 5 pg μL^{-1} of gDNA samples. No signal useful for sample discrimination is observed at this stage of the assay.

The direct interaction of the above-mentioned 5 pg μL^{-1} gDNA solutions on PNA WT and PNA Mut probes generate an SPRI signal close to the instrumental noise with no evident variation in Δ%R, as reported for gDNA WT/G12D (Fig.21 a). I found that the observed signal trend (Fig.21 b) is in line with the literature for similar assays.[52,100]

The ultrasensitive detection of the gDNA target hybridization was obtained by using AuNPs conjugated with an oligonucleotide complementary to a small region of the target gDNA not involved in the hybridization step. Functionalized AuNPs were adsorbed on surfaces (0.1 nM in PBS, flow rate 15 $\mu L\ min^{-1}$, exact volume 900 µL), where the direct hybridization with the complementary gDNA sequence arose (Scheme 1, step 3). By flowing the conjugated AuNPs into the microchannels so as to have a specific control of the detection target gDNA through gold nanoparticles, a significant increase in SPRI signals was obtained (Scheme 1, step 4).

Figure 22 shows the experimental results for ultrasensitive detection of gDNA hybridization, after the adsorption of conjugated AuNPs, for G12D KRAS gene mutation.

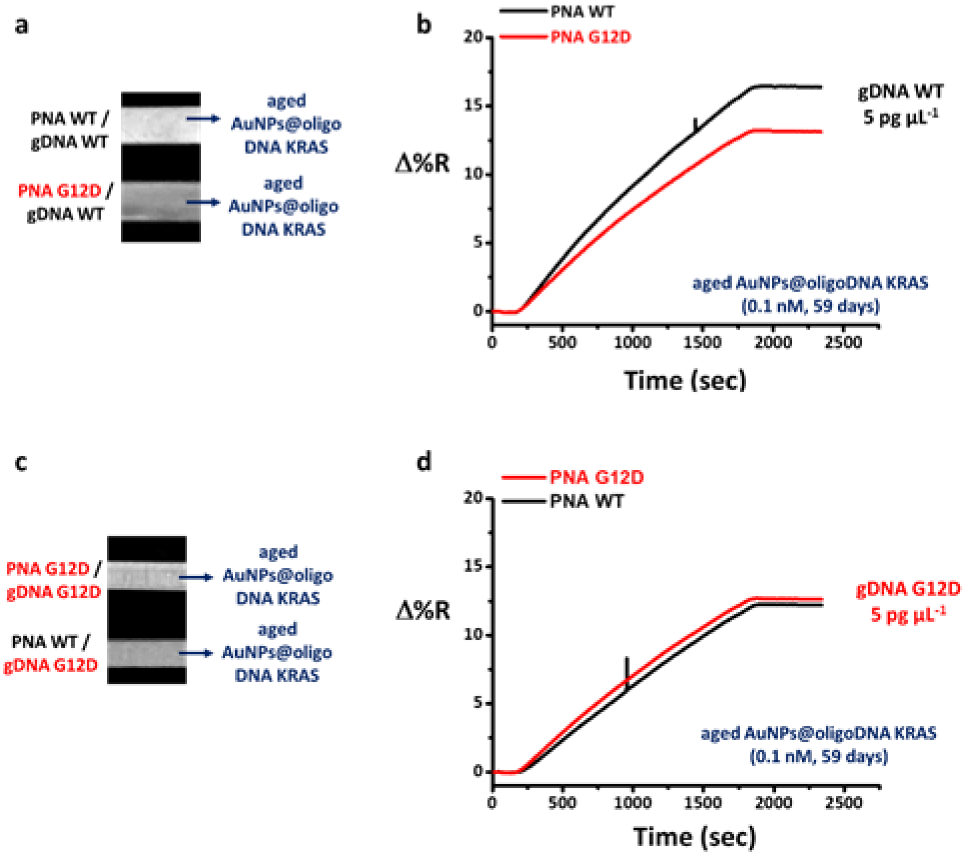

Figure 22. (a) SPR difference image after the adsorption of conjugated AuNPs on PNA WT/gDNA WT control channel and PNA G12D/gDNA WT mismatch channel. (b) Representative time-dependent SPRI curves obtained after the interaction of conjugated AuNPs on PNA WT/gDNA WT control channel and PNA G12D/gDNA WT mismatch channel. (c) SPR difference image after the adsorption of conjugated AuNPs on PNA G12D/gDNA G12D control channel and PNA WT/gDNA G12D mismatch channel. (d) Representative time-dependent SPRI curves obtained after the interaction of conjugated AuNPs on PNA G12D/gDNA G12D control channel and PNA WT/gDNA G12D mismatch channel. gDNA WT and G12D samples were previously adsorbed to the surface immobilized PNA WT (black curves) and PNA G12D (red curves). 5 pg µL^{-1} solutions of gDNAs and 0.1 nM of AuNPs-conjugated were used in three independent experiments.

The detected SPRI responses were in accordance with those expected for gDNA WT hybridization, by recording a remarkable discrimination between target and non-target DNA sequences (Fig.22 b). Basically, gDNA WT preferentially hybridizes with the complementary PNA WT probe, while the interaction of mismatch sequences is prevented, as indicated in SPR difference image after the adsorption of conjugated AuNPs where the brightness of control channel is much higher than that of mismatch channel (Fig.22 a). Differently, after the interaction of functionalized AuNPs for the detection of gDNA G12D, the brightness of the control channel is slightly higher than that of the mismatch channel (Fig.22 c).

A small discrimination between target and non-target DNA sequences for G12D mutation was achieved by using this assay (Fig.22 d).

Figure 23 shows the average results from replicate experiments carried out by using genomic DNAs from healthy donors and cancer patients with G12D KRAS gene mutation.

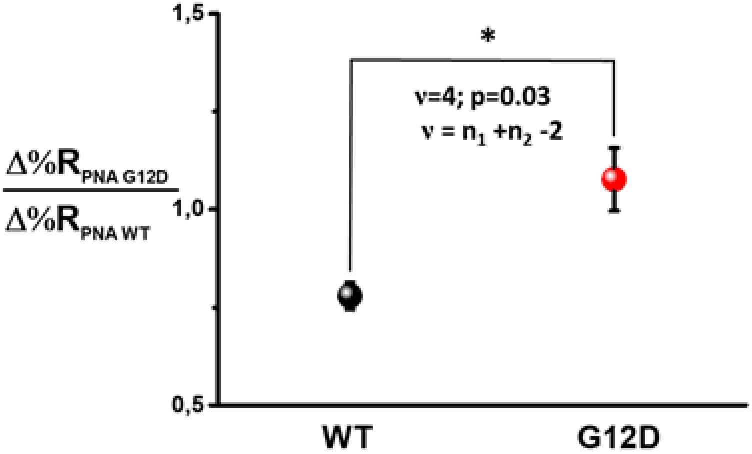

Figure 23. Mean $\Delta\%R_{PNA\ G12D}/\Delta\%R_{PNA\ WT}$ ratio values obtained from three replicated experiments aimed at detecting 5 pg μL^{-1} solutions of WT and G12D non-amplified genomic DNAs. Ratios were obtained by considering Δ%R values after 1500 s of adsorption of conjugated AuNPs. The ratio considers SPRI responses (Δ%R) referred to the PNA G12D probe ($\Delta\%R_{PNA\ G12D}$) and the PNA WT probe ($\Delta\%R_{PNA\ WT}$), respectively when the same DNA target was detected. gDNA WT (mean $\Delta\%R_{PNA\ G12D}/\Delta\%R_{PNA\ WT}$ = 0.78, confidence interval at the 95% level CI = 0.78 (0.03, replicate measurements n_1 = 3) and gDNA G12D (mean $\Delta\%R_{PNA\ G12D}/\Delta\%R_{PNA\ WT}$ = 1.08, CI = 1.08 (0.08, replicate measurements n_2 = 3) generated significantly different $\Delta\%R_{PNA\ G12D}/\Delta\%R_{PNA\ WT}$ ratio (two-tailed t-test, level 95%, P = 0.03). Error bars represent the 95% confidence interval (CI) of the mean. The asterisk (*) indicate statistically different values.

The ratio between the SPRI responses (Δ%R) is referred to the PNA G12D probe ($\Delta\%R_{PNA\ G12D}$) and the PNA WT probe ($\Delta\%R_{PNA\ WT}$) when the same DNA target was detected. gDNA WT and gDNA G12D samples generated $\Delta\%R_{PNA\ G12D}/\Delta\%R_{PNA\ WT}$ ratios significantly different (two-tailed t-tests, level 95%, P = 0.03). These preliminary results confirm the designed nanoparticle-enhanced SPRI assay for the detection of gDNA G12D would be able to discriminate the KRAS single point mutation from genomic sequences of healthy donors at attomolar level.

Similar tests were carried out for G12V mutation, where the experimental results for ultrasensitive detection of gDNA hybridization after the adsorption of conjugated AuNPs is reported in Figure 24.

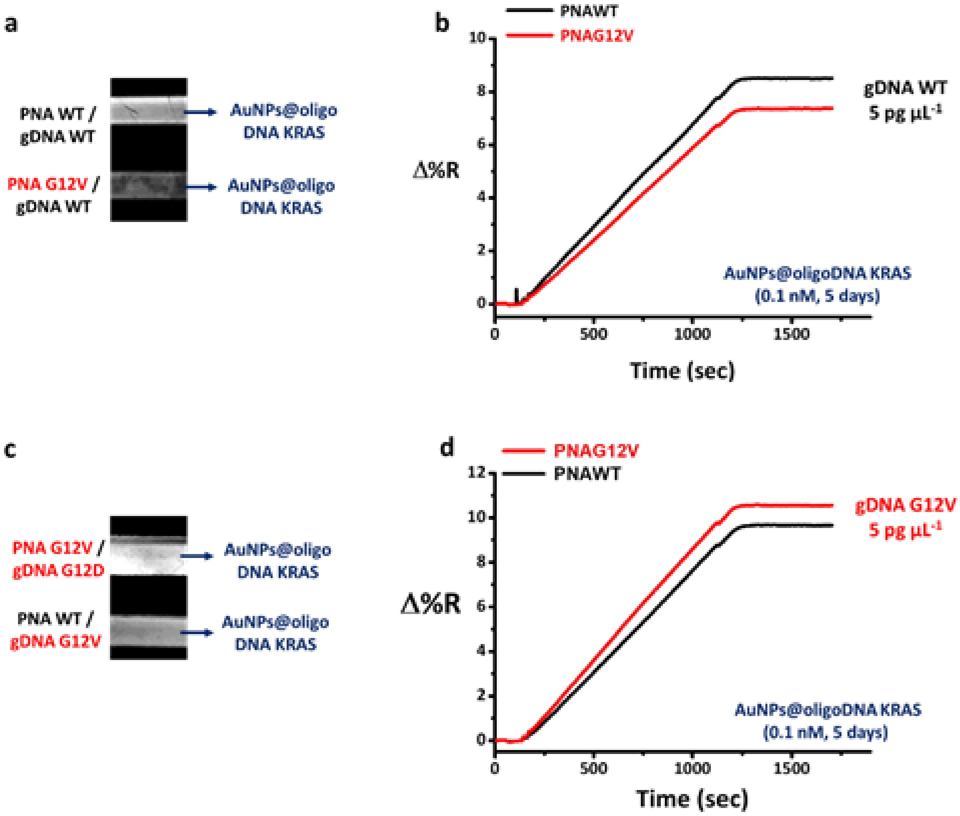

Figure 24. (a) SPR difference image after the adsorption of conjugated AuNPs on PNA WT/gDNA WT control channel and PNA G12V/gDNA WT mismatch channel. (b) Representative time-dependent SPRI curves obtained after the interaction of conjugated AuNPs on PNA WT/gDNA WT control channel and PNA G12V/gDNA WT mismatch channel. (c) SPR difference image after the adsorption of conjugated AuNPs on PNA G12V/gDNA G12V control channel and PNA WT/gDNA G12V mismatch channel. (d) Representative time-dependent SPRI curves obtained after the interaction of conjugated AuNPs on PNA G12V/gDNA G12V control channel and PNA WT/gDNA G12V mismatch channel. gDNA WT and G12V samples were previously adsorbed to the surface immobilized PNA WT (black curves) and PNA G12V (red curves). 5 pg µL^{-1} solutions of gDNAs and 0.1 nM of AuNPs-conjugated were used in three independent experiments.

The detected SPRI responses were in line with those supposed for gDNA WT hybridization, by measuring a good discrimination between target and non-target DNA sequences (Fig.24 b). Essentially, gDNA WT preferentially hybridizes with the complementary PNA WT probe, while the interaction of mismatch sequences is disadvantaged, as shown in SPR difference image after the adsorption of conjugated AuNPs where the light intensity of control channel is slightly higher than that of mismatch channel (Fig.24 a). Conversely, the brightness of the gDNA G12V control channel is more intense than that of mismatch channel after the interaction of functionalized AuNPs (Fig.24 c); thereby a significant discrimination between target and non-target DNA sequences for G12V mutation was gained through nanoparticle-enhanced SPRI assay (Fig.24 d).

Figure 25 exhibits the average results from replicate experiments achieved by using genomic DNAs from healthy donors and cancer patients with G12V KRAS gene mutation.

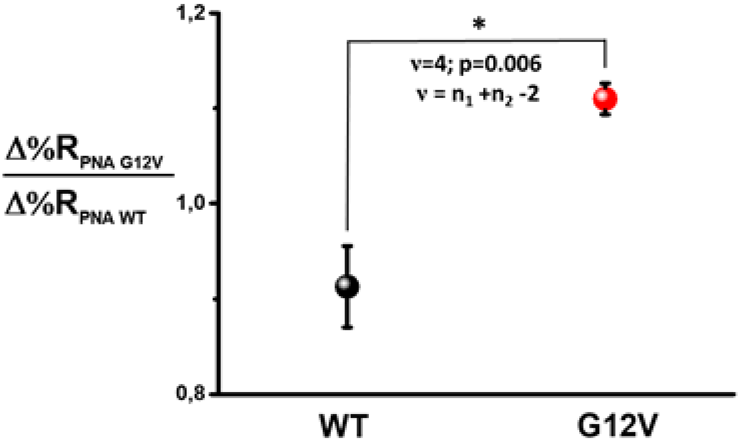

Figure 25. Mean $\Delta\%R_{PNA\ G12V}/\Delta\%R_{PNA\ WT}$ ratio values obtained from three replicated experiments aimed at detecting 5 pg μL^{-1} solutions of WT and G12V non-amplified genomic DNAs. Ratios were obtained by considering Δ%R values after 1500 s of adsorption of conjugated AuNPs. The ratio considers SPRI responses (Δ%R) referred to the PNA G12V probe ($\Delta\%R_{PNA\ G12V}$) and the PNA WT probe ($\Delta\%R_{PNA\ WT}$), respectively when the same DNA target was detected. gDNA WT (mean $\Delta\%R_{PNA\ G12V}/\Delta\%R_{PNA\ WT}$ = 0.91, confidence interval at the 95% level CI = 0.91 (0.04, replicate measurements n_1 = 3) and gDNA G12V (mean $\Delta\%R_{PNA\ G12V}/\Delta\%R_{PNA\ WT}$ = 1.11, CI = 1.11 (0.02, replicate measurements n_2 = 3) generated a $\Delta\%R_{PNA\ G12V}/\Delta\%R_{PNA\ WT}$ ratio which difference is very statistically significant (two-tailed t-test, level 95%, P = 0.006). Error bars represent the 95% confidence interval (CI) of the mean. The asterisk (*) indicate statistically different values.

The ratio between the SPRI responses (Δ%R) is referred to the PNA G12V probe ($\Delta\%R_{PNA\ G12V}$) and the PNA WT probe ($\Delta\%R_{PNA\ WT}$) when the same DNA target was revealed. gDNA WT and gDNA G12V samples generated $\Delta\%R_{PNA\ G12V}/\Delta\%R_{PNA\ WT}$ ratios significantly different (two-tailed t-tests, level 95%, P = 0.006). This preliminary outcome would prove that nanoparticle-enhanced SPRI assay for the detection of gDNA G12V distinguishes the KRAS single point mutation from genomic sequences of healthy donors at attomolar level with a statistically significant discrimination.

Also, the designed nanoparticle-enhanced SPRI assay was applied for the detection of another KRAS gene mutation of colorectal cancer, gDNA G13D (Fig.26).

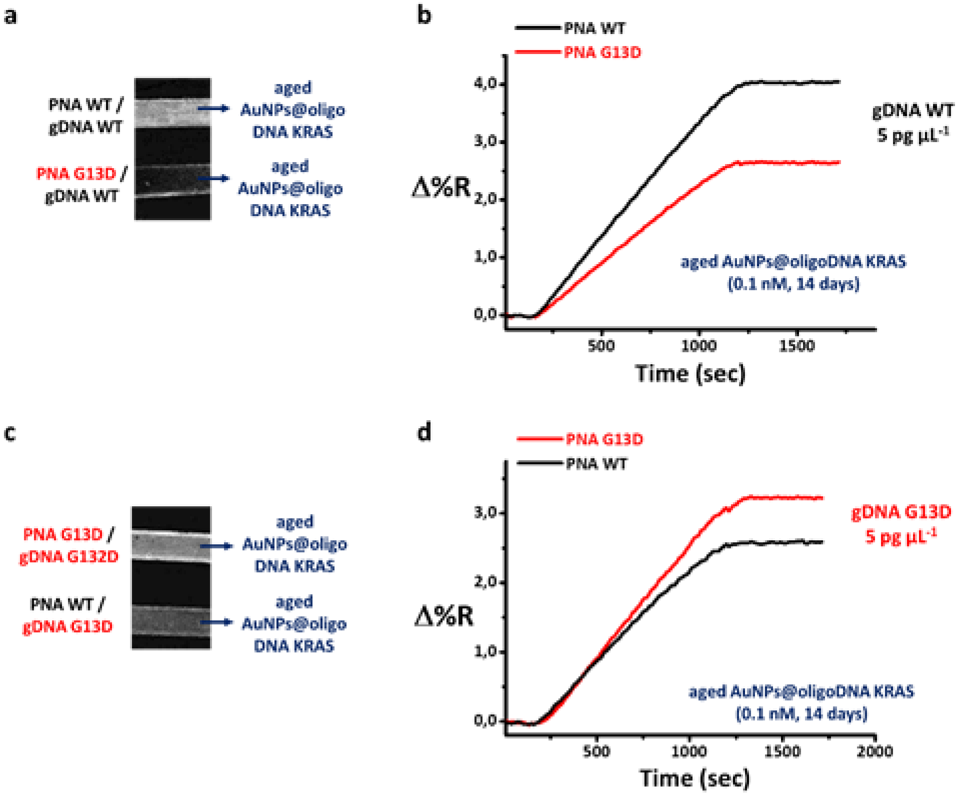

Figure 26. (a) SPR difference image after the adsorption of conjugated AuNPs on PNA WT/gDNA WT control channel and PNA G13D/gDNA WT mismatch channel. (b) Representative time-dependent SPRI curves obtained after the interaction of conjugated AuNPs on PNA WT/gDNA WT control channel and PNA G13D/gDNA WT mismatch channel. (c) SPR difference image after the adsorption of conjugated AuNPs on PNA G13D/gDNA G13 control channel and PNA WT/gDNA G13D mismatch channel. (d) Representative time-dependent SPRI curves obtained after the interaction of conjugated AuNPs on PNA G13D/gDNA G13D control channel and PNA WT/gDNA G13D mismatch channel. gDNA WT and G13D samples were previously adsorbed to the surface immobilized PNA WT (black curves) and PNA G13D (red curves). 5 pg µL^{-1} solutions of gDNAs and 0.1 nM of AuNPs-conjugated were used in three independent experiments.

Similarly to previous SPRI signals, a prominent discrimination between target and non-target DNA sequences was measured for gDNA WT (Fig.26 b), which preferentially interacts with the complementary PNA WT probe thus hindering the hybridization with mismatch sequences. As shown in SPR difference image after the adsorption of conjugated AuNPs (Fig.26 a), the light intensity of control channel is much higher than that of mismatch channel, by confirming the specificity of gDNA WT hybridization with its complementary probe. Also, the brightness of the gDNA G13D control channel is stronger than that of mismatch channel after the interaction of functionalized AuNPs (Fig.26 c) and, consequently, a significant discrimination between target and non-target

DNA sequences for G13D mutation was recorded by using nanoparticle-enhanced SPRI assay (Fig.26 d).

Figure 27 exhibits the average results from replicate experiments obtained by using genomic DNAs from healthy donors and cancer patients with G13D KRAS gene mutation.

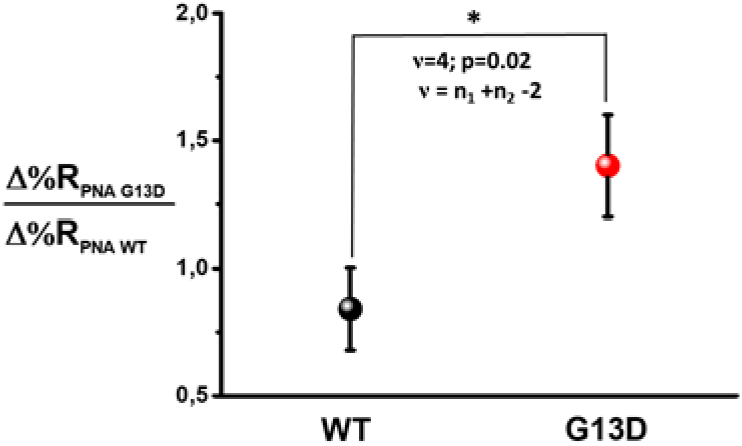

Figure 27. Mean $\Delta\%R_{PNA\ G13D}/\Delta\%R_{PNA\ WT}$ ratio values obtained from three replicated experiments aimed at detecting 5 pg µL^{-1} solutions of WT and G13D non-amplified genomic DNAs. Ratios were obtained by considering Δ%R values after 1500 s of adsorption of conjugated AuNPs. The ratio considers SPRI responses (Δ%R) referred to the PNA G13D probe ($\Delta\%R_{PNA\ G13D}$) and the PNA WT probe ($\Delta\%R_{PNA\ WT}$), respectively when the same DNA target was detected. gDNA WT (mean $\Delta\%R_{PNA\ G13D}/\Delta\%R_{PNA\ WT}$ = 0.91, confidence interval at the 95% level CI = 0.84 (0.16, replicate measurements n_1 = 3) and gDNA G13D (mean $\Delta\%R_{PNA\ G13D}/\Delta\%R_{PNA\ WT}$ = 1.40, CI = 1.40 (0.20, replicate measurements n_2 = 3) generated a $\Delta\%R_{PNA\ G13D}/\Delta\%R_{PNA\ WT}$ ratio which difference is statistically significant (two-tailed t-test, level 95%, P = 0.02). Error bars represent the 95% confidence interval (CI) of the mean. The asterisk (*) indicate statistically different values.

The ratio between the SPRI responses (Δ%R) is referred to the PNA G12V probe ($\Delta\%R_{PNA\ G13D}$) and the PNA WT probe ($\Delta\%R_{PNA\ WT}$) when the same DNA target was discriminated. gDNA WT and gDNA G13D samples generated $\Delta\%R_{PNA\ G13D}/\Delta\%R_{PNA\ WT}$ ratios significantly different (two-tailed t-tests, level 95%, P = 0.02). This preliminary outcome would prove that nanoparticle-enhanced SPRI assay for the detection of gDNA G13D differentiaties the KRAS single point mutation from genomic sequences of healthy donors at attomolar level with a good discrimination.

I also investigated the ageing of functionalized AuNPs (from 5 days to 2 months) by testing them against SPRI experiments aimed at detecting 5 pg µL^{-1} gDNA WT solutions (Fig.28 a,b).

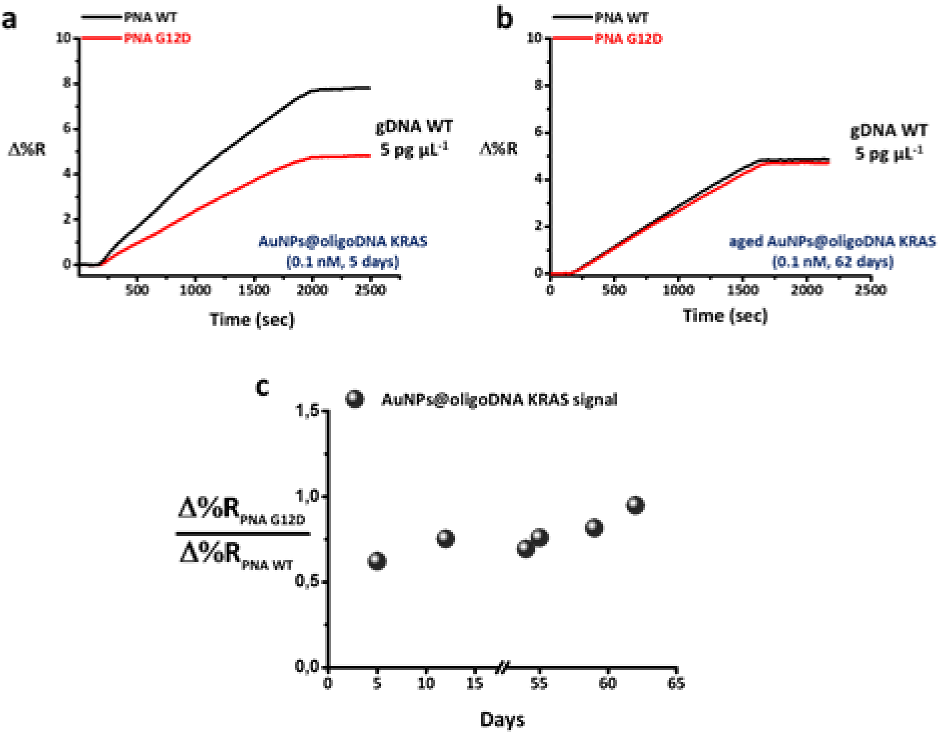

Figure 28. (a) Time-dependent SPRI curves obtained after the interaction of freshly functionalized AuNPs (5 days) on PNA WT/gDNA WT control channel and PNA G12D/gDNA WT mismatch channel. (b) Time-dependent SPRI curves obtained after the interaction of aged functionalized AuNPs (62 days) on PNA WT/gDNA WT control channel and PNA G12D/gDNA WT mismatch channel. DNAs previously adsorbed to the surface immobilized PNA WT (black curves) and PNA G12D (red curves) probes. 5 pg μL^{-1} solutions of genomic DNAs and 0.1 nM of freshly or aged functionalized AuNPs were used for the experiments. (c) $\Delta\%R_{PNAG12D}/\Delta\%R_{PNAWT}$ ratio values versus time of functionalization for AuNPs-conjugated (from 5 days to 2 months). Ratios were obtained by considering Δ%R values after 1500 sec of adsorption of conjugated AuNPs. The ratio considers SPRI responses (Δ%R) referred to the PNA G12D ($\Delta\%R_{PNA\ G12D}$) and the PNA WT ($\Delta\%R_{PNA\ WT}$) probes, respectively, when the same DNA WT target was detected.

As shown in Figure 28 (c), freshly functionalized AuNPs produce an excellent discrimination between SPRI signal detected from the control channel and mismatch channel, as expected. Moreover, the $\Delta\%R\ PNA_{G12D}/\Delta\%R\ PNA_{WT}$ ratios, calculated when the same target DNA WT was detected, are similar until 55 days by indicating the great stability of the conjugated AuNPs for a long-term application in nanoparticle-enhanced SPRI platform. After 55 days, the aged functionalized AuNPs show a slight increase of $\Delta\%R\ PNA_{G12D}/\Delta\%R\ PNA_{WT}$ ratios and, thereby, the specificity for gDNA WT discrimination was reduced.

Promising experimental data for the detection of G12D, G12V and G13D KRAS gene mutations using nanoparticle-enhanced SPRI ultrasensitive platform indicate that the strategy here described allows discriminating single point mutations in gDNA sequences of cancer patients, compared to those of healthy donors, with good specificity for all of three mutations by only using non-amplified target DNA at attomolar concentration. These results encourage additional studies for the optimization of the experimental procedure; for example, further advances could be made for the functionalization method of gold nanoparticles, in order to raise the number of initial AuNP aggregates onto SPRI surface and favour SPRI signal discrimination (Scheme 1, step 4). As demonstrated in literature,[52] nanoparticle-enhanced SPRI ultrasensitive detection of genomic DNA takes advantage of both the specific properties of PNA probes and the use of properly functionalized AuNPs and requires an accurate balancing between the number of surface immobilized probes, the number of target molecules, and the conjugated AuNP concentration. The analysis for a limited number of conjugated AuNPs specifically adsorbed, as a consequence of the hybridization reaction between oligoDNAKRAS on AuNPs surface and the complementary target sequence, is expected to increase the sites of aggregation for AuNPs and guarantee an optimal SPRI signal discrimination.

However, this nanoparticle-enhanced SPRI assay could be already applied the ultrasensitive detection of non-amplified ctDNAs in human blood with single point mutations in KRAS gene for the early diagnosis of colorectal cancer.

V. Results and Discussion – part II

V.2. Antifouling layer based on peptide-PLL polymer

After preliminary results of nanoparticle-enhanced SPRI assay for the detection of genomic DNA with single point mutations in KRAS gene exon 2, I performed the development of new mixed-charge polymer based on PLL modified with an anionic peptide, in order to have a sensor surface with multiple functionalities and, at the same time, an antifouling character.

Positive charges of the PLL backbone play a key role in the immobilization of functionalized PLL polymers on negatively charged surfaces. Functionalized PLL layers tend to lose their adhesive properties with increasing grafting density of OEG-maleimide chains, and 60% (or more) of free lysine is required for tightly anchoring the positively charged polymer to the activated negatively charged substrates.[352] Therefore, only a limited amount of OEG-maleimide chains can be added to PLL without altering the capacity of the whole system to properly immobilize on surfaces. Here, I synthesized PLL-mal(y%) with different percentages of OEG-maleimide (y% ranging from 13% to 26%), to allow coupling with a cysteine-modified peptide by the thiol–maleimide Michael-type addition. To preserve the PLL-mal(y%) capacity to interact with gold, y% values no greater than 26% were considered in this Thesis.

The protocol of the synthesis for PLL polymers was adapted from a procedure described elsewhere (Fig. S2),[352] and the process was carried out under controlled pH conditions to prevent the degradation of the maleimide moiety (pH 7.5). After the modification with different percentages of maleimide units, the grafting density of PLL-mal(y%) polymers was calculated using ^{1}H NMR (Fig. S3-S5). The anionic peptide CEEEEE was synthesized through the automated solid-phase peptide synthesis (SPPS) and then characterized by HPLC-MS (Fig. S1).

Scheme 2 shows a representation of the two-step formation of PLL-mal(y%)-CEEEEE polymers on a gold chip. After the activation of the gold surface by UV-ozone, PLL-mal(y%) polymers were adsorbed on the substrate via electrostatic interactions between the positively charged polymer backbone and the negatively charged surface (Scheme 2, step 1). Thereafter, the anionic peptide CEEEEE has been coupled to the maleimide units of the adsorbed PLL-mal(y%) polymers through the thiol–maleimide Michael-type addition employing the cysteine residue of the CEEEEE sequence (Scheme 2, step 2).

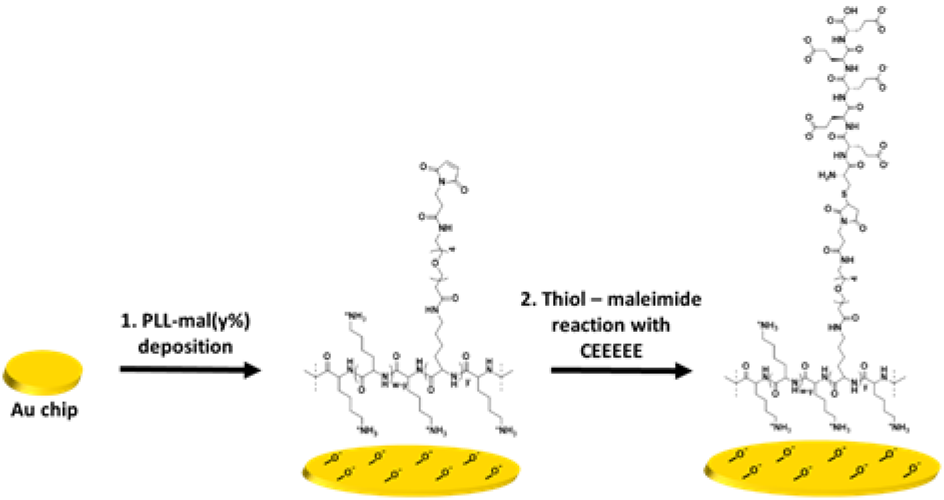

Scheme 2. Immobilization of the PLL-mal(y%) polymers on gold surface (1), the thiol-maleimide reaction between anionic peptide CEEEEE and maleimide units of immobilized PLL-mal(y%) polymers (2).

Water contact angle and PM-IRRAS measurements were used to evaluate the wettability of the substrates and to characterize the PLL-mal(y%)-CEEEEE monolayer deposited on the gold surface. Table 4 shows results from static water contact angle measurements of Au bare, PLL-mal(y%) layers with different percentages of maleimide units (y%, from 13% to 26%), and PLL-mal(y%)-CEEEEE layers after the coupling reaction of CEEEEE.

Table 4. Water contact angle data θ (°) of gold surfaces (Au bare), PLL-mal(y%) layers, and PLL-mal(y%)-CEEEEE layers. Three independent experiments were conducted for each step. Errors indicate the standard deviation.[a]

Surfaces	**(y%) = 26%** **θ (°)[a]**	**(y%) = 22%** **θ (°)[a]**	**(y%) = 13%** **θ (°)[a]**
Au bare		86 ± 1	
PLL-mal(y%)	31 ± 1	32 ± 1	31 ± 1
PLL-mal(y%)-CEEEEE	55 ± 2	53 ± 2	50 ± 1

Upon adsorption of PLL-mal(y%) on the gold surfaces, the contact angle decreased from 86° to 31° for all PLL-mal polymers tested, irrespective of the degree of maleimide functionalization (ranging from 13-26%). The low values for the PLL-mal layers indicate a high hydrophilicity of all PLL-mal(y%) surfaces, and the values correspond to values observed before.[352] The coupling reaction of CEEEEE to the PLL-mal(y%) layers induced an increase in the contact angle values, for most degrees of functionalization reaching 50° to 55°. This increase is attributed to the rise of the grand average of hydropathy

(GRAVY) value (-2.5) obtained for the CEEEEE sequence from the GRAVY Calculator, compared to the hydropathy index (HI) of lysine residues (-3.9) calculated by the ProtScale software. This difference explains the variation of water contact angle data after the coupling reaction and, consequently, the reduction of the hydrophilicity of the surface.

Figure 29 shows representative PM-IRRAS spectra obtained for PLL-mal(26%) deposition on gold surface (black line) and for the coupling reaction of CEEEEE (grey line) to immobilized PLL-mal(26%) on the surface.

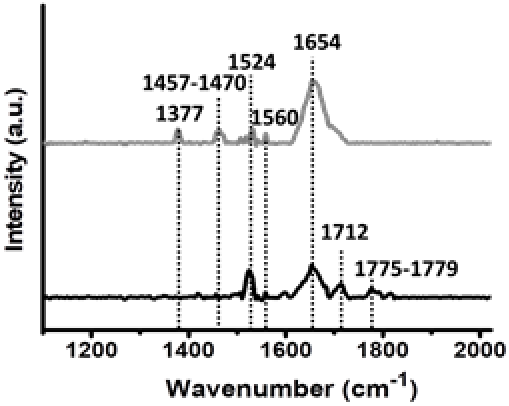

Figure 29. PM-IRRAS spectra of PLL–mal(26%) deposited on a gold chip (black line, bottom), and PLL-mal(26%)-CEEEEE (grey line, top) after the coupling reaction with CEEEEE.

The signals in the 1775-1779 cm^{-1} range are assigned to the symmetric stretch of maleimide carbonyl groups, and the peak at 1712 cm^{-1} is attributed to the in-phase stretching vibration of the two maleimide carbonyl moieties.[358] The large band at 1654 cm^{-1} is attributed to the carbonyl stretch of the amide I bonds within the PLL polymer.[358] This peak at 1654 cm^{-1} increased in intensity upon the immobilization of CEEEEE on PLL-mal(y%). In fact, the immobilized CEEEEE adds carboxylate groups to carbonyl moieties already available on the surface after PLL-mal(y%) deposition. The signals at 1524-1560 cm^{-1} are attributed to the amide II band (CN stretch and NH bend) and their attenuations can be due to the presence of CEEEEE, as described for similar functionalized PLL-mal(y%) polymers.[356] Bands in the 1457 – 1470 cm^{-1} range are attributed to δ (CH_2) scissors deformation, while the band at 1377 cm^{-1} results from the stretching of (C – N – C) groups. PLL-mal(y%)-CEEEEE polymers with different maleimide fractions (y%) showed features similar to those here discussed were observed (Fig. S6-S7). The analysis of the PM-IRRAS spectra indicates the successful formation of PLL-mal(y%)-CEEEEE on the gold surface.

Preliminary evaluations for the coupling efficiency of CEEEEE to the PLL-mal(y%) and for the antifouling property of the new PLL-based systems carrying different y% of maleimide moieties were performed by QCM-D (Table 5), using BSA (1.0 mg mL^{-1} and 50.0 mg mL^{-1}) as standard single-protein solutions. BSA solution at higher concentration (50.0 mg mL^{-1}) has been utilized as the average concentration of blood plasma proteins.[359]

Table 5. Surface coverage (ng cm^{-2}) of PLL-mal(y%), CEEEEE and BSA solutions on PLL-mal(y%)-CEEEEE estimated by QCM-D. Moles of peptide per moles of maleimide units were also calculated to evaluate the coupling efficiency of CEEEEE to the PLL-mal(y%).

Areal mass (ng cm^{-2})					
(y%)	**PLL-mal(y%)**	**CEEEEE**	**mol CEEEEE/ mal(y%)**	**[BSA] 1.0 mg mL^{-1}**	**[BSA] 50.0 mg mL^{-1}**
26	291	470	1.9	32	41
22	363	648	2.3	20	45
13	406	446	2.0	29	49

QCM-D was used to assess film formation, peptide coupling, and protein adsorption. All the analyses of QCM-D measurements (Δf and ΔD) revealed that the ratio $\Delta D/(\Delta f_N/N)$ is lower than 0.4×10^{-6} Hz^{-1} and, therefore, we considered the Sauerbrey equation valid to estimate the adsorbed mass of PLL-mal(y%), peptide and proteins, assuming the film as rigid.[360]

Upon the use of QCM-D to assess the coupling efficiency of CEEEEE and PLL-mal(y%), it was observed (Table 5) that the adsorbed masses of peptide were approx. twice those expected to get saturation of the maleimide units. These differences can possibly be attributed to stronger hydration of CEEEEE compared to PLL, which could arise from the tight adsorption of PLL to the substrate while the peptide chains stand out from the surface. This would mean that in particular the areal masses of the peptide are overestimated, and thus also the peptide/mal ratios. Yet, a minor contribution from the insertion of the peptide directly onto the gold surface cannot be excluded.

When assuming that each peptide has 5 negative charges, charge neutrality is reached when a 17% mal-functionalized PLL (1 neutral mal-functionalized unit per 5 positively charged not functionalized lysine units) is fully reacted with the peptide. From the results presented above, it can be estimated that the resulting layers are ranging, for increasing mal fractions, from close-to charge neutral to negatively charged. Over-charging occurs also normally for polyelectrolytes and it depends on the conditions during coupling reaction. In fact, background salt screens the surface charges making it continuously accessible for the peptide, even when the surface is already overall negatively charged. Moreover, it was observed that PLL-mal(26%)-CEEEEE provides better antifouling performances than the other PLL-mal(y%)-CEEEEE polymers, with the lowest surface coverage value (41 ng cm^{-2}) for 50.0 mg mL^{-1} of BSA. I believe that the highest degree of mal units provides more binding sites available for the coupling reaction with CEEEEE, thus leading to more negative charges on the surface and improving the resistance to the adsorption of negatively charged proteins at physiological pH.[361]

SPRI and QCM-D were also used for the comparison of coupling efficiency analysis for the reaction of CEEEEE to the PLL-mal(y%) layer in real time. Figure 30 shows representative SPRI and QCM-D curves for the adsorption of PLL-mal(26%) (Fig.30 a, b) on gold substrate and the coupling reaction of CEEEEE to maleimide moieties of PLL-mal(26%) layer (Fig.30 c, d).

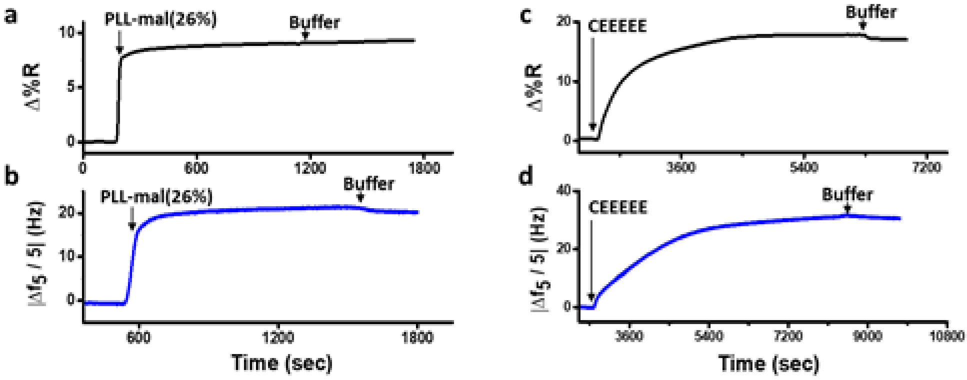

Figure 30. Representative SPRI (a, c) and QCM-D (b, d) adsorption curves of the immobilization of PLL-mal(26%) on gold (a,b), and of the subsequent coupling of CEEEEE to the maleimide units (c, d).

Both SPRI and QCM-D data confirmed that the adsorption of PLL-mal(26%) on gold proceeds with fast kinetics, reaching saturation within a few minutes, and providing a stable surface layer as witnessed by the absence of desorption upon switching to buffer (Fig.30 a, b). The coupling reaction between CEEEEE and the PLL-mal(26%) layer adsorbed on gold appeared to go slower (Fig.30 c, d), as both techniques indicate saturation taking at least 30 min. The areal masses of the absorbing layers and the molar ratio between CEEEEE and PLL-mal(26%) were also calculated considering the SPRI responses after the immobilization of the studied systems (see Table S4). In particular, relevant differences were calculated for the areal mass of the PLL-mal(26%) layer by SPRI (138 ng cm^{-2}, Fig.30 a and Table S4) and by QCM-D (291 ng cm^{-2}, Fig.30 b and Table 5), and also different values of the areal mass after the adsorption of CEEEEE were measured by SPRI (282 ng cm^{-2}, Fig.30 c and Table S4) and by QCM-D (470 ng cm^{-2}, Fig.11 d and Table 5). Similar results for the molar ratio between CEEEEE and PLL-mal(26%) were obtained by both techniques (2.4 by SPRI, Table S4, and 1.9 by QCM-D, Table 5).

For the mass density measurements, significant variations were observed between SPRI and QCM-D results, where the PLL-mal(26%) and CEEEEE layers are heavily hydrated in QCM-D, nearly twice as much if compared with the same SPRI data. Despite the hydration of PLL-mal(26%) and CEEEEE may be differently weighted in QCM-D experiments, due to the bound water molecules co-measured to PLL polymer and, especially, co-measured to the highly hydrophilic peptide, similar molar ratios of CEEEEE to PLL-mal(26) were obtained by SPRI and QCM-D, confirming the same coupling efficiency of the reaction obtained by two different techniques. Subsequently, the antifouling activities for PLL-mal(26%)-CEEEEE were investigated by both QCM-D and SPRI, using the same BSA solutions. Figure 31 shows representative SPRI (Fig.31 a) and QCM-D (Fig.31 b) responses measured during the adsorption of BSA (1.0 mg mL^{-1} and 50.0 mg mL^{-1}) on PLL-mal(26%)-CEEEEE.

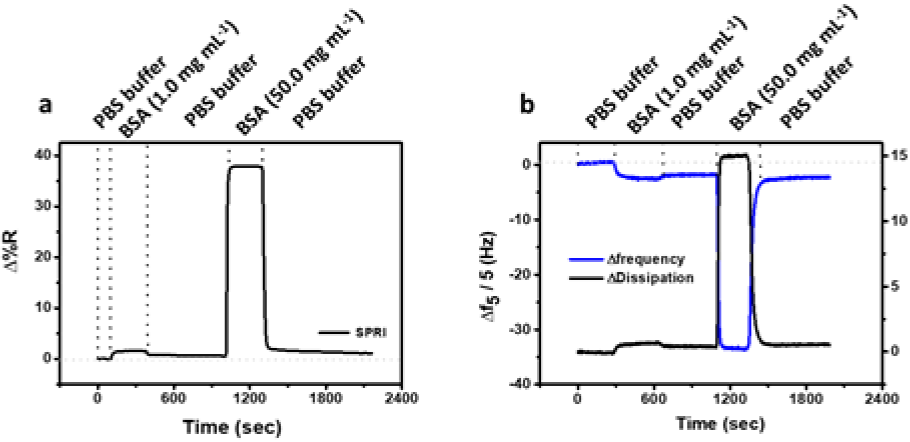

Figure 31. BSA adsorption on PLL-mal(26%)-CEEEEE measured by (a) SPRI and (b) QCM-D. Frequency (blue line) and energy dissipation (black line) shifts corresponding to BSA adsorption are observed in QCM-D measurement (b).

Surface coverage was similarly quantified by SPRI when a 1.0 mg mL^{-1} and 50.0 mg mL^{-1} solutions were put in contact with the PLL-mal(26%)-CEEEEE antifouling layer for 5 min, respectively (Table S4). In contrast, calculations based on QCM-D experiments produced a higher surface coverage (41 ng cm^{-2}) when 26% of maleimide units was considered (Table 5). It has been already reported that QCM-D data are significantly affected by the contribution (70-90%) of bound water molecules present in the structure of adsorbed molecules, in particular proteins, such as BSA.[107] On the basis of the experimental data, it is evident that water contributes to the QCM frequency change to a higher extent.

Only for the PLL-mal(26%)-CEEEEE layer, both QCM and SPR were performed, for the other mal fractions, only QCM-D was used (see Table 2). The comparison shows that the best antifouling properties were obtained for the highest degree of peptide functionalization.

Compared with the polymer systems of antifouling coatings in SPRI experiments, such as polysaccharide-based materials and zwitterionic compounds based materials where the protein adsorption levels were more than 6 ng cm^{-2} using lower concentrations of BSA, such as 0.1 mg mL^{-1} and 1.0 mg mL^{-1},[362-364] the functionalized PLL-mal(26%)-CEEEEE layer exhibits an excellent resistance to fouling from highly concentrated single-protein solutions.

A further non-fouling investigation was performed on silicon oxide surfaces covered with PLL-mal(26%)-CEEEEE, by QCM-D experiments (Fig. S8, Table S5). Similar antifouling performance was achieved when PLL-mal(26%)-CEEEEE layer was immobilized on SiO_2 (55 ng cm^{-2}) as compared to modified PLL on a gold surface (41 ng cm^{-2}), by confirming the antifouling character of the layer on both surfaces in BSA solutions.

In order to assess the antifouling activity of the PLL-mal(26%)-CEEEEE layer in real and complex biological samples, diluted human blood plasma samples (5%, 10% and 33% in PBS) were tested (Fig.32) and, thereby, the final adsorbed protein mass was calculated by SPRI and QCM-D (Table 6, Fig.33).

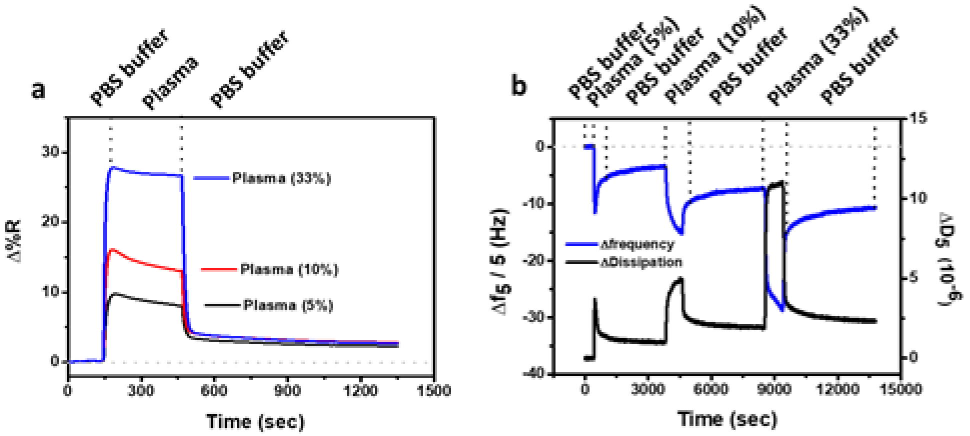

Figure 32. (a) SPRI and (b) QCM-D antifouling tests using diluted human plasma samples and PLL-mal(26%)-CEEEEE. Frequency (blue line) and energy dissipation (black line) shifts corresponding to the adsorption of protein from diluted human plasma samples are observed in QCM-D measurement (b).

Table 6. Surface coverage of protein (ng cm^{-2}) from diluted human plasma samples on PLL-mal(26%)-CEEEEE estimated by SPRI and QCM-D. Errors indicate the standard deviation of the SPRI data.

Human plasma in PBS	SPRI (ng cm^{-2})	QCM-D (ng cm^{-2})
5%	39 ± 7	62
10%	48 ± 6	130
33%	46 ± 1	190

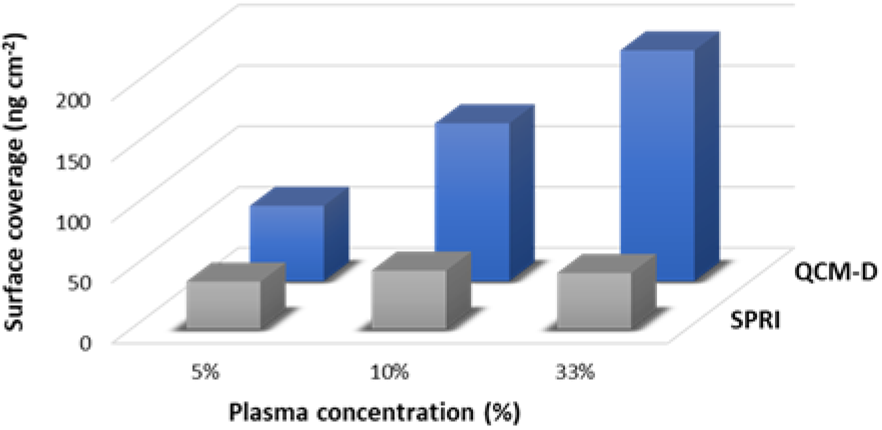

Figure 33. Surface coverage of protein (ng cm^{-2}) from diluted human plasma samples on PLL-mal(26%)-CEEEEE estimated by SPRI and QCM-D. Surface coverage values are reported in Table 6.

As reported in Table 6 and in Figure 33, it was revealed that the resistance to fouling from complex media does not reflect the surface resistance to single-protein BSA solutions. Human plasma comprises a mixture of plasma proteins, being lysozyme (MW about 14 kDa), albumin (MW about 66 kDa), immunoglobulins (MW about 150 kDa) and fibrinogen (MW about 340 kDa) the most abundant.[322,365] The hydration shell of bound water molecules, the concentration and the molecular size of the plasma proteins have a relevant effect on the adsorption phenomenon and, then, on the mass of adsorbed protein detected by QCM-D (Table 6). In general, small proteins, such as lysozyme, are able to penetrate the antifouling polymer and adsorb directly on the substrate. This process is called primary adsorption, or ternary adsorption whether the small proteins are within the layer. Both adsorption mechanisms strongly influence the QCM resonant frequency shifts, where the smallest proteins can be better detected than the largest ones.[107] The adsorption “on top” of the layer, termed secondary adsorption, is more likely to arise for large plasma protein, such as fibrinogen. Depending on the thickness of the antifouling polymer, the secondary adsorption process affects QCM-D results and the absolute amount of protein absorbed may be underestimated when this adsorption process on top of the layer occurred.[107] Here, however, the antifouling layers are very thin (few nm) and therefore adsorption is primarily on top of the layer, but assumed without a change in sensitivity.

The values of adsorbed mass, equal to 46 ng cm^{-2} using 33% human plasma detected by SPRI (Table 6), show a significant non-fouling activity of PLL-mal(26%)-CEEEEE layer in real human plasma samples, especially if compared to PEG/OEG-based materials and other hydrophilic antifouling materials where the protein adsorption levels in complex media were more than 60 ng cm^{-2} in SPR measurements.[366-369] Moreover, the antifouling test was carried out for PLL-mal(26%)-CEEEEE deposited on a silicon oxide surface, thus confirming the antifouling property in diluted human plasma samples comparable to the previous results obtained for the gold surface (Fig. S9, Table S9).

To assess the contribution to the antifouling properties of the coupling reaction of CEEEEE with PLL-mal(26%), the antifouling test was replicated using 5%, 10% and 33% diluted human plasma on PLL-mal(26%) surface (Table 7, Fig.34).

Table 7. Surface coverage of protein (ng cm^{-2}) from diluted human plasma samples on PLL-mal(26%) and PLL-mal(26%)-CEEEEE estimated by SPRI. Errors indicate the standard deviation of the data.

Human plasma in PBS	**SPRI (ng cm^{-2})**	
	PLL-mal(26%)	**PLL-mal(26%)-CEEEEE**
5%	38	39 ± 7
10%	48 ± 13	48 ± 6
33%	74 ± 3	46 ± 1

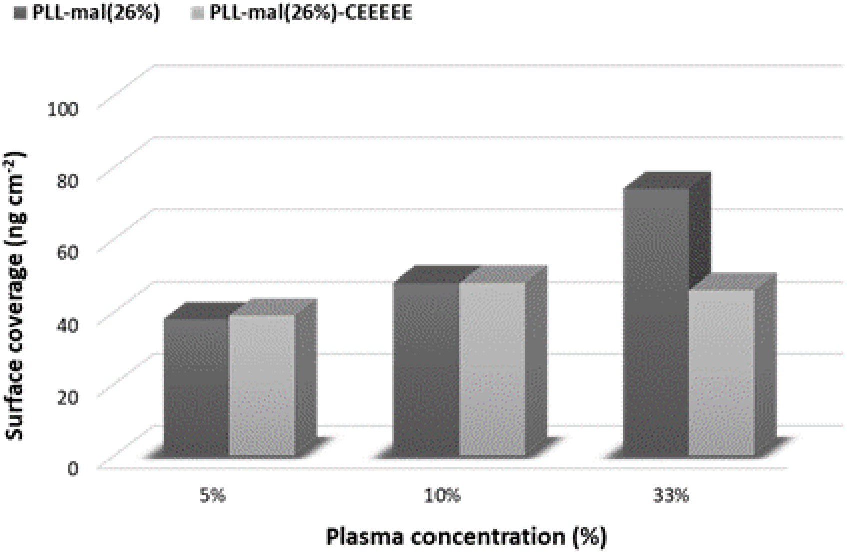

Figure 34. Surface coverage of protein (ng cm^{-2}) from diluted human plasma samples on PLL-mal(26%) and PLL-mal(26%)-CEEEEE sensors estimated by SPRI.

By comparing the previous results gained from PLL-mal(26%)-CEEEEE surface, the large amount of adsorbed protein (74 ± 3 ng cm^{-2}) on PLL-mal(26%) layer is attributed to electrostatic interactions between the positively charged surface and the oppositely charged protein residues. Hence, the increase of the nonspecific protein adsorption of PLL-mal(26%) confirmed that the CEEEEE plays a crucial role for the antifouling property of PLL-mal(26%)-CEEEEE layer.

After these data on the antifouling property, I optimized the functionalization strategy of PLL-mal(26%)-CEEEEE film, in terms of the running buffer and the yield of peptide synthesis, in order to reduce the total amount of plasma protein adsorbed on the surface. Then, the antifouling test was replicated with 10% diluted human plasma on PLL-mal(26%)-CEEEEE by recording an amount of plasma protein adsorbed on the surface equal to 22 ± 7 ng cm^{-2}. The standard deviation was calculated for thirteen independent experiments (Table 8, Fig.35).

Table 8. Surface coverage of protein (ng cm^{-2}) from diluted human plasma samples (10%) on PLL-mal(26%)-CEEEEE old synthesis and PLL-mal(26%)-CEEEEE new synthesis surfaces estimated by SPRI. Errors indicate the standard deviation of the data.

	SPRI (ng cm^{-2})
PLL-mal(26%)-CEEEEE old synthesis	48 ± 6
PLL-mal(26%)-CEEEEE new synthesis	22 ± 7

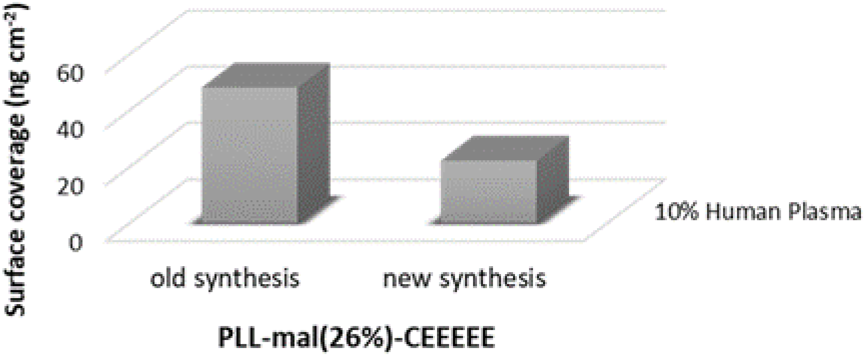

Figure 35. Surface coverage of protein (ng cm^{-2}) from diluted human plasma samples on PLL-mal(26%)-CEEEEE old synthesis and PLL-mal(26%)-CEEEEE new synthesis surfaces estimated by SPRI.

If compared to previous antifouling results, the significant reduction of plasma protein adsorption could be especially ascribed to high purity and yield of the new synthesis of commercial CEEEEE peptide used to optimize the functionalization strategy of the antifouling coating.

V. Results and Discussion – part III

V.3. Development of nanoparticle-enhanced SPRI assay for ctDNA mutations using PLL-mal(26%)-CEEEEE as antifouling layer

In the last part, I realized a novel nanoparticle-enhanced SPRI assay for ctDNA detection, carrying KRAS gene mutation, in human plasma samples using PLL-mal(y%)-CEEEEE layer as antifouling coating.

Scheme 3 shows the adopted nanoparticle-enhanced SPRI strategy for the ultrasensitive detection of non-amplified genomic DNA (gDNA) with single point mutations in KRAS gene exon 2, using the PLL-peptide antifouling layer.

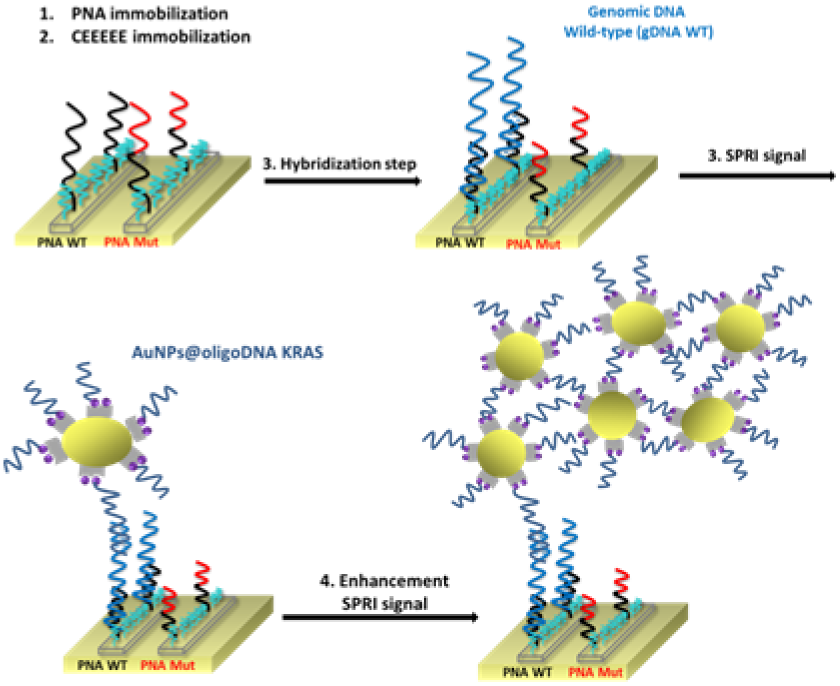

Scheme 3. Pictorial representation of nanoparticle-enhanced SPRI assay for the detection of ctDNA KRAS exon 2: Wild-Type and mutated target in human plasma samples by using the PLL-mal(26%)-CEEEEE antifouling layer. To simplify the representation only specific adsorbed ctDNA is shown. PNA WT and PNA Mut specifically recognize the wild-type and mutated genomic sequences, respectively.

Initially, after the activation of the gold chip by UV-ozone, 0.5 mg mL^{-1} of PLL-mal(26%) was deposited via electrostatic interactions on the gold sensor by flowing the polymer into the SPRI microfluidic device, in order to have a spatial control of the PLL-mal(26%) attachment to the surface. Therefore, 0.1 µM of thiol-PNA WT and thiol-PNA Mut (G12D) probes freshly deprotected by using the TCEP gel were attached to the maleimide units of the functionalized PLL-mal(26%) sensor through the thiol–maleimide Michael-type addition (Scheme 3, step 1). Subsequently, 1.0 mM of anionic peptide CEEEEE was anchored to the free maleimide moieties by the above-described thiol–maleimide reaction using the microfluidic system coupled to SPR sensor chip (Scheme 3, step 2).

Figure 36 shows representative SPR curves of PLL-mal(26%) deposition, PNA WT and PNA Mut (PNA G12D) probes immobilization and CEEEEE coupling reaction to the free maleimide moieties of PLL-mal(26%) previously absorbed on the gold substrate.

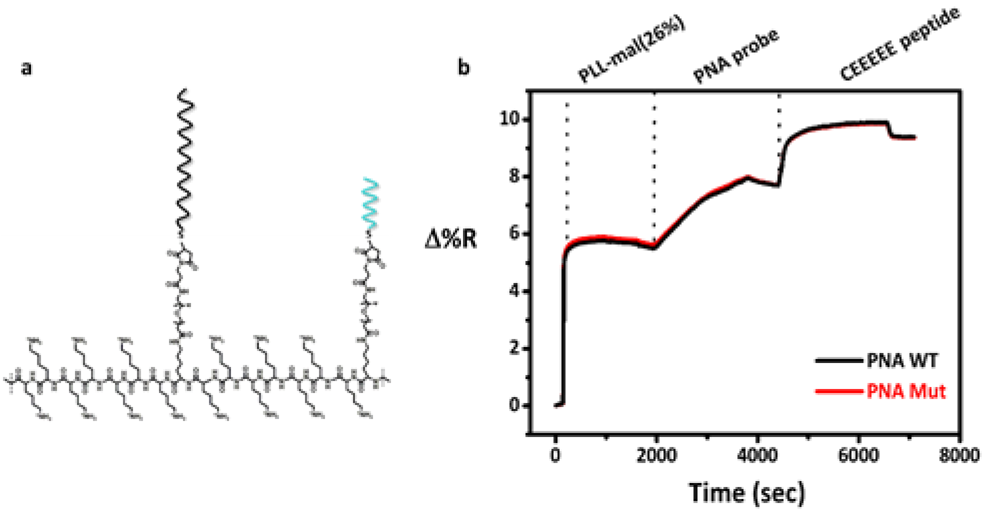

Figure 36. (a) Schematic representation of PLL-mal(26%)-PNA probes-CEEEEE layer on SPR gold sensor. (b) Representative SPRI curve, in percent reflectivity (Δ%R) over time, of PLL-mal(26%) deposition, PNA WT and PNA Mut (PNA G12D) probes immobilization and CEEEEE coupling reaction with PLL-mal(26%) previously absorbed on the gold substrate.

As reported in Figure 36 (b), homogeneous PLL-mal(26%) deposition, PNA probes immobilization and CEEEEE anchoring were obtained for both control and mismatch channels. Also, in this nanoparticle-enhanced SPRI assay, the optimal range of molecular probes density was determined between 2 and 3 Δ%R values by flowing PBS buffer after the PNA immobilization step (Fig.36 b).

Diluted human plasma samples (10% in PBS buffer) were spiked with genomic DNA sequences of healthy donors and cancer patients, respectively, at a final concentration of 5 pg µL^{-1}. Therefore, each ctDNA sample was centrifuged and fragmented following the above-mentioned protocols before the analysis (Section IV.3.2.). No other treatments were reserved to ctDNA samples for nanoparticle-enhanced SPRI assay detection. Typical experiments were carried out by detecting multiplex responses using an SPRI microfluidic device assembled by six parallel channels. An exact volume of ctDNA samples in human plasma (300 µL) directly flowed into the SPRI device to allow the direct interaction of each of the three specimens with PNA WT and PNA Mut, previously attached to PLL-mal polymer (Scheme 3, step 3). As described before for the development of nanoparticle-enhanced SPRI assay for gDNA KRAS gene mutations, the design of SPRI experiments included control channels, where the direct hybridization between ctDNA samples and corresponding PNA probes occurred and mismatch channels, where the binding between ctDNA samples and PNA probes was not to be expected (Fig. 37).

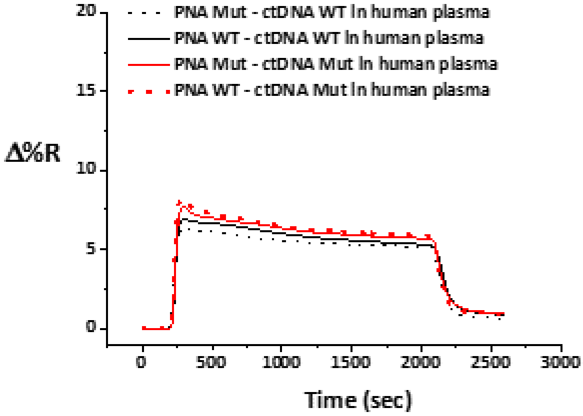

Figure 37. Typical SPRI curves, in percent reflectivity (Δ%R) over time, of gDNA hybridization in control channels (PNA WT/DNA WT black solid line, PNA Mut/DNA Mut red solid line) and mismatch channels (PNA Mut/DNA WT black dot line, PNA WT/DNA Mut red dot line) using 5 pg µL^{-1} of ctDNA fragments in diluted human plasma samples. PNA G12D and gDNA G12D were employed as PNA Mut and gDNA Mut, respectively.

The direct interaction of the above-mentioned 5 pg µL^{-1} ctDNA solutions in human plasma with PNA WT and PNA Mut probes generate SPRI signals quite different if compared with the previous results of the nanoparticle-enhanced SPRI assay (Fig.21 b, Fig.37). Precisely, the initial increase of Δ%R values could be attributed to the strong variation of the refractive index of plasma proteins into the sample solutions. However, by flowing PBS buffer after the hybridization step, the Δ%R values swiftly decrease when the plasma proteins are flushed away from the surface thanks to the antifouling property of PLL-mal(26%)-CEEEEE layer. In this way, the PLL-mal(26%) coupled with

PNA probes and CEEEEE would facilitate the hybridization with complementary ctDNA sequences and, at the same time, it would prevent the nonspecific protein adsorption from human plasma samples.

The ultrasensitive detection of the ctDNA target hybridization was obtained by using AuNPs conjugated with an oligonucleotide complementary to a small region of the target gDNA not involved in the hybridization step. Functionalized AuNPs were adsorbed on surfaces (0.1 nM in PBS, flow rate 15 µL min^{-1}, exact volume 900 µL), where the direct hybridization with the complementary gDNA sequence occurred (Scheme 3, step 4). By flowing the conjugated AuNPs into the microchannels so as to have a specific control of the detection target ctDNA through gold nanoparticles, a significant increase in SPRI signals was obtained (Scheme 3, step 5).

Figure 38 shows the experimental results for ultrasensitive detection of ctDNA hybridization for G12D KRAS gene mutation after the adsorption of conjugated AuNPs.

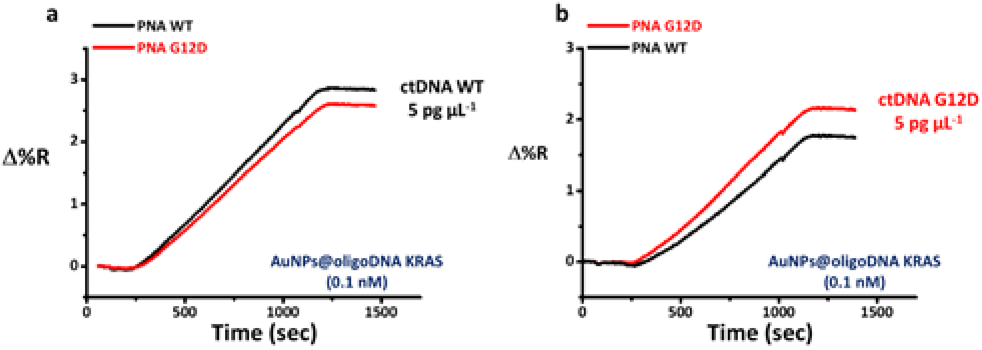

Figure 38. (a) Representative time-dependent SPRI curves obtained after the interaction of conjugated AuNPs on PNA WT/ctDNA WT control channel and PNA G12D/ctDNA WT mismatch channel. (b) Representative time-dependent SPRI curves obtained after the interaction of conjugated AuNPs on PNA G12D/ctDNA G12D control channel and PNA WT/ctDNA G12D mismatch channel. ctDNA WT and G12D sequences in diluted human plasma samples were previously adsorbed to PLL-mal(26%) functionalized with PNA WT (black curves) and PNA G12D (red curves) and CEEEEE peptide in parallel channels. 5 pg µL^{-1} solutions of ctDNAs in diluted human plasma and 0.1 nM of AuNPs-conjugated were used in ten independent experiments.

The detected SPRI responses were in accordance with those expected for ctDNA WT hybridization, by recording an optimal discrimination between target and non-target DNA sequences. Basically, ctDNA WT preferentially hybridizes with the complementary PNA WT probe, while the interaction of mismatch sequences is prevented (Fig.38 a). Moreover, after the interaction of functionalized AuNPs for the detection of ctDNA G12D in plasma, a significant discrimination between target and non-target DNA sequences for G12D mutation was recorded by using nanoparticle-enhanced SPRI assay with antifouling layer based on modified PLL-mal polymer (Fig.38 b).

Figure 39 shows the average results from 10 replicate experiments carried out by using ctDNAs from healthy donors and cancer patients with G12D KRAS gene mutation.

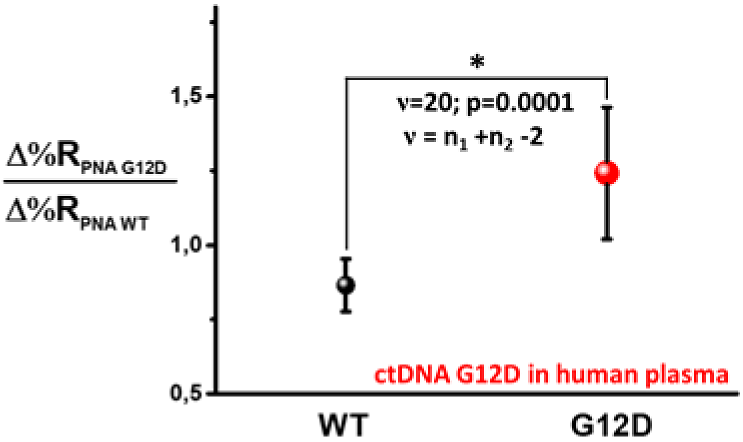

Figure 39. Mean $\Delta\%R_{PNA\ G12D}/\Delta\%R_{PNA\ WT}$ ratio values obtained from 10 replicated experiments aimed at detecting 5 pg μL^{-1} solutions of WT and G12D non-amplified genomic DNAs in human plasma samples. Ratios were obtained by considering Δ%R values after 1000 s of adsorption of conjugated AuNPs. The ratio considers SPRI responses (Δ%R) referred to the PNA G12D probe ($\Delta\%R_{PNA\ G12D}$) and the PNA WT probe ($\Delta\%R_{PNA\ WT}$), respectively when the same DNA target was detected. ctDNA WT (mean $\Delta\%R_{PNA\ G12D}/\Delta\%R_{PNA\ WT}$ = 0.87, confidence interval at the 95% level CI = 0.87 (0.09, replicate measurements n_1 = 9) and ctDNA G12D (mean $\Delta\%R_{PNA\ G12D}/\Delta\%R_{PNA\ WT}$ = 1.24, CI = 1.24 (0.22, replicate measurements n_2 = 13) generated significantly different $\Delta\%R_{PNA\ G12D}/\Delta\%R_{PNA\ WT}$ ratio (unpaired t-test, level 95%, two-tailed P value equals to 0.0001). Error bars represent the 95% confidence interval (CI) of the mean. The asterisk (*) indicate statistically different values.

The ratio between the SPRI responses (Δ%R) is referred to the PNA G12D probe ($\Delta\%R_{PNA\ G12D}$) and the PNA WT probe ($\Delta\%R_{PNA\ WT}$) when the same ctDNA target in human plasma was detected. ctDNA WT and ctDNA G12D generated $\Delta\%R_{PNA\ G12D}/\Delta\%R_{PNA\ WT}$ ratios extremely statistically different (unpaired t-test, level 95%, two-tailed P value equals to 0.0001). These data confirm the designed nanoparticle-enhanced SPRI assay for the detection of ctDNA G12D in real samples would be able to distinguish the KRAS single point mutation from genomic sequences of healthy donors, directly in biological fluids, at attomolar level with an excellent discrimination. Also, I investigated the antifouling property of the single components of PLL-mal(26%)–PNA–CEEEEE layers by exposing the antifouling film at 10% of human plasma reproducing the same conditions of ctDNA detection.

Initially, the role of maleimide moieties of PLL polymer was analysed through the antifouling test. Therefore without maleimide units, the antifouling properties of PLL(no mal) layer, PLL(no mal) layer with PNA probes (PLL(no mal)–PNA), and PLL(no mal) layer with PNA probes and CEEEE peptide (PLL(no mal)–PNA–CEEEEE) were studied by flowing 10% of human plasma for 30 minutes. Then, the protein fouling resistance in terms of surface coverage (ng cm^{-2}) was evaluated by flushing away the plasma protein with PBS buffer for 10 minutes (Table 9, Fig.40).

Table 9. Surface coverage of protein (ng cm^{-2}) from 10% human plasma samples on PLL(no mal) layer, PLL(no mal)–PNA layer and PLL(no mal)–PNA–CEEEEE layer. The standard deviation was calculated for three independent experiments of each layer. Errors indicate the standard deviation of the data.

Surface layer	SPRI (ng cm^{-2})
PLL(no mal)	535 ± 17
PLL(no mal)–PNA	558 ± 54
PLL(no mal)–PNA–CEEEEE	347 ± 45

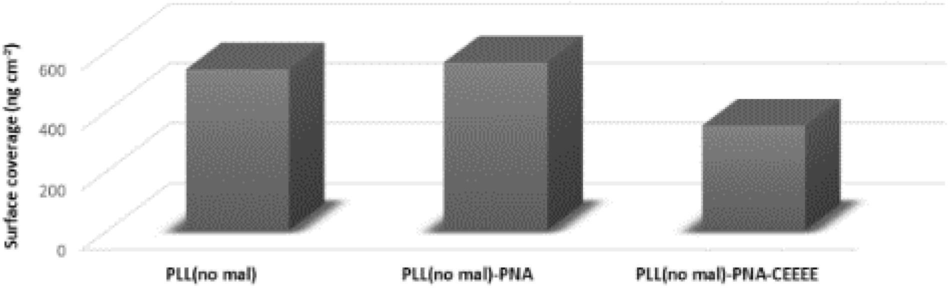

Figure 40. Surface coverage of protein (ng cm^{-2}) from 10% human plasma samples on PLL(no mal) layer, PLL(no mal)–PNA layer and PLL(no mal)–PNA–CEEEEE layer. Surface coverage values are reported in Table 9.

As reported in Table 9 and Figure 40, the surface layers show a non-fouling character by depositing a huge amount of plasma proteins onto the sensor chip. A slight decrease was observed when CEEEEE was attached to the PLL(no mal)–PNA layer, but no significant result in terms of the antifouling property of the coating was recorded.

Hence, the antifouling activity of the other components of the layer, which are PLL-mal(26%) and PLL-mal(26%)–PNA, was examined and compared with the entire layer PLL-mal(26%)–PNA–CEEEEE by flowing 10% of human plasma for 30 minutes. Then, the protein fouling resistance in terms of surface coverage (ng cm^{-2}) was evaluated by flushing away the plasma protein with PBS buffer for 10 minutes (Table 10, Fig.41).

Table 10. Surface coverage of protein (ng cm^{-2}) from 10% human plasma samples on PLL-mal(26%) layer, PLL-mal(26%)–PNA layer and PLL-mal(26%)–PNA–CEEEEE layer. The standard deviation was calculated for three independent experiments of the first two layers, and nine replicates for PLL-mal(26%)–PNA–CEEEEE layer. Errors indicate the standard deviation of the data.

Surface layer	SPRI (ng cm^{-2})
PLL-mal(26%)	364 ± 13
PLL-mal(26%)–PNA	381 ± 31
PLL-mal(26%)–PNA–CEEEEE	46 ± 34

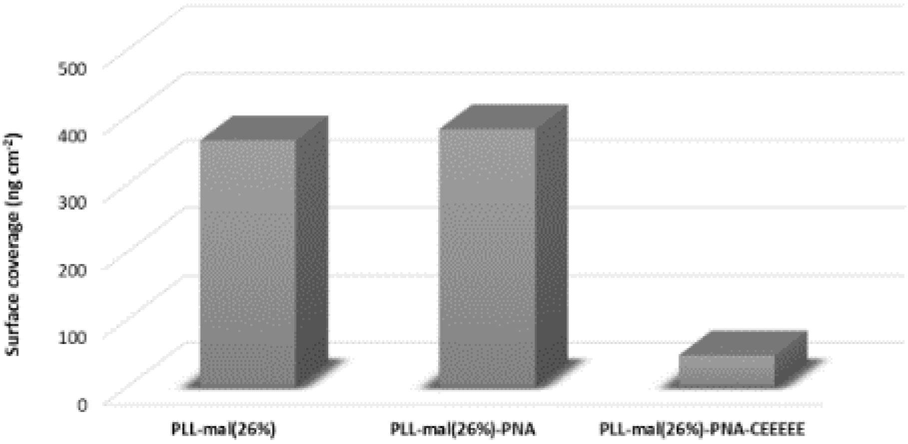

Figure 41. Surface coverage of protein (ng cm^{-2}) from 10% human plasma samples on PLL-mal(26%) layer, PLL-mal(26%)–PNA layer and PLL-mal(26%)–PNA–CEEEEE layer. Surface coverage values are reported in Table 10.

By comparing the experimental data obtained for PLL-mal(26%), PLL-mal(26%)–PNA and PLL-mal(26%)–PNA–CEEEEE films, the remarkable reduction of the surface coverage on PLL-mal(26%)–PNA–CEEEEE layer, after the exposure of the plasma proteins, indicates that all the components of the coating, that is PLL polymer, maleimide units and CEEEE peptide, cooperate for the antifouling property. Precisely, after the surface functionalization with PLL(no mal) or PLL-mal(26%), the modified-PLL sensors are positively charged and the plasma proteins, not neutral at physiological pH, could adsorb onto the substrate via electrostatic interactions so as to raise the surface coverage (Fig.40 and Fig.41, first column).

The functionalization of PLL polymers with PNA probes shows a small increase of the surface coverage both in PLL(no mal) and in PLL-mal(26%) layers (Fig.40 and Fig.41, second column). In this instance, the neutral backbone of PNA sequences would confer a hydrophobic character to the surfaces, which does not prevent the nonspecific protein adsorption from plasma medium.

Finally, after the functionalization of both PLL(no mal)–PNA and PLL-mal(26%)–PNA surfaces with the anionic peptide, a considerable reduction of the surface coverage after the plasma protein exposure was obtained (Fig.40 and Fig.41, third column). Especially, an excellent decrease of nonspecific adsorption of plasma proteins was recorded when the PLL polymer was previously modified with maleimide moieties. In this case, the coupling reaction of CEEEEE with maleimide units would guarantee the rise of peptide molecules attached to the sensor, in order to improve the antifouling character of the layer.

I also studied the direct functionalization of PNA probes and CEEEEE on SPR sensors through the well-known reaction between gold bare and thiol groups of the probes and the peptide. Therefore, the antifouling activity of PNA–CEEEEE film was examined and compared with PLL(no mal)–PNA–CEEEEE and PLL-mal(26%)–PNA–CEEEEE layers, by flowing 10% of human plasma for 30 minutes, in order to comprehend the role of PLL polymer in the antifouling property. Then, the protein fouling resistance in terms of surface coverage (ng cm^{-2}) was evaluated by flushing away the plasma protein with PBS buffer for 10 minutes (Table 11, Fig.42).

Table 11. Surface coverage of protein (ng cm^{-2}) from 10% human plasma samples on PNA–CEEEEE, PLL(no mal)–PNA–CEEEEE and PLL-mal(26%)–PNA–CEEEEE layer. The standard deviation was calculated for three independent experiments of the first two layers, and nine replicates for PLL-mal(26%)–PNA–CEEEEE layer. Errors indicate the standard deviation of the data.

Surface layer	**SPRI (ng cm^{-2})**
PNA–CEEEEE	300 ± 3
PLL(no mal)–PNA–CEEEEE	347 ± 45
PLL-mal(26%)–PNA–CEEEEE	46 ± 34

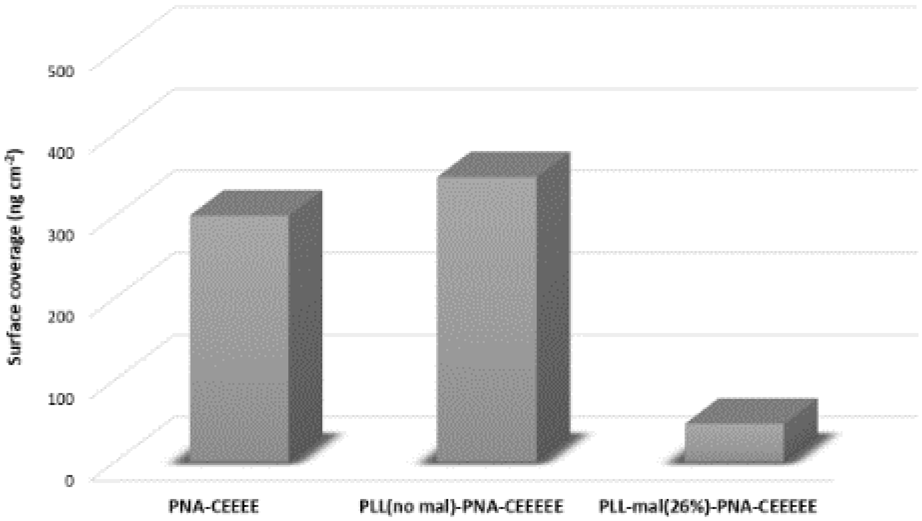

Figure 42. Surface coverage of protein (ng cm^{-2}) from 10% human plasma samples on PNA–CEEEEE, PLL(no mal)–PNA–CEEEEE and PLL-mal(26%)–PNA–CEEEEE layer. Surface coverage values are reported in Table 11.

As reported in Table 11 and Figure 42, the direct functionalization with PNA–CEEEEE did not provide any improvement on the antifouling property, by confirming that PLL polymer plays a crucial role in the nonspecific protein adsorption only when the polymer is previously modified with maleimide units and functionalized with the anionic peptide chains. In fact, the comparison with the data obtained for the other layers highlights that the balanced mixture of positive charges, from PLL-mal(26%) polymer, and the negative charges, from CEEEEE peptide, plays a synergic role to minimize the fouling effect from plasma proteins.

Figure 43 shows the SPRI kinetic curves of plasma proteins obtained for each surface layers.

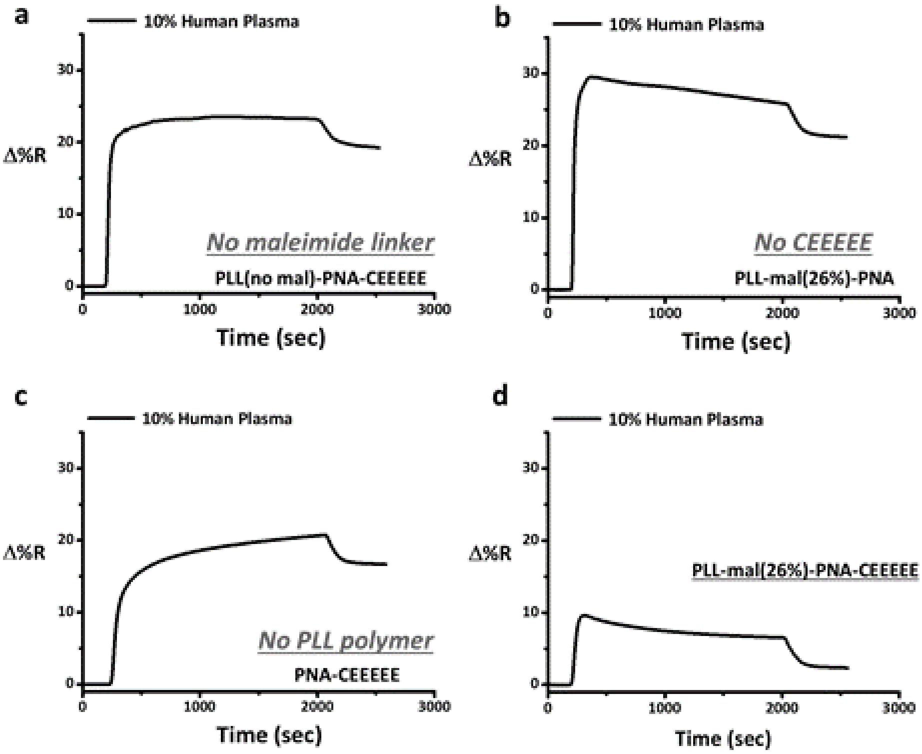

Figure 43. SPRI kinetic curves of plasma proteins interaction with (a) PLL(no mal)–PNA–CEEEEE layer, (b) PLL-mal(26%)–PNA layer, (c) PNA–CEEEEE layer and (d) PLL-mal(26%)–PNA–CEEEEE layer. The antifouling tests were replicated in three independent experiments for the layer (a), (b), (c) and in nine independent experiments for the layer (d).

Specifically, the kinetic curves highlight the different interaction mechanisms between the plasma proteins and the surface coatings: the experimental curves of PLL(no mal)–PNA–CEEEEE layer and PLL-mal(26%)–PNA layer exhibit a rapid adsorption of plasma proteins reaching the plateau of the curves within few minutes (Fig.43 a, b). Differently, the kinetic curve of PNA–CEEEEE layer presents a slow adsorption mechanism of plasma proteins, which does not completely get the saturation of the surface after the exposure to the biological medium (Fig.43 c). Then, the experimental curve of PLL-mal(26%)–PNA–CEEEEE layer displays the initial interaction upon the contact with the plasma proteins, but the SPRI kinetic curve goes rapidly down when the proteins are flushed away by PBS buffer, by confirming the antifouling activity of the film (Fig.43 d).

Chapter VI

Conclusions

VI. Conclusions

The work described in this PhD Thesis shows the potential benefits of the plasmonic platforms in the clinical and biomedical field. The appropriate knowledge in surface chemistry and biochemistry combined with the recent advances in biosensor technologies allowed the development of an efficient analytical device as a novel solution for early cancer diagnosis by liquid biopsy.

The key-points here proposed involved the design of biosensing strategy for cancer diagnosis, employing the well-known SPR biosensor, by offering a rapid, simple and label-free detection of tumor-derivated materials circulating in biological fluids.

Besides, the in-depth optimization and the evaluation of sensor surface biofunctionalization enabled an overall enhancement of the bioanalytical performances, leading to direct and reliable discrimination of ctDNA, with specific single-point mutations in KRAS gene exon 2, with good reproducibility in real clinical samples.

The general conclusions of this PhD Thesis are the following:

- The new design of SPRI biosensor assay for the ultrasensitive detection of single point mutations in non-amplified genomic DNA KRAS for early cancer diagnosis, using nanoparticle-enhanced SPRI approach, has been realized. Promising preliminary data for gDNA G12D, G12V, G13D detection have shown an acceptable discrimination between target and not-target DNA sequences. Moreover, the plasmonic platform has exhibited good results for the ultrasensitive detection of attomolar gDNA WT concentration, using aged AuNPs@oligoDNAKRAS.

- Mixed-charge polymer based on peptide-PLL polymers, which enables rapid, direct, effective functionalization of non-fouling layers for biosensing applications has been developed as blocking agents in this Thesis. While IR measurements confirmed successful coupling to the maleimide units, peptide-maleimide molar ratios have been assessed for the evaluation of the coupling efficiency. All molar ratios have been larger than 1:1 for all the y% values of maleimide units, which is in part attributed to differences in hydration between the peptide and the PLL polymer. Functionalized PLL-mal(26%)-CEEEEE surface revealed significant low-fouling properties in both BSA and human plasma samples through SPRI technique, with 46 ng cm^{-2} as the value of adsorbed protein when the highest percentage of human plasma samples has been utilized. Differently, the total nonspecific protein adsorption by QCM-D experiments was greater than 46 ng cm^{-2} in human plasma, confirming that these measurements are influenced by many factors, such as the hydration shell of bound water molecules co-measured with the plasma protein, the mechanism of protein adsorption and the molecular size of the plasma proteins. In contrast with many antifouling polymers, the PLL-mal(26%)-CEEEEE film demonstrated an excellent antifouling property using the highest concentration (50.0 mg mL^{-1}) of the single-protein solution. Additionally, after the optimization of the anionic peptide synthesis, the antifouling property has been improved in diluted human plasma (10%) on PLL-mal(26%)-CEEEEE with an amount of plasma protein adsorbed on the surface equal to 22 ± 7 ng cm^{-2}.

- The plasmonic biosensor has been finally applied for the development of a new early diagnostic technology for colorectal cancer. In this study, I designed and optimized a rapid and label-free methodology for the detection of circulating tumour DNA, carrying KRAS gene mutation, in human plasma samples using PLL-mal(26%)-CEEEEE layer as antifouling coating. After the interaction of functionalized AuNPs@oligoDNAKRAS for the detection of ctDNA G12D in plasma, a significant discrimination between target and non-target DNA sequences for G12D mutation has been recorded. I also investigated the contribution of the single components of PLL-mal(26%)-PNA-CEEEEE layer in the antifouling activity, by confirming that only the balanced mixture of positive charges, from PLL-mal(26%) polymer, and the negative charges, from CEEEEE peptide, plays a synergic role to minimize the fouling effect from plasma proteins.

Future perspectives may be focused towards performing the analytical methodology here studied in innovative biosensor platforms for rapid and multiplexed detection of ctDNA in real clinical samples for many cancer mutations.

This doctoral work has involved close collaborations with University of Parma, University of Twente, MESA+ Institute for Nanotechnology, and Italian National Cancer Institute Regina Elena in Rome.

This PhD Thesis would like to make a significant contribution to the progress of nanomedicine in clinical diagnostics to open the door to global health access in the near future.

Chapter VII

Bibliography

VII. Bibliography

1. World, Health, Organization, Global Health Observatory data repository (WHO), apps.who.int/gho/data/node.main.CODWORLD?lang=enaccessed 31.10.2013, **2011**, p. Number of deaths (World) by cause.
2. J. Ferlay, I. Soerjomataram, R. Dikshit, S. Eser, C. Mathers, M. Rebelo, D. M. Parkin, D. Forman, F. Bray, *Int J Cancer* **2015**, *136*, E359-E386.
3. B. Winograd, M. Peckham, H. M. Pinedo, *Human Tumour Xenografts in Anticancer Drug Development*, 1 ed., Springer-Verlag Berlin Heidelberg, **1988**.
4. M. Thompson, S. Sheikh, C. Blaszykowski, A. Romaschin, in *Detection Challenges in Clinical Diagnostics*, The Royal Society of Chemistry, **2013**, pp. 1-34.
5. E. Luong-Van, I. Rodriguez, H. Y. Low, N. Elmouelhi, B. Lowenhaupt, S. Natarajan, C. T. Lim, R. Prajapati, M. Vyakarnam, K. Cooper, *J Mater Res* **2013**, *28*, 165-174.
6. C. Blaszykowski, S. Sheikh, M. Thompson, *Trends Biotechnol* **2014**, *32*, 61-62.
7. A. R. Thierry, F. Mouliere, S. El Messaoudi, C. Mollevi, E. Lopez-Crapez, F. Rolet, B. Gillet, C. Gongora, P. Dechelotte, B. Robert, M. Del Rio, P. J. Lamy, F. Bibeau, M. Nouaille, V. Loriot, A. S. Jarrousse, F. Molina, M. Mathonnet, D. Pezet, M. Ychou, *Nat Med* **2014**, *20*, 430-435.
8. D. C. Garcia-Olmo, C. Dominguez, M. Garcia-Arranz, P. Anker, M. Stroun, J. M. Garcia-Verdugo, D. Garcia-Olmo, *Cancer Res* **2010**, *70*, 560-567.
9. H. Schwarzenbach, D. S. B. Hoon, K. Pantel, *Nat Rev Cancer* **2011**, *11*, 426-437.
10. G. Spoto, R. Corradini, *Detection of non-amplified genomic DNA, Springer* **2012**.
11. E. M. Southern, *Methods Mol Biol* **2001**, *170*, 1-15.
12. D. A. Hall, J. Ptacek, M. Snyder, *Mech Ageing Dev* **2007**, *128*, 161-167.
13. M. J. Heller, *Annu Rev Biomed Eng* **2002**, *4*, 129-153.
14. N. Leveque, F. Renois, L. Andreoletti, *Clin Microbiol Infect* **2013**, *19*, 10-14.
15. G. Wang, R. Han, X. Su, Y. Li, G. Xu, X. Luo, *Biosens Bioelectron* **2017**, *92*, 396-401.
16. V. Neychev, S. M. Steinberg, C. Cottle-Delisle, R. Merkel, N. Nilubol, J. Yao, P. Meltzer, K. Pacak, S. Marx, E. Kebebew, *BMJ Open* **2015**, *5*, e008248.
17. H. J. Burstein, A. D. Elias, H. S. Rugo, M. A. Cobleigh, A. C. Wolff, P. D. Eisenberg, M. Lehman, B. J. Adams, C. L. Bello, S. E. DePrimo, C. M. Baum, K. D. Miller, *J Clin Oncol* **2008**, *26*, 1810-1816.
18. P. A. Muller, K. H. Vousden, *Cancer Cell* **2014**, *25*, 304-317.
19. C. H. Yun, K. E. Mengwasser, A. V. Toms, M. S. Woo, H. Greulich, K. K. Wong, M. Meyerson, M. J. Eck, *Proc Natl Acad Sci U S A* **2008**, *105*, 2070-2075.
20. A. F. Gazdar, *Oncogene* **2009**, *28 Suppl 1*, S24-31.

21. E. Crowley, F. Di Nicolantonio, F. Loupakis, A. Bardelli, *Nat Rev Clin Oncol* **2013**, *10*, 472-484.
22. A. Diamantis, E. Magiorkinis, H. Koutselini, *Folia Histochem Cytobiol* **2009**, *47*, 191-197.
23. M. Gerlinger, A. J. Rowan, S. Horswell, M. Math, J. Larkin, D. Endesfelder, E. Gronroos, P. Martinez, N. Matthews, A. Stewart, P. Tarpey, I. Varela, B. Phillimore, S. Begum, N. Q. McDonald, A. Butler, D. Jones, K. Raine, C. Latimer, C. R. Santos, M. Nohadani, A. C. Eklund, B. Spencer-Dene, G. Clark, L. Pickering, G. Stamp, M. Gore, Z. Szallasi, J. Downward, P. A. Futreal, C. Swanton, *N Engl J Med* **2012**, *366*, 883-892.
24. D. R. Thevenot, K. Toth, R. A. Durst, G. S. Wilson, *Biosens Bioelectron* **2001**, *16*, 121-131.
25. F. J. Mulaa, P. M. Krämer, in *Handbook of Food Safety Engineering, Vol. 2* (Ed.: D. W. Sun), Wiley Blackwill, **2011**, pp. 313-352.
26. C. S. Huertas, L. M. Lechuga, *EMJ Oncol* **2017**, *5*, 54-61.
27. U. Jönsson, in *Biosensors 92 Proceedings: The Second World Congress on Biosensors* Elsevier Science, **1992**, p. 572.
28. J. Y. Yoon, in *Introduction to Biosensors*, Springer-Verlag New York, **2013**, pp. XIII, 262.
29. S. Sagadevan, M. Periasamy, *Rev Adv Mater Sci* **2014**, *36*, 62-69.
30. C. H. Ahn, J. W. Choi, G. Beaucage, J. H. Nevin, J. B. Lee, A. Puntambekar, J. Y. Lee, *P Ieee* **2004**, *92*, 154-173.
31. S. Kumar, S. Kumar, M. A. Ali, P. Anand, V. V. Agrawal, R. John, S. Maji, B. D. Malhotra, *Biotechnol J* **2013**, *8*, 1267-1279.
32. W. K. Kwong, Hong Kong University of Science and Technology **2000**.
33. K. Rogers, A. Mulchandani, *Affinity Biosensors - Techniques and Protocols*, Humana Press, **1998**.
34. N. J. Ronkainen, H. B. Halsall, W. R. Heineman, *Chem Soc Rev* **2010**, *39*, 1747-1763.
35. X. Zhang, H. Ju, J. Wang, *Electrochemical Sensors, Biosensors and their Biomedical Applications 1st Edition*, Academic Press, **2008**.
36. J. Tamayo, P. M. Kosaka, J. J. Ruz, A. San Paulo, M. Calleja, *Chem Soc Rev* **2013**, *42*, 1287-1311.
37. G. N. Ferreira, A. C. da-Silva, B. Tome, *Trends Biotechnol* **2009**, *27*, 689-697.
38. L. G. Carrascosa, M. Moreno, M. Alvarez, L. M. Lechuga, *Trac-Trend Anal Chem* **2006**, *25*, 196-206.
39. J. L. Arlett, E. B. Myers, M. L. Roukes, *Nat Nanotechnol* **2011**, *6*, 203-215.
40. M. Calleja, P. M. Kosaka, A. San Paulo, J. Tamayo, *Nanoscale* **2012**, *4*, 4925-4938.
41. F. Ligler, C. Taitt, *Optical Biosensors, 2nd Edition: Today and Tomorrow*, Elsevier Science, **2008**.
42. R. Narayanaswamy, O. S. Wolfbeis, *Optical Sensors - Industrial Environmental and Diagnostic Applications, Vol. 1*, Springer-Verlag Berlin Heidelberg, **2004**.

43. H. N. Daghestani, B. W. Day, *Sensors (Basel)* **2010**, *10*, 9630-9646.
44. V. Passaro, F. Dell'Olio, B. Casamassima, F. De Leonardis, *Sensors* **2007**, *7*, 508.
45. R. D'Agata, G. Spoto, *Anal Bioanal Chem* **2013**, *405*, 573-584.
46. A. G. Brolo, *Nat Photonics* **2012**, *6*, 709-713.
47. G. Spoto, M. Minunni, *J Phys Chem Lett* **2012**, *3*, 2682-2691.
48. R. Wilson, *Chemical Society Reviews* **2008**, *37*, 2028-2045.
49. P. L. Truong, C. Cao, S. Park, M. Kim, S. J. Sim, *Lab Chip* **2011**, *11*, 2591-2597.
50. R. Viswambari Devi, M. Doble, R. S. Verma, *Biosens Bioelectron* **2015**, *68*, 688-698.
51. W. Ma, H. Kuang, L. Xu, L. Ding, C. Xu, L. Wang, N. A. Kotov, *Nat Commun* **2013**, *4*, 2689.
52. R. D'Agata, G. Breveglieri, L. M. Zanoli, M. Borgatti, G. Spoto, R. Gambari, *Anal Chem* **2011**, *83*, 8711-8717.
53. J. Das, I. Ivanov, L. Montermini, J. Rak, E. H. Sargent, S. O. Kelley, *Nat Chem* **2015**, *7*, 569-575.
54. L. G. Carrascosa, A. A. Sina, R. Palanisamy, B. Sepulveda, M. A. Otte, S. Rauf, M. J. Shiddiky, M. Trau, *Chem Commun (Camb)* **2014**, *50*, 3585-3588.
55. A. H. Nguyen, S. J. Sim, *Biosens Bioelectron* **2015**, *67*, 443-449.
56. F. Wei, C. C. Lin, A. Joon, Z. Feng, G. Troche, M. E. Lira, D. Chia, M. Mao, C. L. Ho, W. C. Su, D. T. Wong, *Am J Respir Crit Care Med* **2014**, *190*, 1117-1126.
57. H. X. Bei, R. Y. Li, Z. J. Li, J. K. Liu, Z. G. Gu, G. L. Wang, *RSC Advances* **2015**, *5*, 54211-54219.
58. M. Born, E. Wolf, *Principles of Optics Electromagnetic Theory of Propagation, Interference and Diffraction of Light*, Oxford, GB: Pergamon Press, **1980**.
59. H. Raether, *Springer Trac Mod Ph* **1988**, *111*, 1-133.
60. E. Kretschmann, H. Raether, *Zeitschrift Fur Naturforschung Part A—Astrophysik Physik Und Physikalische Chemie A, Vol. 23*, **1968**.
61. R. L. Rich, D. G. Myszka, *Curr Opin Biotechnol* **2000**, *11*, 54-61.
62. J. G. Quinn, S. O'Neill, A. Doyle, C. McAtamney, D. Diamond, B. D. MacCraith, R. O'Kennedy, *Anal Biochem* **2000**, *281*, 135-143.
63. D. G. Myszka, R. L. Rich, *Pharm Sci Technolo Today* **2000**, *3*, 310-317.
64. A. G. Frutos, R. M. Corn, *Anal Chem* **1998**, *70*, 449A-455A.
65. U. Jonsson, L. Fagerstam, B. Ivarsson, B. Johnsson, R. Karlsson, K. Lundh, S. Lofas, B. Persson, H. Roos, I. Ronnberg, S. Sjolander, E. Stenberg, R. Stahlberg, C. Urbaniczky, H. Ostlin, M. Malmqvist, *Biotechniques* **1991**, *11*, 620-&.
66. W. J. Zhou, Y. L. Chen, R. M. Corn, *Anal Chem* **2011**, *83*, 3897-3902.
67. T. H. Seefeld, W. J. Zhou, R. M. Corn, *Langmuir* **2011**, *27*, 6534-6540.
68. Y. Li, H. J. Lee, R. M. Corn, *Anal Chem* **2007**, *79*, 1082-1088.
69. M. Kim, S. O. Jung, K. Park, E. J. Jeong, H. A. Joung, T. H. Kim, D. W. Seol, B. H. Chung, *Biochem Bioph Res Co* **2005**, *338*, 1834-1838.
70. J. M. Brockman, B. P. Nelson, R. M. Corn, *Annu Rev Phys Chem* **2000**, *51*, 41-63.
71. R. D'Agata, G. Grasso, G. Iacono, G. Spoto, G. Vecchio, *Org Biomol Chem* **2006**, *4*, 610-612.

72. L. K. Wolf, Y. Gao, R. M. Georgiadis, *J Am Chem Soc* **2007**, *129*, 10503-10511.
73. H. J. Lee, A. W. Wark, R. M. Corn, *Langmuir* **2006**, *22*, 5241-5250.
74. H. H. Nguyen, J. Park, S. Kang, M. Kim, *Sensors (Basel)* **2015**, *15*, 10481-10510.
75. J. S. Shumaker-Parry, C. T. Campbell, *Anal Chem* **2004**, *76*, 907-917.
76. T. M. Squires, S. R. Quake, *Rev Mod Phys* **2005**, *77*, 977-1026.
77. R. D'Agata, G. Grasso, G. Spoto, *Open Spectrosc J* **2008**, *1*, 1-9.
78. D. Amarie, A. Alileche, B. Dragnea, J. A. Glazier, *Anal Chem* **2010**, *82*, 343-352.
79. E. Ouellet, C. Lausted, T. Lin, C. W. Yang, L. Hood, E. T. Lagally, *Lab Chip* **2010**, *10*, 581-588.
80. G. ZederLutz, E. Zuber, J. Witz, M. H. V. VanRegenmortel, *Anal Biochem* **1997**, *246*, 123-132.
81. P. Pattnaik, *Appl Biochem Biotech* **2005**, *126*, 79-92.
82. C. L. Baird, E. S. Courtenay, D. G. Myszka, *Anal Biochem* **2002**, *310*, 93-99.
83. G. J. Wegner, A. W. Wark, H. J. Lee, E. Codner, T. Saeki, S. P. Fang, R. M. Corn, *Anal Chem* **2004**, *76*, 5677-5684.
84. M. Geitmann, U. H. Danielson, *Anal Biochem* **2004**, *332*, 203-214.
85. T. Mannen, S. Yamaguchi, J. Honda, S. Sugimoto, A. Kitayama, T. Nagamune, *Anal Biochem* **2001**, *293*, 185-193.
86. M. Minunni, S. Tombelli, M. Mascini, *Anal Lett* **2007**, *40*, 1360-1370.
87. S. Scarano, M. Mascini, A. P. F. Turner, M. Minunni, *Biosens Bioelectron* **2010**, *25*, 957-966.
88. T. T. Goodrich, H. J. Lee, R. M. Corn, *J Am Chem Soc* **2004**, *126*, 4086-4087.
89. M. E. Stewart, C. R. Anderton, L. B. Thompson, J. Maria, S. K. Gray, J. A. Rogers, R. G. Nuzzo, *Chem Rev* **2008**, *108*, 494-521.
90. Z. Altintas, Y. Uludag, Y. Gurbuz, I. E. Tothill, *Talanta* **2011**, *86*, 377-383.
91. J. Ladd, A. D. Taylor, M. Piliarik, J. Homola, S. Y. Jiang, *Anal Bioanal Chem* **2009**, *393*, 1157-1163.
92. C. Liu, T. J. Lei, K. Ino, T. Matsue, N. J. Tao, C. Z. Li, *Chem Commun* **2012**, *48*, 10389-10391.
93. M. Ehrlich, *Oncogene* **2002**, *21*, 5400-5413.
94. Y. A. Li, A. W. Wark, H. J. Lee, R. M. Corn, *Anal Chem* **2006**, *78*, 3158-3164.
95. A. Shalabney, I. Abdulhalim, *Laser Photonics Rev* **2011**, *5*, 571-606.
96. K. A. Willets, R. P. Van Duyne, *Annu Rev Phys Chem* **2007**, *58*, 267-297.
97. C. R. Yonzon, E. Jeoung, S. Zou, G. C. Schatz, M. Mrksich, R. P. Van Duyne, *J Am Chem Soc* **2004**, *126*, 12669-12676.
98. Y. Sato, S. Ikegaki, K. Suzuki, H. Kawaguchi, *J Biomater Sci Polym Ed* **2003**, *14*, 803-820.
99. A. Bertucci, A. Manicardi, A. Candiani, S. Giannetti, A. Cucinotta, G. Spoto, M. Konstantaki, S. Pissadakis, S. Selleri, R. Corradini, *Biosens Bioelectron* **2015**, *63*, 248-254.
100. R. D'Agata, R. Corradini, C. Ferretti, L. Zanoli, M. Gatti, R. Marchelli, G. Spoto, *Biosens Bioelectron* **2010**, *25*, 2095-2100.

101. M. Egholm, O. Buchardt, L. Christensen, C. Behrens, S. M. Freier, D. A. Driver, R. H. Berg, S. K. Kim, B. Norden, P. E. Nielsen, *Nature* **1993**, *365*, 566-568.
102. P. E. Nielsen, *Curr Opin Biotechnol* **1999**, *10*, 71-75.
103. D. Johannsmann, *The Quartz Crystal Microbalance in Soft Matter Research - Fundamentals and Modeling*, 1 ed., Springer International Publishing, **2015**.
104. W. H. King, *Anal Chem* **1964**, *36*, 1735-1739.
105. S. K. Vashist, P. Vashist, *J Sensors* **2011**.
106. G. Sauerbrey, *Zeitschrift für Physik* **1959**, *155*, 206-222.
107. Y. Luan, D. Li, T. Wei, M. Wang, Z. Tang, J. L. Brash, H. Chen, *Anal Chem* **2017**, *89*, 4184-4191.
108. M. C. Dixon, *J Biomol Tech* **2008**, *19*, 151-158.
109. S. Sigalov, N. Shpigel, M. D. Levi, M. Feldberg, L. Daikhin, D. Aurbach, *Anal Chem* **2016**, *88*, 10151-10157.
110. M. D. Levi, L. Daikhin, D. Aurbach, V. Presser, *Electrochem Commun* **2016**, *67*, 16-21.
111. G. Duner, E. Thormann, A. Dedinaite, *J Colloid Interface Sci* **2013**, *408*, 229-234.
112. A. Dolatshahi-Pirouz, T. H. Jensen, K. Kolind, C. Bunger, M. Kassem, M. Foss, F. Besenbacher, *Colloids Surf B Biointerfaces* **2011**, *84*, 18-25.
113. N. Giamblanco, E. Martines, G. Marletta, *Langmuir* **2013**, *29*, 8335-8342.
114. M. Tagaya, T. Ikoma, N. Hanagata, T. Yoshioka, J. Tanaka, *Sci Technol Adv Mater* **2011**, *12*, 034411.
115. H. T. Phan, S. Bartelt-Hunt, K. B. Rodenhausen, M. Schubert, J. C. Bartz, *PLoS One* **2015**, *10*, e0141282.
116. S. Oh, M. Wilcox, J. P. Pearson, S. Borros, *Eur J Pharm Biopharm* **2015**, *96*, 477-483.
117. T. A. P. Rocha-Santos, *Trac-Trend Anal Chem* **2014**, *62*, 28-36.
118. E. T. Jansson, C. L. Trkulja, J. Olofsson, M. Millingen, J. Wikstrom, A. Jesorka, A. Karlsson, R. Karlsson, M. Davidson, O. Orwar, *Anal Chem* **2012**, *84*, 5582-5588.
119. K. F. Wang, R. Nagarajan, T. A. Camesano, *Colloids Surf B Biointerfaces* **2014**, *116*, 472-481.
120. S. Heydari, G. Haghayegh, *J Sensor Technology* **2014**, *4*, 81-100.
121. Y. Uludag, I. E. Tothill, *Anal Chem* **2012**, *84*, 5898-5904.
122. W. Y. Peh, E. Reimhult, H. F. Teh, J. S. Thomsen, X. Su, *Biophys J* **2007**, *92*, 4415-4423.
123. P. Ibarra, A. Fernandez, J. Campos, M. Urrejola, Z. S. Haidar, *J Biomed Nanotechnol* **2017**, *13*, 469-484.
124. P. Mandel, P. Metais, *C R Seances Soc Biol Fil* **1948**, *142*, 241-243.
125. V. Hofman, M. I. Ilie, E. Long, E. Selva, C. Bonnetaud, T. Molina, N. Venissac, J. Mouroux, P. Vielh, P. Hofman, *Int J Cancer* **2011**, *129*, 1651-1660.
126. C. Alix-Panabieres, K. Pantel, *Clin Chem* **2013**, *59*, 110-118.
127. C. Alix-Panabieres, K. Pantel, *Cancer Discov* **2016**, *6*, 479-491.
128. N. McGranahan, C. Swanton, *Cell* **2017**, *168*, 613-628.
129. C. Alix-Panabieres, K. Pantel, *Nat Rev Cancer* **2014**, *14*, 623-631.

130. D. D. Taylor, C. Gercel-Taylor, *Semin Immunopathol* **2011**, *33*, 441-454.
131. N. Kosaka, H. Iguchi, T. Ochiya, *Cancer Sci* **2010**, *101*, 2087-2092.
132. S. E. Deprimo, C. L. Bello, J. Smeraglia, C. M. Baum, D. Spinella, B. I. Rini, M. D. Michaelson, R. J. Motzer, *J Transl Med* **2007**, *5*, 32.
133. J. A. L. Coronell, P. Syed, K. Sergelen, I. Gyurjan, A. Weinhausel, *J Proteomics* **2012**, *76*, 102-115.
134. N. Bellassai, G. Spoto, *Anal Bioanal Chem* **2016**, *408*, 7255-7264.
135. D. W. Tsui, M. F. Berger, *Clin Cancer Res* **2016**, *22*, 790-792.
136. K. R. Chi, *Nature* **2016**, *532*, 269-271.
137. T. F. Imperiale, D. F. Ransohoff, S. H. Itzkowitz, T. R. Levin, P. Lavin, G. P. Lidgard, D. A. Ahlquist, B. M. Berger, *N Engl J Med* **2014**, *370*, 1287-1297.
138. RNCOS, **2016**, p. 90.
139. S. A. Leon, B. Shapiro, D. M. Sklaroff, M. J. Yaros, *Cancer Res* **1977**, *37*, 646-650.
140. Y. M. D. Lo, N. Corbetta, P. F. Chamberlain, V. Rai, I. L. Sargent, C. W. G. Redman, J. S. Wainscoat, *Lancet* **1997**, *350*, 485-487.
141. J. A. Hyett, G. Gardener, T. Stojilkovic-Mikic, K. M. Finning, P. G. Martin, C. H. Rodeck, L. S. Chitty, *Prenatal Diag* **2005**, *25*, 1111-1116.
142. H. Saito, A. Sekizawa, T. Morimoto, M. Suzuki, T. Yanaihara, *Lancet* **2000**, *356*, 1170-1170.
143. M. Stroun, P. Anker, P. Maurice, J. Lyautey, C. Lederrey, M. Beljanski, *Oncology* **1989**, *46*, 318-322.
144. A. R. Thierry, S. El Messaoudi, P. B. Gahan, P. Anker, M. Stroun, *Cancer Metastasis Rev* **2016**, *35*, 347-376.
145. S. J. Dawson, D. W. Y. Tsui, M. Murtaza, H. Biggs, O. M. Rueda, S. F. Chin, M. J. Dunning, D. Gale, T. Forshew, B. Mahler-Araujo, S. Rajan, S. Humphray, J. Becq, D. Halsall, M. Wallis, D. Bentley, C. Caldas, N. Rosenfeld, *New Engl J Med* **2013**, *368*, 1199-1209.
146. D. Sidransky, A. Voneschenbach, Y. C. Tsai, P. Jones, I. Summerhayes, F. Marshall, M. Paul, P. Green, S. R. Hamilton, P. Frost, B. Vogelstein, *Science* **1991**, *252*, 706-709.
147. E. M. Swisher, M. Wollan, S. M. Mahtani, J. B. Willner, R. Garcia, B. A. Goff, M. C. King, *Am J Obstet Gynecol* **2005**, *193*, 662-667.
148. H. Kimura, K. Kasahara, M. Kawaishi, H. Kunitoh, T. Tamura, B. Holloway, K. Nishio, *Clin Cancer Res* **2006**, *12*, 3915-3921.
149. G. Sozzi, K. Musso, C. Ratcliffe, P. Goldstraw, M. A. Pierotti, U. Pastorino, *Clin Cancer Res* **1999**, *5*, 2689-2692.
150. T. Lecomte, A. Berger, F. Zinzindohoue, S. Micard, B. Landi, H. Blons, P. Beaune, P. H. Cugnenc, P. Laurent-Puig, *Int J Cancer* **2002**, *100*, 542-548.
151. B. Vogelstein, K. W. Kinzler, *P Natl Acad Sci USA* **1999**, *96*, 9236-9241.
152. D. Dressman, H. Yan, G. Traverso, K. W. Kinzler, B. Vogelstein, *P Natl Acad Sci USA* **2003**, *100*, 8817-8822.

153. F. Diehl, M. Li, D. Dressman, Y. P. He, D. Shen, S. Szabo, L. A. Diaz, S. N. Goodman, K. A. David, H. Juhl, K. W. Kinzler, B. Vogelstein, *P Natl Acad Sci USA* **2005**, *102*, 16368-16373.
154. F. Diehl, K. Schmidt, M. A. Choti, K. Romans, S. Goodman, M. Li, K. Thornton, N. Agrawal, L. Sokoll, S. A. Szabo, K. W. Kinzler, B. Vogelstein, L. A. Diaz, Jr., *Nat Med* **2008**, *14*, 985-990.
155. T. Forshew, M. Murtaza, C. Parkinson, D. Gale, D. W. Y. Tsui, F. Kaper, S. J. Dawson, A. M. Piskorz, M. Jimenez-Linan, D. Bentley, J. Hadfield, A. P. May, C. Caldas, J. D. Brenton, N. Rosenfeld, *Sci Transl Med* **2012**, *4*.
156. R. J. Leary, M. Sausen, I. Kinde, N. Papadopoulos, J. D. Carpten, D. Craig, J. O'Shaughnessy, K. W. Kinzler, G. Parmigiani, B. Vogelstein, L. A. Diaz, Jr., V. E. Velculescu, *Sci Transl Med* **2012**, *4*, 162ra154.
157. K. C. Chan, P. Jiang, Y. W. Zheng, G. J. Liao, H. Sun, J. Wong, S. S. Siu, W. C. Chan, S. L. Chan, A. T. Chan, P. B. Lai, R. W. Chiu, Y. M. Lo, *Clin Chem* **2013**, *59*, 211-224.
158. E. Heitzer, P. Ulz, J. Belic, S. Gutschi, F. Quehenberger, K. Fischereder, T. Benezeder, M. Auer, C. Pischler, S. Mannweiler, M. Pichler, F. Eisner, M. Haeusler, S. Riethdorf, K. Pantel, H. Samonigg, G. Hoefler, H. Augustin, J. B. Geigl, M. R. Speicher, *Genome Med* **2013**, *5*, 30.
159. M. Murtaza, S. J. Dawson, D. W. Tsui, D. Gale, T. Forshew, A. M. Piskorz, C. Parkinson, S. F. Chin, Z. Kingsbury, A. S. Wong, F. Marass, S. Humphray, J. Hadfield, D. Bentley, T. M. Chin, J. D. Brenton, C. Caldas, N. Rosenfeld, *Nature* **2013**, *497*, 108-112.
160. D. S. Pisetsky, A. M. Fairhurst, *Autoimmunity* **2007**, *40*, 281-284.
161. A. Mantovani, S. Sozzani, M. Locati, P. Allavena, A. Sica, *Trends Immunol* **2002**, *23*, 549-555.
162. M. Stroun, J. Lyautey, C. Lederrey, A. Olson-Sand, P. Anker, *Clin Chim Acta* **2001**, *313*, 139-142.
163. E. W. H. To, K. C. A. Chan, S. F. Leung, L. Y. S. Chan, K. F. To, A. T. C. Chan, P. J. Johnson, Y. M. D. Lo, *Clin Cancer Res* **2003**, *9*, 3254-3259.
164. Y. M. D. Lo, J. Zhang, T. N. Leung, T. K. Lau, A. M. Z. Chang, N. M. Hjelm, *Am J Hum Genet* **1999**, *64*, 218-224.
165. W. Yao, C. Mei, X. Nan, L. Hui, *Gene* **2016**, *590*, 142-148.
166. C. Bettegowda, M. Sausen, R. J. Leary, I. Kinde, Y. Wang, N. Agrawal, B. R. Bartlett, H. Wang, B. Luber, R. M. Alani, E. S. Antonarakis, N. S. Azad, A. Bardelli, H. Brem, J. L. Cameron, C. C. Lee, L. A. Fecher, G. L. Gallia, P. Gibbs, D. Le, R. L. Giuntoli, M. Goggins, M. D. Hogarty, M. Holdhoff, S. M. Hong, Y. Jiao, H. H. Juhl, J. J. Kim, G. Siravegna, D. A. Laheru, C. Lauricella, M. Lim, E. J. Lipson, S. K. Marie, G. J. Netto, K. S. Oliner, A. Olivi, L. Olsson, G. J. Riggins, A. Sartore-Bianchi, K. Schmidt, M. Shih l, S. M. Oba-Shinjo, S. Siena, D. Theodorescu, J. Tie, T. T. Harkins, S. Veronese, T. L. Wang, J. D. Weingart, C. L. Wolfgang, L. D. Wood, D. Xing, R. H. Hruban, J. Wu, P. J. Allen, C. M. Schmidt, M. A. Choti, V. E. Velculescu,

K. W. Kinzler, B. Vogelstein, N. Papadopoulos, L. A. Diaz, Jr., *Sci Transl Med* **2014**, *6*, 224ra224.

167. M. J. Overman, J. Modak, S. Kopetz, R. Murthy, J. C. Yao, M. E. Hicks, J. L. Abbruzzese, A. L. Tam, *J Clin Oncol* **2013**, *31*, 17-22.
168. P. A. Vanderlaan, N. Yamaguchi, E. Folch, D. H. Boucher, M. S. Kent, S. P. Gangadharan, A. Majid, M. A. Goldstein, M. S. Huberman, O. N. Kocher, D. B. Costa, *Lung Cancer* **2014**, *84*, 39-44.
169. P. M. Ellis, F. A. Shepherd, M. Millward, F. Perrone, L. Seymour, G. Liu, S. Sun, B. C. Cho, A. Morabito, N. B. Leighl, M. R. Stockler, C. W. Lee, R. Wierzbicki, V. Cohen, N. Blais, R. S. Sangha, A. G. Favaretto, J. H. Kang, M. S. Tsao, C. F. Wilson, Z. Goldberg, K. Ding, G. D. Goss, P. A. Bradbury, C. T. G. Ncic, G. Australasian Lung Cancer Trials, N. C. I. N. C. T. Unit, *Lancet Oncol* **2014**, *15*, 1379-1388.
170. H. H. Popper, *Transl Lung Cancer Res* **2016**, *5*, 433-435.
171. L. De Mattos-Arruda, B. Weigelt, J. Cortes, H. H. Won, C. K. Ng, P. Nuciforo, F. C. Bidard, C. Aura, C. Saura, V. Peg, S. Piscuoglio, M. Oliveira, Y. Smolders, P. Patel, L. Norton, J. Tabernero, M. F. Berger, J. Seoane, J. S. Reis-Filho, *Ann Oncol* **2014**, *25*, 1729-1735.
172. R. Lebofsky, C. Decraene, V. Bernard, M. Kamal, A. Blin, Q. Leroy, T. R. Frio, G. Pierron, C. Callens, I. Bieche, A. Saliou, J. Madic, E. Rouleau, F. C. Bidard, O. Lantz, M. H. Stern, C. Le Tourneau, J. Y. Pierga, *Mol Oncol* **2015**, *9*, 783-790.
173. M. Jamal-Hanjani, G. A. Wilson, S. Horswell, R. Mitter, O. Sakarya, T. Constantin, R. Salari, E. Kirkizlar, S. Sigurjonsson, R. Pelham, S. Kareht, B. Zimmermann, C. Swanton, *Ann Oncol* **2016**, *27*, 862-867.
174. M. Murtaza, S. J. Dawson, K. Pogrebniak, O. M. Rueda, E. Provenzano, J. Grant, S. F. Chin, D. W. Tsui, F. Marass, D. Gale, H. R. Ali, P. Shah, T. Contente-Cuomo, H. Farahani, K. Shumansky, Z. Kingsbury, S. Humphray, D. Bentley, S. P. Shah, M. Wallis, N. Rosenfeld, C. Caldas, *Nat Commun* **2015**, *6*, 8760.
175. M. J. Duffy, *Clin Chem* **2006**, *52*, 345-351.
176. R. Fazel, H. M. Krumholz, Y. Wang, J. S. Ross, J. Chen, H. H. Ting, N. D. Shah, K. Nasir, A. J. Einstein, B. K. Nallamothu, *N Engl J Med* **2009**, *361*, 849-857.
177. L. Benesova, B. Belsanova, S. Suchanek, M. Kopeckova, P. Minarikova, L. Lipska, M. Levy, V. Visokai, M. Zavoral, M. Minarik, *Anal Biochem* **2013**, *433*, 227-234.
178. F. Mauger, C. Dulary, C. Daviaud, J. F. Deleuze, J. Tost, *Anal Bioanal Chem* **2015**, *407*, 6873-6878.
179. A. Szpechcinski, J. Chorostowska-Wynimko, R. Struniawski, W. Kupis, P. Rudzinski, R. Langfort, E. Puscinska, P. Bielen, P. Sliwinski, T. Orlowski, *Br J Cancer* **2015**, *113*, 476-483.
180. G. Perkins, T. A. Yap, L. Pope, A. M. Cassidy, J. P. Dukes, R. Riisnaes, C. Massard, P. A. Cassier, S. Miranda, J. Clark, K. A. Denholm, K. Thway, D. Gonzalez De Castro, G. Attard, L. R. Molife, S. B. Kaye, U. Banerji, J. S. de Bono, *PLoS One* **2012**, *7*, e47020.
181. K. L. G. Spindler, N. Pallisgaard, R. F. Andersen, I. Brandslund, A. Jakobsen, *Plos One* **2015**, *10*.

182. F. Mouliere, S. El Messaoudi, D. Pang, A. Dritschilo, A. R. Thierry, *Mol Oncol* **2014**, *8*, 927-941.
183. F. Mouliere, B. Robert, E. Arnau Peyrotte, M. Del Rio, M. Ychou, F. Molina, C. Gongora, A. R. Thierry, *PLoS One* **2011**, *6*, e23418.
184. M. Cristofanilli, P. Fortina, *N Engl J Med* **2013**, *369*, 93.
185. G. Siravegna, A. Bardelli, *Mol Oncol* **2016**, *10*, 475-480.
186. L. A. Diaz, Jr., A. Bardelli, *J Clin Oncol* **2014**, *32*, 579-586.
187. M. L. Metzker, *Nat Rev Genet* **2010**, *11*, 31-46.
188. S. Banerji, K. Cibulskis, C. Rangel-Escareno, K. K. Brown, S. L. Carter, A. M. Frederick, M. S. Lawrence, A. Y. Sivachenko, C. Sougnez, L. Zou, M. L. Cortes, J. C. Fernandez-Lopez, S. Peng, K. G. Ardlie, D. Auclair, V. Bautista-Pina, F. Duke, J. Francis, J. Jung, A. Maffuz-Aziz, R. C. Onofrio, M. Parkin, N. H. Pho, V. Quintanar-Jurado, A. H. Ramos, R. Rebollar-Vega, S. Rodriguez-Cuevas, S. L. Romero-Cordoba, S. E. Schumacher, N. Stransky, K. M. Thompson, L. Uribe-Figueroa, J. Baselga, R. Beroukhim, K. Polyak, D. C. Sgroi, A. L. Richardson, G. Jimenez-Sanchez, E. S. Lander, S. B. Gabriel, L. A. Garraway, T. R. Golub, J. Melendez-Zajgla, A. Toker, G. Getz, A. Hidalgo-Miranda, M. Meyerson, *Nature* **2012**, *486*, 405-409.
189. S. V. Bratman, A. M. Newman, A. A. Alizadeh, M. Diehn, *Expert Rev Mol Diagn* **2015**, *15*, 715-719.
190. N. Ogasawara, H. Bando, Y. Kawamoto, T. Yoshino, K. Tsuchihara, A. Ohtsu, H. Esumi, *Jpn J Clin Oncol* **2011**, *41*, 52-56.
191. Z. B. Chen, J. N. Feng, C. H. Buzin, Q. Liu, L. Weiss, K. Kernstine, G. Somlo, S. S. Sommer, *Plos One* **2009**, *4*.
192. I. Mancini, C. Santucci, R. Sestini, L. Simi, N. Pratesi, F. Cianchi, R. Valanzano, P. Pinzani, C. Orlando, *J Mol Diagn* **2010**, *12*, 705-711.
193. P. Carotenuto, C. Roma, S. Cozzolino, F. Fenizia, A. M. Rachiglio, F. Tatangelo, A. Iannaccone, L. Baron, G. Botti, N. Normanno, *Int J Oncol* **2012**, *40*, 378-384.
194. P. Pinzani, C. Santucci, I. Mancini, L. Simi, F. Salvianti, N. Pratesi, D. Massi, V. De Giorgi, M. Pazzagli, C. Orlando, *Clin Chim Acta* **2011**, *412*, 901-905.
195. C. Ausch, V. Buxhofer-Ausch, C. Oberkanins, B. Holzer, M. Minai-Pour, S. Jahn, N. Dandachi, R. Zeillinger, G. Kriegshauser, *J Mol Diagn* **2009**, *11*, 508-513.
196. M. J. Higgins, D. Jelovac, E. Barnathan, B. Blair, S. Slater, P. Powers, J. Zorzi, S. C. Jeter, G. R. Oliver, J. Fetting, L. Emens, C. Riley, V. Stearns, F. Diehl, P. Angenendt, P. Huang, L. Cope, P. Argani, K. M. Murphy, K. E. Bachman, J. Greshock, A. C. Wolff, B. H. Park, *Clin Cancer Res* **2012**, *18*, 3462-3469.
197. K. Taniguchi, J. Uchida, K. Nishino, T. Kumagai, T. Okuyama, J. Okami, M. Higashiyama, K. Kodama, F. Imamura, K. Kato, *Clin Cancer Res* **2011**, *17*, 7808-7815.
198. M. F. Sanmamed, S. Fernandez-Landazuri, C. Rodriguez, R. Zarate, M. D. Lozano, L. Zubiri, J. L. Perez-Gracia, S. Martin-Algarra, A. Gonzalez, *Clin Chem* **2015**, *61*, 297-304.

199. O. Abdel-Wahab, V. M. Klimek, A. A. Gaskell, A. Viale, D. Cheng, E. Kim, R. Rampal, M. Bluth, J. J. Harding, M. K. Callahan, T. Merghoub, M. F. Berger, D. B. Solit, N. Rosen, R. L. Levine, P. B. Chapman, *Cancer Discov* **2014**, *4*, 538-545.
200. G. R. Oxnard, C. P. Paweletz, Y. A. Kuang, S. L. Mach, A. O'Connell, M. M. Messineo, J. J. Luke, M. Butaney, P. Kirschmeier, D. M. Jackman, P. A. Janne, *Clin Cancer Res* **2014**, *20*, 1698-1705.
201. J. A. Beaver, D. Jelovac, S. Balukrishna, R. L. Cochran, S. Croessmann, D. J. Zabransky, H. Y. Wong, P. V. Toro, J. Cidado, B. G. Blair, D. Chu, T. Burns, M. J. Higgins, V. Stearns, L. Jacobs, M. Habibi, J. Lange, P. J. Hurley, J. Lauring, D. A. VanDenBerg, J. Kessler, S. Jeter, M. L. Samuels, D. Maar, L. Cope, A. Cimino-Mathews, P. Argani, A. C. Wolff, B. H. Park, *Clin Cancer Res* **2014**, *20*, 2643-2650.
202. S. J. Dawson, D. W. Tsui, M. Murtaza, H. Biggs, O. M. Rueda, S. F. Chin, M. J. Dunning, D. Gale, T. Forshew, B. Mahler-Araujo, S. Rajan, S. Humphray, J. Becq, D. Halsall, M. Wallis, D. Bentley, C. Caldas, N. Rosenfeld, *N Engl J Med* **2013**, *368*, 1199-1209.
203. J. Stadler, J. Eder, B. Pratscher, S. Brandt, D. Schneller, R. Mullegger, C. Vogl, F. Trautinger, G. Brem, J. P. Burgstaller, *Plos One* **2015**, *10*.
204. I. Kinde, J. Wu, N. Papadopoulos, K. W. Kinzler, B. Vogelstein, *Proceedings of the National Academy of Sciences of the United States of America* **2011**, *108*, 9530-9535.
205. A. R. Thierry, F. Mouliere, S. El Messaoudi, C. Mollevi, E. Lopez-Crapez, F. Rolet, B. Gillet, C. Gongora, P. Dechelotte, B. Robert, M. Del Rio, P. J. Lamy, F. Bibeau, M. Nouaille, V. Loriot, A. S. Jarrousse, F. Molina, M. Mathonnet, D. Pezet, M. Ychou, *Nat Med.* **2014**, *20*, 430-435.
206. H. Schwarzenbach, D. S. Hoon, K. Pantel, *Nat Rev Cancer* **2011**, *11*, 426-437.
207. C. A. Parkinson, D. Gale, A. M. Piskorz, H. Biggs, C. Hodgkin, H. Addley, S. Freeman, P. Moyle, E. Sala, K. Sayal, K. Hosking, I. Gounaris, M. Jimenez-Linan, H. M. Earl, W. Qian, N. Rosenfeld, J. D. Brenton, *PLoS Med* **2016**, *13*, e1002198.
208. S. E. Norton, K. K. Luna, J. M. Lechner, J. B. Qin, M. R. Fernando, *J Clin Lab Anal* **2013**, *27*, 305-311.
209. R. F. Andersen, K. L. G. Spindler, I. Brandslund, A. Jakobsen, N. Pallisgaard, *Clin Chim Acta* **2015**, *439*, 97-101.
210. S. O. Kelley, C. A. Mirkin, D. R. Walt, R. F. Ismagilov, M. Toner, E. H. Sargent, *Nat Nanotechnol* **2014**, *9*, 969-980.
211. S. O. Krabbenborg, C. Nicosia, P. Chen, J. Huskens, *Nat Commun* **2013**, *4*, 1667.
212. R. Corradini, S. Sforza, T. Tedeschi, F. Totsingan, A. Manicardi, R. Marchelli, *Curr Top Med Chem* **2011**, *11*, 1535-1554.
213. R. D'Agata, G. Spoto, *Artif DNA PNA XNA* **2012**, *3*, 45-52.
214. M. Li, S. K. Cushing, N. Wu, *Analyst* **2015**, *140*, 386-406.
215. L. M. Zanoli, R. D'Agata, G. Spoto, *Anal Bioanal Chem* **2012**, *402*, 1759-1771.
216. K. A. Hyun, J. Kim, H. Gwak, H. I. Jung, *Analyst* **2016**, *141*, 382-392.

217. B. Hongxia, L. Ruiyi, L. Zaijun, L. Junkang, G. Zhiguo, W. Guangli, *RSC Advances* **2015**, *5*, 54211-54219.
218. K. J. Liu, M. V. Brock, M. Shih Ie, T. H. Wang, *J Am Chem Soc* **2010**, *132*, 5793-5798.
219. Y. H. Su, M. Wang, D. E. Brenner, P. A. Norton, T. M. Block, *Ann N Y Acad Sci* **2008**, *1137*, 197-206.
220. F. Diehl, K. Schmidt, K. H. Durkee, K. J. Moore, S. N. Goodman, A. P. Shuber, K. W. Kinzler, B. Vogelstein, *Gastroenterology* **2008**, *135*, 489-498.
221. M. J. Sorich, M. D. Wiese, A. Rowland, G. Kichenadasse, R. A. McKinnon, C. S. Karapetis, *Ann Oncol* **2015**, *26*, 13-21.
222. C. Therkildsen, T. K. Bergmann, T. Henrichsen-Schnack, S. Ladelund, M. Nilbert, *Acta Oncol* **2014**, *53*, 852-864.
223. S. Benvenuti, A. Sartore-Bianchi, F. Di Nicolantonio, C. Zanon, M. Moroni, S. Veronese, S. Siena, A. Bardelli, *Cancer Res* **2007**, *67*, 2643-2648.
224. I. A. Prior, J. F. Hancock, *Semin Cell Dev Biol* **2012**, *23*, 145-153.
225. A. R. Thierry, *Methods Mol Biol* **2016**, *1392*, 1-16.
226. J. Downward, *Nat Rev Cancer* **2003**, *3*, 11-22.
227. T. Minamoto, M. Mai, Z. Ronai, *Cancer Detect Prev* **2000**, *24*, 1-12.
228. S. Schubbert, K. Shannon, G. Bollag, *Nat Rev Cancer* **2007**, *7*, 295-308.
229. G. D. Sorenson, D. M. Pribish, F. H. Valone, V. A. Memoli, D. J. Bzik, S. L. Yao, *Cancer Epidemiol Biomarkers Prev* **1994**, *3*, 67-71.
230. C. S. Karapetis, S. Khambata-Ford, D. J. Jonker, C. J. O'Callaghan, D. Tu, N. C. Tebbutt, R. J. Simes, H. Chalchal, J. D. Shapiro, S. Robitaille, T. J. Price, L. Shepherd, H. J. Au, C. Langer, M. J. Moore, J. R. Zalcberg, *N Engl J Med* **2008**, *359*, 1757-1765.
231. S. Siena, A. Sartore-Bianchi, F. Di Nicolantonio, J. Balfour, A. Bardelli, *J Natl Cancer Inst* **2009**, *101*, 1308-1324.
232. I. A. Cree, *Expert Rev Mol Diagn* **2016**, *16*, 1067-1072.
233. C. Guerra, N. Mijimolle, A. Dhawahir, P. Dubus, M. Barradas, M. Serrano, V. Campuzano, M. Barbacid, *Cancer Cell* **2003**, *4*, 111-120.
234. M. Barbacid, *Eur J Clin Invest* **1990**, *20*, 225-235.
235. S. Rodenhuis, R. J. C. Slebos, *Am Rev Respir Dis* **1990**, *142*, S27-S30.
236. S. J. Clayton, F. M. Scott, J. Walker, K. Callaghan, K. Haque, T. Liloglou, G. Xinarianos, S. Shawcross, P. Ceuppens, J. K. Field, J. C. Fox, *Clin Chem* **2000**, *46*, 1929-1938.
237. K. Scheffzek, M. R. Ahmadian, W. Kabsch, L. Wiesmuller, A. Lautwein, F. Schmitz, A. Wittinghofer, *Science* **1997**, *277*, 333-338.
238. S. Jancik, J. Drabek, D. Radzioch, M. Hajduch, *J Biomed Biotechnol* **2010**, *2010*, 150960.
239. F. Perrone, A. Lampis, C. Bertan, P. Verderio, C. M. Ciniselli, S. Pizzamiglio, M. Frattini, M. Nucifora, F. Molinari, G. Gallino, M. Gariboldi, E. Meroni, E. Leo, M. A. Pierotti, S. Pilotti, *Tumori* **2014**, *100*, 115-121.

240. D. Gonzalez de Castro, B. Angulo, B. Gomez, D. Mair, R. Martinez, A. Suarez-Gauthier, F. Shieh, M. Velez, V. H. Brophy, H. J. Lawrence, F. Lopez-Rios, *Br J Cancer* **2012**, *107*, 345-351.
241. L. Bolton, A. Reiman, K. Lucas, J. Timms, I. A. Cree, *PLoS One* **2015**, *10*, e0115672.
242. V. Whitehall, K. Tran, A. Umapathy, F. Grieu, C. Hewitt, T. J. Evans, T. Ismail, W. Q. Li, P. Collins, P. Ravetto, B. Leggett, M. Salto-Tellez, R. Soong, S. Fox, R. J. Scott, A. Dobrovic, B. Iacopetta, *J Mol Diagn* **2009**, *11*, 543-552.
243. J. R. Dijkstra, D. A. Heideman, G. A. Meijer, J. E. Boers, N. A. t Hart, J. Diebold, A. Hirschmann, G. Hoefler, G. Winter, G. Miltenberger-Miltenyi, S. V. Pereira, S. D. Richman, P. Quirke, E. L. Rouleau, J. M. Guinebretiere, S. Tejpar, B. Biesmans, J. H. van Krieken, *Virchows Arch* **2013**, *462*, 39-46.
244. I. Bando, L. Cillero, J. Sanz-Ortega, P. Llovet, P. Pescador, M. Ferrer, M. de la Hoya, J. Sastre, E. D. Garcia, T. Caldes, *Clin Transl Oncol* **2012**, *14*, 937-942.
245. K. M. Woo, V. J. Chen, P. X. Ma, *J Biomed Mater Res A* **2003**, *67*, 531-537.
246. T. Boontheekul, D. J. Mooney, *Curr opin in biotechnol* **2003**, *14*, 559-565.
247. K. Maehashi, T. Katsura, K. Kerman, Y. Takamura, K. Matsumoto, E. Tamiya, *Anal Chem* **2007**, *79*, 782-787.
248. C. A. Rowe, L. M. Tender, M. J. Feldstein, J. P. Golden, S. B. Scruggs, B. D. MacCraith, J. J. Cras, F. S. Ligler, *Anal Chem* **1999**, *71*, 3846-3852.
249. X. Liu, L. Yuan, D. Li, Z. Tang, Y. Wang, G. Chen, H. Chen, J. L. Brash, *J Mater Chem B* **2014**, *2*, 5718-5738.
250. Z. Tang, X. Liu, Y. Luan, W. Liu, Z. Wu, D. Li, H. Chen, *Polym Chem* **2013**, *4*, 5597-5602.
251. P. Vadgama, S. Anastasova, A. Spehar-Deleze, in *Detection Challenges in Clinical Diagnostics*, The Royal Society of Chemistry, **2013**, pp. 35-64.
252. I. Banerjee, R. C. Pangule, R. S. Kane, *Adv Mater* **2011**, *23*, 690-718.
253. M. Thompson, C. Blaszykowski, S. Sheikh, C. Rodriguez-Emmenegger, A. de los Santos Pereira, in *Biological Fluid-Surface Interactions in Detection and Medical Devices*, The Royal Society of Chemistry, **2017**, pp. 184-265.
254. L. C. Xu, J. W. Bauer, C. A. Siedlecki, *Colloids Surf B Biointerfaces* **2014**, *124*, 49-68.
255. A. A. Thyparambil, Y. Wei, R. A. Latour, *Biointerphases* **2015**, *10*, 019002.
256. E. P. Childers, G. I. Peterson, A. B. Ellenberger, K. Domino, G. V. Seifert, M. L. Becker, *Biomacromolecules* **2016**, *17*, 3396-3403.
257. M. Rabe, D. Verdes, S. Seeger, *Adv Colloid Interface Sci* **2011**, *162*, 87-106.
258. E. A. Vogler, *Biomaterials* **2012**, *33*, 1201-1237.
259. T. S. Tsapikouni, Y. F. Missirlis, *Mater Sci Eng B* **2008**, *152*, 2-7.
260. P. Lin, C. W. Lin, R. Mansour, F. Gu, *Biosens Bioelectron* **2013**, *47*, 451-460.
261. M Mrksich, G. M. Whitesides, *Annu Rev Biophys Biomol Struct* **1996**, *25*, 55-78.
262. J. D. Andrade, V. Hlady, *Ann N Y Acad Sci* **1987**, *516*, 158-172.
263. S. Pasche, J. Voros, H. J. Griesser, N. D. Spencer, M. Textor, *J Phys Chem B* **2005**, *109*, 17545-17552.

264. S. L. Hirsh, D. R. McKenzie, N. J. Nosworthy, J. A. Denman, O. U. Sezerman, M. M. Bilek, *Colloids Surf B Biointerfaces* **2013**, *103*, 395-404.
265. J. D. Andrade, V. Hlady, Springer Berlin Heidelberg, Berlin, Heidelberg, **1986**, pp. 1-63.
266. A. Halperin, *Langmuir* **1999**, *15*, 2525-2533.
267. P. Vermette, S. Taylor, D. Dunstan, L. Meagher, *Langmuir* **2002**, *18*, 505-511.
268. P. E. Scopelliti, A. Borgonovo, M. Indrieri, L. Giorgetti, G. Bongiorno, R. Carbone, A. Podesta, P. Milani, *PLoS One* **2010**, *5*, e11862.
269. P. G. Koutsoukos, W. Norde, J. Lyklema, *J Colloid Interface Sci* **1983**, *95*, 385-397.
270. S. Chen, L. Li, C. Zhao, J. Zheng, *Polymer* **2010**, *51*, 5283-5293.
271. M. Wei, Y. Gao, X. Li, M. J. Serpe, *Polym Chem* **2017**, *8*, 127-143.
272. Y. Akdogan, W. Wei, K.-Y. Huang, Y. Kageyama, E. W. Danner, D. R. Miller, N. R. Martinez Rodriguez, J. H. Waite, S. Han, *Angew Chem Int Ed* **2014**, *53*, 11253-11256.
273. X. Huang, Y. Sun, S. Soh, *Adv Mater* **2015**, *27*, 4062-4068.
274. P. Y. Qian, L. Chen, Y. Xu, *Biofouling* **2013**, *29*, 381-400.
275. C. Zhao, L. Li, Q. Wang, Q. Yu, J. Zheng, *Langmuir* **2011**, *27*, 4906-4913.
276. T. Goda, M. Tabata, M. Sanjoh, M. Uchimura, Y. Iwasaki, Y. Miyahara, *Chem Commun (Camb)* **2013**, *49*, 8683-8685.
277. S. Seo, S. Das, P. J. Zalicki, R. Mirshafian, C. D. Eisenbach, J. N. Israelachvili, J. H. Waite, B. K. Ahn, *J Am Chem Soc* **2015**, *137*, 9214-9217.
278. K. Anselme, P. Davidson, A. M. Popa, M. Giazzon, M. Liley, L. Ploux, *Acta Biomater* **2010**, *6*, 3824-3846.
279. S. I. Jeon, J. H. Lee, J. D. Andrade, P. G. De Gennes, *J Colloid Interface Sci* **1991**, *142*, 149-158.
280. Y. He, Y. Chang, J. C. Hower, J. Zheng, S. Chen, S. Jiang, *Phys Chem Chem Phys* **2008**, *10*, 5539-5544.
281. C. X. Liu, D. R. Zhang, Y. He, X. S. Zhao, R. Bai, *J Membr Sci* **2010**, *346*, 121-130.
282. D. Rana, T. Matsuura, *Chem Rev* **2010**, *110*, 2448-2471.
283. P. A. Mulheran, D. J. Connell, K. Kubiak-Ossowska, *RSC Advances* **2016**, *6*, 73709-73716.
284. L. Mi, S. Jiang, *Angew Chem Int Ed Engl* **2014**, *53*, 1746-1754.
285. H. Zhang, M. Chiao, *J Med Biol Eng* **2015**, *35*, 143-155.
286. L. M. Szott, M. J. Stein, B. D. Ratner, T. A. Horbett, *J Biomed Mater Res A* **2011**, *96*, 150-161.
287. M. C. Sin, S. H. Chen, Y. Chang, *Polym J* **2014**, *46*, 436-443.
288. J. Deng, T. Ren, J. Zhu, Z. Mao, C. Gao, *Regen Biomater* **2014**, *1*, 17-25.
289. F. Zhou, *Antifouling Surfaces and Materials-From Land to Marine Environment*, 1 ed., Springer-Verlag Berlin Heidelberg, **2015**.
290. Y. Nagasaki, *Polym J* **2011**, *43*, 949-958.
291. P. Kingshott, H. Thissen, H. J. Griesser, *Biomaterials* **2002**, *23*, 2043-2056.
292. S. Lowe, N. M. O'Brien-Simpson, L. A. Connal, *Polym Chem* **2015**, *6*, 198-212.

293. E. M. Clop, M. A. Perillo, A. K. Chattah, *J Phys Chem B* **2012**, *116*, 11953-11958.

294. P. Gasteier, A. Reska, P. Schulte, J. Salber, A. Offenhausser, M. Moeller, J. Groll, *Macromol Biosci* **2007**, *7*, 1010-1023.

295. L. D. Unsworth, Z. Tun, H. Sheardown, J. L. Brash, *J Colloid Interface Sci* **2005**, *281*, 112-121.

296. T. Riedel, Z. Riedelova-Reicheltova, P. Majek, C. Rodriguez-Emmenegger, M. Houska, J. E. Dyr, E. Brynda, *Langmuir* **2013**, *29*, 3388-3397.

297. P. Chapman, R. E. Ducker, C. R. Hurley, J. K. Hobbs, G. J. Leggett, *Langmuir* **2015**, *31*, 5935-5944.

298. V. B. Damodaran, N. S. Murthy, *Biomater Res* **2016**, *20*, 18.

299. J. Ulbricht, R. Jordan, R. Luxenhofer, *Biomaterials* **2014**, *35*, 4848-4861.

300. Q. Wei, T. Becherer, S. Angioletti-Uberti, J. Dzubiella, C. Wischke, A. T. Neffe, A. Lendlein, M. Ballauff, R. Haag, *Angew Chem Int Ed Engl* **2014**, *53*, 8004-8031.

301. H.-J. Sung, A. Luk, N. S. Murthy, E. Liu, M. Jois, A. Joy, J. Bushman, P. V. Moghe, J. Kohn, *Soft Matter* **2010**, *6*, 5196-5205.

302. T. Weber, M. Bechthold, T. Winkler, J. Dauselt, A. Terfort, *Colloids Surf B Biointerfaces* **2013**, *111*, 360-366.

303. R. Konradi, C. Acikgoz, M. Textor, *Macromol Rapid Comm* **2012**, *33*, 1663-1676.

304. A. I. Lopez, A. Kumar, M. R. Planas, Y. Li, T. V. Nguyen, C. Cai, *Biomaterials* **2011**, *32*, 4336-4346.

305. V. B. Damodaran, V. Leszczak, K. A. Wold, S. M. Lantvit, K. C. Popat, M. M. Reynolds, *RSC Advances* **2013**, *3*, 24406-24414.

306. Q. Shao, S. Jiang, *Adv Mater* **2015**, *27*, 15-26.

307. C. M. Kirschner, A. B. Brennan, *Annu Rev Mater Res* **2012**, *42*, 211-229.

308. S. Chen, F. Yu, Q. Yu, Y. He, S. Jiang, *Langmuir* **2006**, *22*, 8186-8191.

309. H. Vaisocherova, W. Yang, Z. Zhang, Z. Cao, G. Cheng, M. Piliarik, J. Homola, S. Jiang, *Anal Chem* **2008**, *80*, 7894-7901.

310. Z. Zhang, S. Chen, S. Jiang, *Biomacromolecules* **2006**, *7*, 3311-3315.

311. G. Cheng, H. Xue, Z. Zhang, S. Chen, S. Jiang, *Angew Chem Int Ed Engl* **2008**, *47*, 8831-8834.

312. J. Ladd, Z. Zhang, S. Chen, J. C. Hower, S. Jiang, *Biomacromolecules* **2008**, *9*, 1357-1361.

313. R. E. Holmlin, X. Chen, R. G. Chapman, S. Takayama, G. M. Whitesides, *Langmuir* **2001**, *17*, 2841-2850.

314. M. T. Bernards, G. Cheng, Z. Zhang, S. Chen, S. Jiang, *Macromolecules* **2008**, *41*, 4216-4219.

315. S. Chen, S. Jiang, *Adv Mater* **2008**, *20*, 335-338.

316. Q. Zhang, M. Li, C. Zhu, G. Nurumbetov, Z. Li, P. Wilson, K. Kempe, D. M. Haddleton, *J Am Chem Soc* **2015**, *137*, 9344-9353.

317. Q. Liu, W. Li, A. Singh, G. Cheng, L. Liu, *Acta Biomater* **2014**, *10*, 2956-2964.

318. H. Chen, M. Zhang, J. Yang, C. Zhao, R. Hu, Q. Chen, Y. Chang, J. Zheng, *Langmuir* **2014**, *30*, 10398-10409.

319. J. E. Krause, N. D. Brault, Y. Li, H. Xue, Y. Zhou, S. Jiang, *Macromolecules* **2011**, *44*, 9213-9220.

320. A. S. Knight, E. Y. Zhou, M. B. Francis, R. N. Zuckermann, *Adv Mater* **2015**, *27*, 5665-5691.

321. K. Wang, A. A. Abdalla, M. A. Khaleel, N. Hilal, M. K. Khraisheh, *Desalination* **2017**, *401*, 190-205.

322. H. Vaisocherova, E. Brynda, J. Homola, *Anal Bioanal Chem* **2015**, *407*, 3927-3953.

323. Y. Chang, S.-H. Shu, Y.-J. Shih, C.-W. Chu, R.-C. Ruaan, W.-Y. Chen, *Langmuir* **2010**, *26*, 3522-3530.

324. Z. Lin, Y. Yang, A. Zhang, *Polymer-Engineered Nanostructures for Advanced Energy Applications*, 1 ed., Springer International Publishing, **2017**.

325. H. Ye, L. Wang, R. Huang, R. Su, B. Liu, W. Qi, Z. He, *ACS Appl Mater Interfaces* **2015**, *7*, 22448-22457.

326. A. K. Nowinski, F. Sun, A. D. White, A. J. Keefe, S. Jiang, *J Am Chem Soc* **2012**, *134*, 6000-6005.

327. C. Leng, H. G. Buss, R. A. Segalman, Z. Chen, *Langmuir* **2015**, *31*, 9306-9311.

328. I. C. Kruis, D. W. P. M. Löwik, W. C. Boelens, J. C. M. van Hest, G. J. M. Pruijn, *Analyst* **2016**, *141*, 5321-5328.

329. W. van Zoelen, H. G. Buss, N. C. Ellebracht, N. A. Lynd, D. A. Fischer, J. Finlay, S. Hill, M. E. Callow, J. A. Callow, E. J. Kramer, R. N. Zuckermann, R. A. Segalman, *ACS Macro Letters* **2014**, *3*, 364-368.

330. J. Pei, H. Hall, N. D. Spencer, *Biomaterials* **2011**, *32*, 8968-8978.

331. R. Ogaki, O. Zoffmann Andersen, G. V. Jensen, K. Kolind, D. C. E. Kraft, J. S. Pedersen, M. Foss, *Biomacromolecules* **2012**, *13*, 3668-3677.

332. B. Pidhatika, M. Rodenstein, Y. Chen, E. Rakhmatullina, A. Mühlebach, C. Acikgöz, M. Textor, R. Konradi, *Biointerphases* **2012**, *7*, 1.

333. J. K. West, R. Latour, L. L. Hench, *J Biomed Mater Res* **1997**, *37*, 585-591.

334. M. Schuler, G. R. Owen, D. W. Hamilton, M. de Wild, M. Textor, D. M. Brunette, S. G. P. Tosatti, *Biomaterials* **2006**, *27*, 4003-4015.

335. S. Lee, N. D. Spencer, *Langmuir* **2008**, *24*, 9479-9488.

336. S. G. Zhu, J. J. Xiang, X. L. Li, S. R. Shen, H. B. Lu, J. Zhou, W. Xiong, B. C. Zhang, X. M. Nie, M. Zhou, K. Tang, G. Y. Li, *Biotechnol Appl Biochem* **2004**, *39*, 179-187.

337. I. Szilagyi, G. Trefalt, A. Tiraferri, P. Maroni, M. Borkovec, *Soft Matter* **2014**, *10*, 2479-2502.

338. J. Borges, J. M. Campina, A. F. Silva, *J Phys Chem B* **2013**, *117*, 16565-16576.

339. C. Satriano, S. Svedhem, B. Kasemo, *Phys Chem Chem Phys* **2012**, *14*, 16695-16698.

340. M. Jiang, I. Popa, P. Maroni, M. Borkovec, *Colloid Surface A* **2010**, *360*, 20-25.

341. M. Porus, P. Maroni, M. Borkovec, *Langmuir* **2012**, *28*, 17506-17516.

342. D. Mazia, G. Schatten, W. Sale, *J Cell Biol* **1975**, *66*, 198-200.

343. S. Gac-Breton, J. Coudane, M. Boustta, M. Vert, *J Drug Target* **2004**, *12*, 297-307.
344. Y. H. Choi, F. Liu, J. S. Kim, Y. K. Choi, J. S. Park, S. W. Kim, *J Control Release* **1998**, *54*, 39-48.
345. S. Hwa Kim, J. Hoon Jeong, C. O. Joe, T. Gwan Park, *J Control Release* **2005**, *103*, 625-634.
346. S. R. Hynes, M. F. Rauch, J. P. Bertram, E. B. Lavik, *J Biomed Mater Res A* **2009**, *89A*, 499-509.
347. S. Morgenthaler, C. Zink, B. Stadler, J. Voros, S. Lee, N. D. Spencer, S. G. Tosatti, *Biointerphases* **2006**, *1*, 156-165.
348. A. Germini, A. Mezzelani, F. Lesignoli, R. Corradini, R. Marchelli, R. Bordoni, C. Consolandi, G. De Bellis, *J Agr Food Chem* **2004**, *52*, 4535-4540.
349. G. Grasso, R. D'Agata, E. Rizzarelli, G. Spoto, L. D'Andrea, C. Pedone, A. Picardi, A. Romanelli, M. Fragai, K. J. Yeo, *J Mass Spectrom* **2005**, *40*, 1565-1571.
350. R. D'Agata, P. Palladino, G. Spoto, *Beilstein J Nanotechnol* **2017**, *8*, 1-11.
351. T. L. Mann, U. J. Krull, *Biosens Bioelectron* **2004**, *20*, 945-955.
352. X. Duan, L. Y. Mu, S. D. Sawtelle, N. K. Rajan, Z. Y. Han, Y. Y. Wang, H. M. Qu, M. A. Reed, *Adv Funct Mater* **2015**, *25*, 2279-2286.
353. L. S. Jung, C. T. Campbell, T. M. Chinowsky, M. N. Mar, S. S. Yee, *Langmuir* **1998**, *14*, 5636-5648.
354. H. Fischer, I. Polikarpov, A. F. Craievich, *Protein Sci* **2004**, *13*, 2825-2828.
355. J. Voros, *Biophys J* **2004**, *87*, 553-561.
356. C. E. Jordan, A. G. Frutos, A. J. Thiel, R. M. Corn, *Anal Chem* **1997**, *69*, 4939-4947.
357. H. Y. Zhao, P. H. Brown, P. Schuckt, *Biophys J* **2011**, *100*, 2309-2317.
358. B. L. Frey, R. M. Corn, *Anal Chem* **1996**, *68*, 3187-3193.
359. S. Sheikh, D. Y. Yang, C. Blaszykowski, M. Thompson, *Chem Commun* **2012**, *48*, 1305-1307.
360. I. Reviakine, D. Johannsmann, R. P. Richter, *Anal Chem* **2011**, *83*, 8838-8848.
361. H. Wiig, O. Kolmannskog, O. Tenstad, J. L. Bert, *J Physiol* **2003**, *550*, 505-514.
362. P. Akkahat, S. Kiatkamjornwong, S.-i. Yusa, V. P. Hoven, Y. Iwasaki, *Langmuir* **2012**, *28*, 5872-5881.
363. C. Situ, A. R. G. Wylie, A. Douglas, C. T. Elliott, *Talanta* **2008**, *76*, 832-836.
364. K. Uchida, Y. Hoshino, A. Tamura, K. Yoshimoto, S. Kojima, K. Yamashita, I. Yamanaka, H. Otsuka, K. Kataoka, Y. Nagasaki, *Biointerphases* **2007**, *2*, 126-130.
365. S. Pasche, J. Voros, H. J. Griesser, N. D. Spencer, M. Textor, *J Phys Chem B* **2005**, *109*, 17545-17552.
366. N. Xia, L. Liu, M. G. Harrington, J. Wang, F. Zhou, *Anal Chem* **2010**, *82*, 10151-10157.
367. F. Fernandez, K. Hegnerova, M. Piliarik, F. Sanchez-Baeza, J. Homola, M. P. Marco, *Biosens Bioelectron* **2010**, *26*, 1231-1238.

368. H. Vaisocherova, V. Sevcu, P. Adam, B. Spackova, K. Hegnerova, A. de los Santos Pereira, C. Rodriguez-Emmenegger, T. Riedel, M. Houska, E. Brynda, J. Homola, *Biosens Bioelectron* **2014**, *51*, 150-157.
369. T. Riedel, Z. Riedelová-Reicheltová, P. Májek, C. Rodriguez-Emmenegger, M. Houska, J. E. Dyr, E. Brynda, *Langmuir* **2013**, *29*, 3388-3397.

Publications

Journal Articles:

Biosensors for liquid biopsy: circulating nucleic acids to diagnose and treat cancer
N. Bellassai, G. Spoto, *Anal Bioanal Chem* **2016**, *408*, 7255-7264.

Low-fouling, mixed-charge poly-L-lysine polymers with anionic oligopeptide side-chains
N. Bellassai, A. Marti, J. Huskens, G. Spoto, *J Mater Chem B* **2018,** doi:10.1039/c8tb01619d.

A new PEG-dendrimer zwitterionic compound with superior performance for antifouling applications
(in preparation)

Oral Presentations:

New antifouling platform for DNA detection in human plasma based on modified poly-L-lysine polymers with anionic peptide
N. Bellassai, A. Marti, J. Huskens, G. Spoto
XXVII Congress of the Analytical Chemistry Division, Bologna, Italy, 16th-20th September, **2018**

Protein adsorption studies of low-fouling zwitterionic polymer by complementary SPR and QCM techniques
N. Bellassai, A. Marti Morant, G. Spoto, J. Huskens
7th EuCheMS Chemistry Congress, ACC Liverpool, UK, 26th–30th August, **2018**

Protein adsorption studies of low-fouling, mixed-charge, zwitterionic polymer by complementary SPR and QCM techniques
N. Bellassai, A. Marti Morant, G. Spoto, J. Huskens
Incontro Spettroscopia Analitica ISA 2018, Cagliari, Italy, 5th – 8th June, **2018**

Complementary SPR and QCM techniques for the characterization of low fouling, mixed-charged zwitterionic polymer
N. Bellassai, A. Marti Morant, G. Spoto, J. Huskens
Winterschool on Biophotonics and Bioelectronics, Hirschegg, Austria, 19th – 24th February, **2018**

Sviluppo di nuovi polimeri zwitterionici per superfici antifouling mediante tecniche SPR e QCM
N. Bellassai, A. Marti Morant, G. Spoto, J. Huskens
Congresso Congiunto delle Sezioni Sicilia e Calabria SCI 2018, Catania, Italy, 9th – 10th February, **2018**, p. 29

Posters Presentations:

Development of a biosensing antifouling platform for DNA detection
N. Bellassai, A. Marti Morant, J. Huskens, G. Spoto
CONVENTIONAL AND HIGH-ENERGY SPECTROSCOPIES FOR INORGANIC, ORGANIC AND BIOMOLECULAR SURFACES AND INTERFACES (CHESS 2017). An unconventional school for PhD students & young investigators, Florence, Italy, 27th – 30th November, **2017**, p.13

Nanostructured antifouling polymer for DNA detection
N. Bellassai, A. Marti Morant, J. Huskens, G. Spoto
NanoBio&Med2017 Conference, Barcelona, Spain, 22nd – 24th November, **2017**, Editor: Phantoms Foundation, ISBN: 978-84-697-7905-7, p.101

Co-authored Presentations:

Nanoparticle-enhanced Surface Plasmon Resonance Imaging for the detection of genomic DNA: properties and role of functionalized gold nanoparticles
R. D'Agata, M.C. Giuffrida, N. Bellassai, A.M. Aura, M. Calcagno, C. Valenti, G. Spoto
Nano and Photonics Conference, Mauterndorf, Salzburg, Austria, 22nd – 25th March, **2017**, p.22

Surface plasmon resonance imaging detection of foodborne pathogens by using PNA probes and gold nanoparticles
A.M. Aura, R. D'Agata, N. Bellassai, C. Valenti, G. Spoto
XXV Congresso Nazionale della Divisione di Chimica Analitica della Società Chimica Italiana (SCI), Trieste, Italy, 13th – 17th September, **2015**, Editor: Antonella Rossi, Co-editor: Gianpiero Adami, published online September 14th, 2015, at University of Trieste, ISBN: 978-88-907670-2-9, p. 179

Internship:

Internship at the University of Twente, Erasmus Plus Project 2016 (grant recipient)
Molecular Nanofabrication group (MnF), Prof.dr.ir. Jurriaan Huskens
University of Twente, Enschede, The Netherlands, from 1st February to 31st July, 2017 (6 months)

PhD Courses:

Project Writing Course 2018
University of Catania, Catania, Italy, March, **2018**

Biosensors
University of Catania, Catania, Italy, September, **2017**

Workweek MnF and BnT
University of Ghent, Ghent, Belgium, 16th – 19th May, **2017**

Supramolecular Chemistry Course 2017

University of Groningen, University of Twente, University of Technology in Eindhoven, The Netherlands, 22nd – 23rd June, 8th – 9th June, 9th – 10th May, **2017**

Scientific Writing Course 2016

University of Catania, Catania, Italy, 9th – 10th June, **2016**

Project meetings:

UltraPlacad Meeting M42, end user Workshop and Final Event

Italian National Cancer Institute Regina Elena and Villino Eclettico, Rome, Italy, 24th – 26th October, **2018**

UltraPlacad Meeting M36

Future Diagnostics, Wijchen, The Netherlands, 15th – 16th May, **2018**

UltraPlacad Meeting M24

Horiba Center, Palaiseau, France, 30th – 31st May, **2017**

UltraPlacad Meeting M18

Bruxelles, Belgium, 2nd – 4th November, **2016**

UltraPlacad Kick Off Meeting

Catania, Italy, 6th – 8th May, **2015**

Supplementary Materials

Table of contents

Table S1. $\Delta\%R_{PNA\ G12D}$, $\Delta\%R_{PNA\ WT}$ and $\Delta\%R_{PNA\ G12D}/\Delta\%R_{PNA\ WT}$ values obtained from three replicated experiments aimed at detecting 5 pg μL^{-1} solutions of WT and G12D non-amplified genomic DNAs after 1500 s of adsorption of conjugated AuNPs.

Table S2. $\Delta\%R_{PNA\ G12V}$, $\Delta\%R_{PNA\ WT}$ and $\Delta\%R_{PNA\ G12V}/\Delta\%R_{PNA\ WT}$ values obtained from three replicated experiments aimed at detecting 5 pg μL^{-1} solutions of WT and G12V non-amplified genomic DNAs after 1500 s of adsorption of conjugated AuNPs.

Table S3. $\Delta\%R_{PNA\ G13D}$, $\Delta\%R_{PNA\ WT}$ and $\Delta\%R_{PNA\ G13D}/\Delta\%R_{PNA\ WT}$ values obtained from three replicated experiments aimed at detecting 5 pg μL^{-1} solutions of WT and G13D non-amplified genomic DNAs after 1500 s of adsorption of conjugated AuNPs.

Figure S1. Mass spectrum of oligopeptide CEEEEE after purification, using 90 % Milli-Q water and 10 % acetonitrile.

Figure S2. Scheme of PLL-mal(y%) synthesis.

Figure S3. ^{1}H-NMR spectrum of PLL-mal(26%) after purification recorded on a Bruker 400 MHz spectrometer. Chemical shifts are reported in ppm with tetramethylsilane as an internal standard.

Figure S4. ^{1}H-NMR spectrum of PLL-mal(22%) after purification recorded on a Bruker 400 MHz spectrometer. Chemical shifts are reported in ppm with tetramethylsilane as an internal standard.

Figure S5. ^{1}H-NMR spectrum of PLL-mal(13%) after purification recorded on a Bruker 400 MHz spectrometer. Chemical shifts are reported in ppm with tetramethylsilane as an internal standard.

Figure S6. PM-IRRAS spectra of PLL–mal(22%) deposited on a gold chip (black line, bottom), and PLL-mal(22%)-CEEEEE (grey line, top) after the coupling reaction with CEEEEE.

Figure S7. PM-IRRAS spectra of PLL–mal(13%) deposited on a gold chip (black line, bottom), and PLL-mal(13%)-CEEEEE (grey line, top) after the coupling reaction with CEEEEE.

Table S4. Surface coverage (ng cm^{-2}) of PLL-mal(26%), CEEEEE and molar ratio of CEEEEE to the PLL-mal(26%) for the evaluation of the coupling efficiency estimated by SPRI.

Figure S8. Surface coverage (ng cm^{-2}) of BSA adsorption on PLL-mal(26%)-CEEEEE silicon oxide surface measured by QCM-D.

Table S5. Surface coverage (ng cm^{-2}) of BSA adsorption on PLL-mal(26%)-CEEEEE silicon oxide surface measured by QCM-D on silicon oxide surface.

Figure S9. QCM-D antifouling tests using diluted human plasma samples and PLL-mal(26%)-CEEEEE on silicon oxide surface.

Table S6. Surface coverages of protein (ng cm^{-2}) from diluted human plasma samples on PLL-mal(26%)-CEEEEE silicon oxide surface estimated by QCM-D.

Table S7. $\Delta\%R_{\text{PNA G12D}}$, $\Delta\%R_{\text{PNA WT}}$ and $\Delta\%R_{\text{PNA G12D}}/\Delta\%R_{\text{PNA WT}}$ values obtained from ten replicated experiments aimed at detecting 5 pg μL^{-1} solutions of WT and G12D non-amplified genomic DNAs in human plasma samples after 1000 s of the adsorption of conjugated AuNPs.

Table S1. $\Delta\%R_{PNA\ G12D}$, $\Delta\%R_{PNA\ WT}$ and $\Delta\%R_{PNA\ G12D}/\Delta\%R_{PNA\ WT}$ values obtained from three replicated experiments aimed at detecting 5 pg µL^{-1} solutions of WT and G12D non-amplified genomic DNAs after 1500 s of adsorption of conjugated AuNPs. The ratio considers SPRI responses (Δ%R) referred to the PNA G12D probe ($\Delta\%R_{PNA\ G12D}$) and the PNA WT probe ($\Delta\%R_{PNA\ WT}$), respectively when the same DNA target was detected. The mean $\Delta\%R_{PNA\ G12D}/\Delta\%R_{PNA\ WT}$ ratio value is reported in Fig. 23.

Sample	Δ%R PNA G12D at 1500 sec	Δ%R PNA WT at 1500 sec	Δ%R PNA G12D / Δ%R PNA WT
gDNA G12D	2.56	2.20	1.16
	7.38	7.32	1.01
	10.60	9.94	1.07
gDNA WT	7.56	9.96	0.76
	3.66	4.87	0.76
	11.08	13.57	0.82

Table S2. $\Delta\%R_{PNA\ G12V}$, $\Delta\%R_{PNA\ WT}$ and $\Delta\%R_{PNA\ G12V}/\Delta\%R_{PNA\ WT}$ values obtained from three replicated experiments aimed at detecting 5 pg µL^{-1} solutions of WT and G12V non-amplified genomic DNAs after 1500 s of adsorption of conjugated AuNPs. The ratio considers SPRI responses (Δ%R) referred to the PNA G12V probe ($\Delta\%R_{PNA\ G12V}$) and the PNA WT probe ($\Delta\%R_{PNA\ WT}$), respectively when the same DNA target was detected. The mean $\Delta\%R_{PNA\ G12V}/\Delta\%R_{PNA\ WT}$ ratio value is reported in Fig. 25.

Sample	Δ%R PNA G12V at 1500 sec	Δ%R PNA WT at 1500 sec	Δ%R PNA G12V / Δ%R PNA WT
gDNA G12V	10.56	9.67	1.09
	7.80	7.00	1.11
	10.29	9.15	1.12
gDNA WT	7.36	8.51	0.87
	7.43	8.03	0.93
	9.41	9.92	0.95

Table S3. $\Delta\%R_{\text{PNA G13D}}$, $\Delta\%R_{\text{PNA WT}}$ and $\Delta\%R_{\text{PNA G13D}}/\Delta\%R_{\text{PNA WT}}$ values obtained from three replicated experiments aimed at detecting 5 pg μL^{-1} solutions of WT and G13D non-amplified genomic DNAs after 1500 s of adsorption of conjugated AuNPs. The ratio considers SPRI responses (Δ%R) referred to the PNA G13D probe ($\Delta\%R_{\text{PNA G13D}}$) and the PNA WT probe ($\Delta\%R_{\text{PNA WT}}$), respectively when the same DNA target was detected. The mean $\Delta\%R_{\text{PNA G13D}}/\Delta\%R_{\text{PNA WT}}$ ratio value is reported in Fig. 27.

Sample	Δ%R PNA G13D at 1500 sec	Δ%R PNA WT at 1500 sec	Δ%R PNA G13D / Δ%R PNA WT
gDNA G13D	1.59	1.20	1.32
	3.22	2.57	1.25
	11.00	6.76	1.63
gDNA WT	2.41	2.60	0.93
	2.63	4.01	0.65
	9.24	9.80	0.94

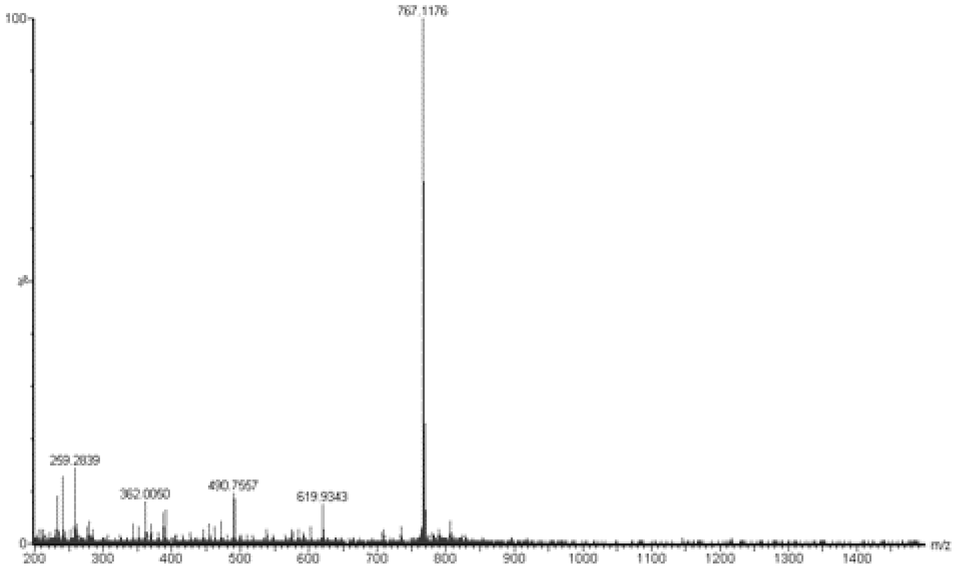

Figure S1. Mass spectrum of oligopeptide CEEEEE after purification, using 90 % Milli-Q water and 10 % acetonitrile.

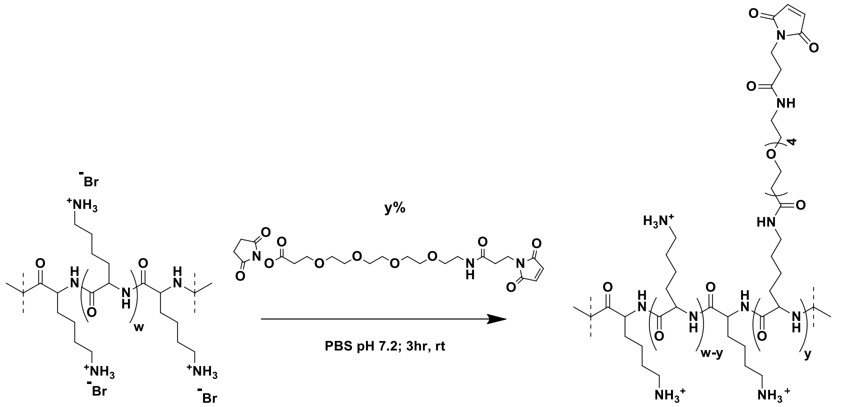

Figure S2. Scheme of PLL-mal(y%) synthesis.

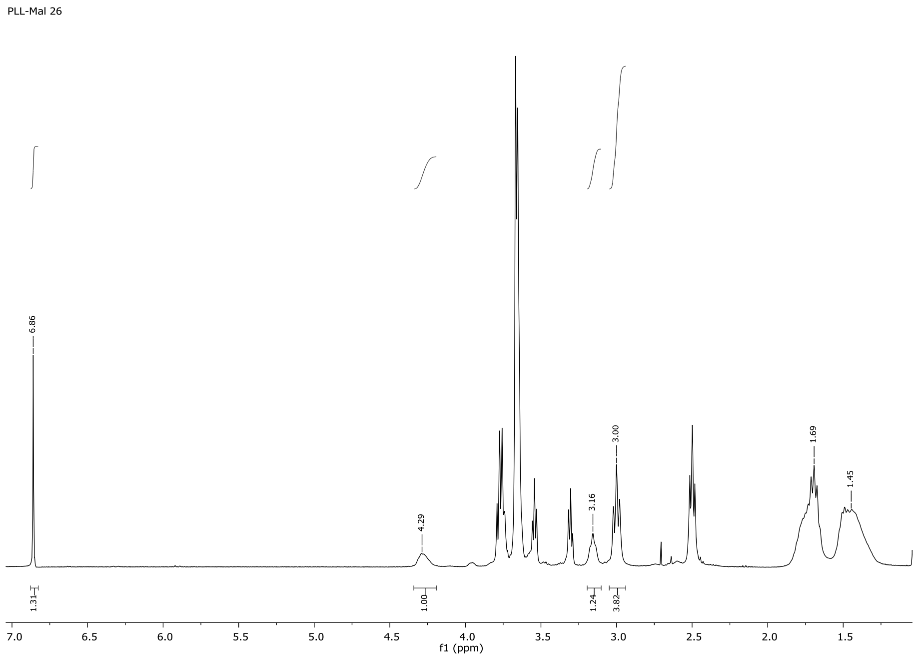

Figure S3. ^{1}H-NMR spectrum of PLL-mal(26%) after purification recorded on a Bruker 400 MHz spectrometer. Chemical shifts are reported in ppm with tetramethylsilane as an internal standard.

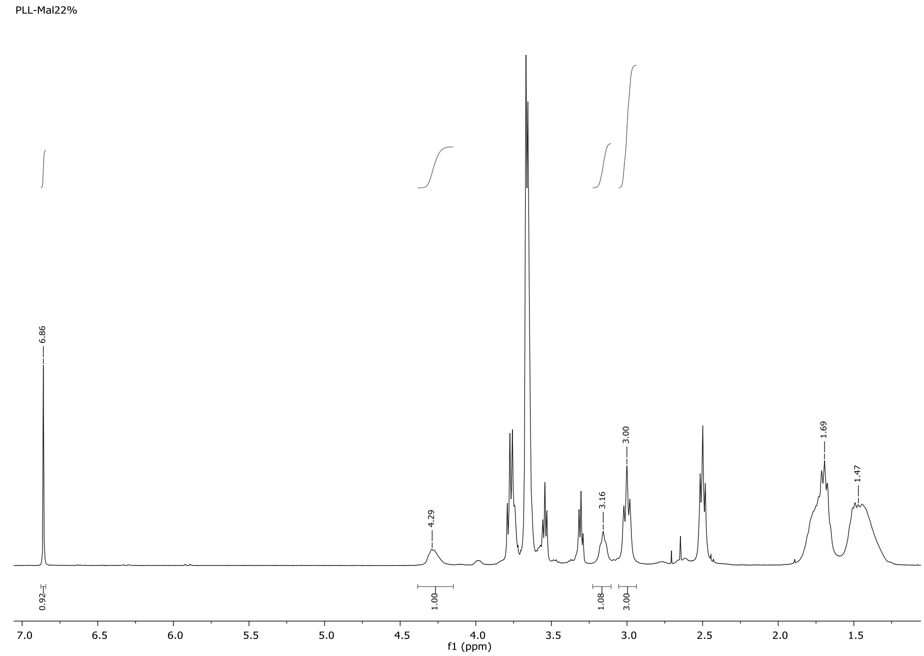

Figure S4. ^{1}H-NMR spectrum of PLL-mal(22%) after purification recorded on a Bruker 400 MHz spectrometer. Chemical shifts are reported in ppm with tetramethylsilane as an internal standard.

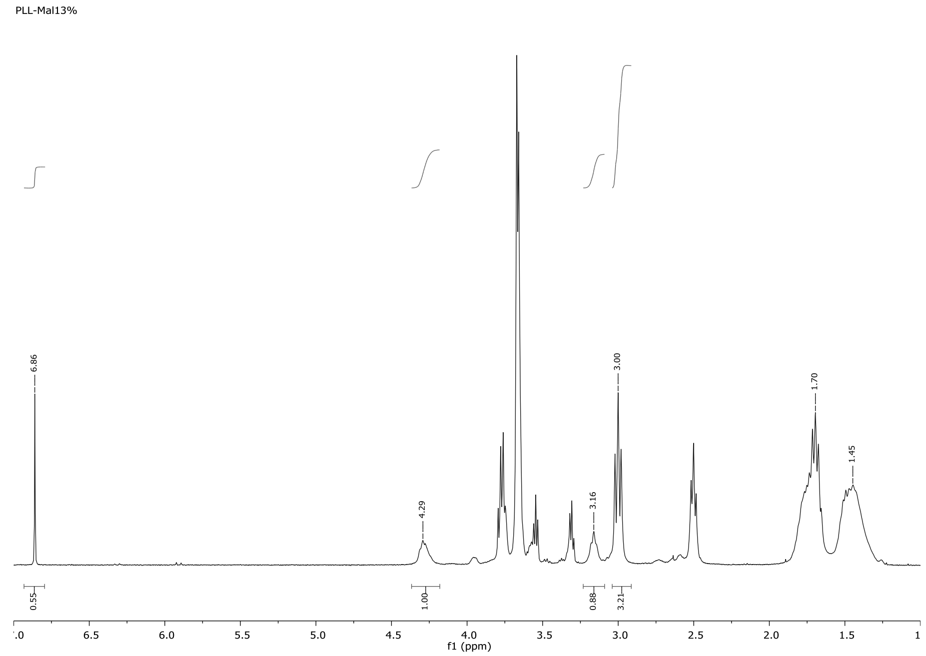

Figure S5. ^{1}H-NMR spectrum of PLL-mal(13%) after purification recorded on a Bruker 400 MHz spectrometer. Chemical shifts are reported in ppm with tetramethylsilane as an internal standard.

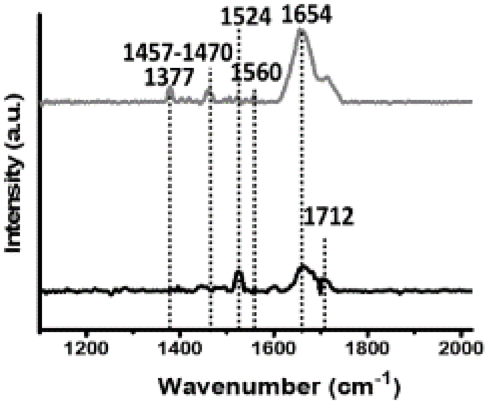

Figure S6. PM-IRRAS spectra of PLL–mal(22%) deposited on a gold chip (black line, bottom), and PLL-mal(22%)-CEEEEE (grey line, top) after the coupling reaction with CEEEEE.

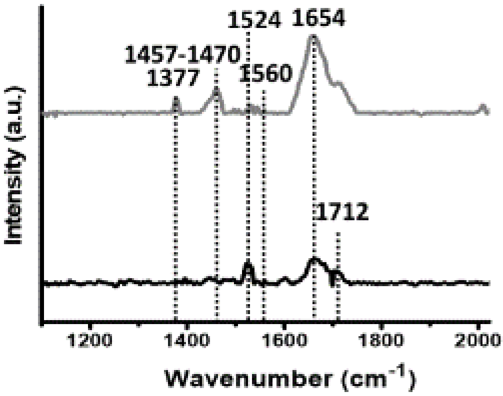

Figure S7. PM-IRRAS spectra of PLL–mal(13%) deposited on a gold chip (black line, bottom), and PLL-mal(13%)-CEEEEE (grey line, top) after the coupling reaction with CEEEEE.

Table S4. Surface coverage (ng cm^{-2}) of PLL-mal(26%), CEEEEE and molar ratio of CEEEEE to the PLL-mal(26%) for the evaluation of the coupling efficiency estimated by SPRI. Errors indicate the standard deviation of the data.

SPRI areal mass (ng cm^{-2})				
PLL-mal(26%)	**CEEEEE**	**mol CEEEEE/ mal(26%)**	**[BSA] 1.0 mg mL^{-1}**	**[BSA] 50.0 mg mL^{-1}**
138	282	2.4	9 ± 2	13 ± 2

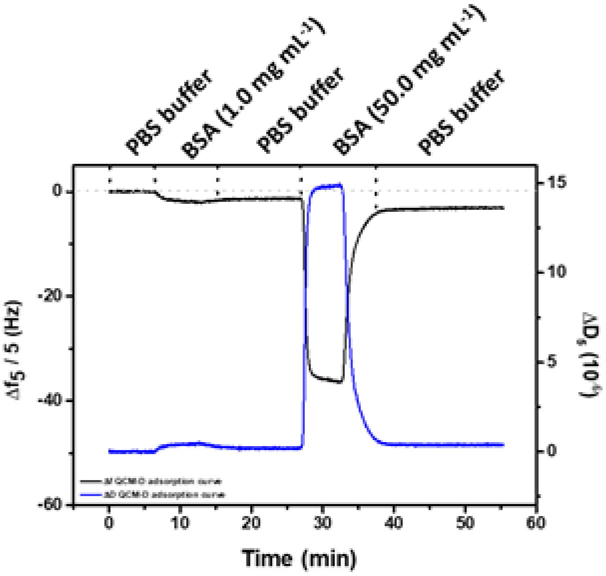

Figure S8. Surface coverage (ng cm^{-2}) of BSA adsorption on PLL-mal(26%)-CEEEEE silicon oxide surface measured by QCM-D. Frequency (blue line) and energy dissipation (black line) shifts corresponding to BSA adsorption are observed in QCM-D measurement (b).

Table S5. Surface coverage (ng cm^{-2}) of BSA adsorption on PLL-mal(26%)-CEEEEE silicon oxide surface measured by QCM-D on silicon oxide surface.

QCM-D areal mass (ng cm-2)	
[BSA] 1.0 mg mL^{-1}	**[BSA] 50.0 mg mL^{-1}**
24	55

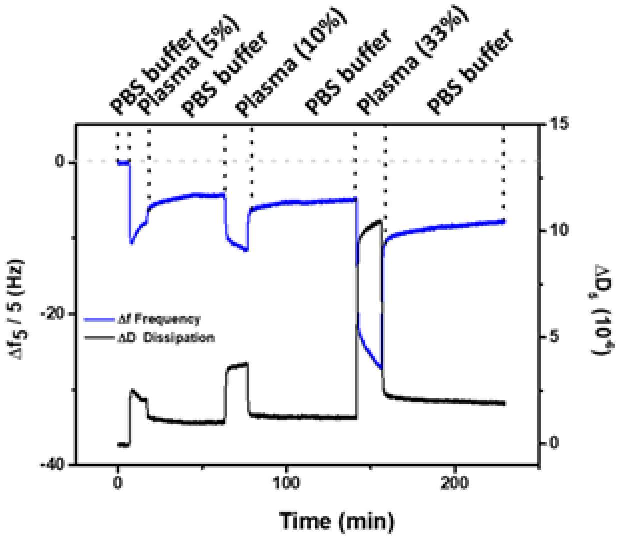

Figure S9. QCM-D antifouling tests using diluted human plasma samples and PLL-mal(26%)-CEEEEE on silicon oxide surface. Frequency (blue line) and energy dissipation (black line) shifts corresponding to the adsorption of protein from diluted human plasma samples are observed in QCM-D measurement.

Table S6. Surface coverages of protein (ng cm^{-2}) from diluted human plasma samples on PLL-mal(26%)-CEEEEE silicon oxide surface estimated by QCM-D.

Human plasma in PBS	QCM-D (ng cm^{-2})
5%	78
10%	88
33%	139

Table S7. $\Delta\%R_{PNA\ G12D}$, $\Delta\%R_{PNA\ WT}$ and $\Delta\%R_{PNA\ G12D}/\Delta\%R_{PNA\ WT}$ values obtained from ten replicated experiments aimed at detecting 5 pg µL^{-1} solutions of WT and G12D non-amplified genomic DNAs in human plasma samples after 1000 s of adsorption of conjugated AuNPs. The ratio considers SPRI responses (Δ%R) referred to the PNA G12D probe ($\Delta\%R_{PNA\ G12D}$) and the PNA WT probe ($\Delta\%R_{PNA\ WT}$), respectively when the same DNA target was detected. The mean $\Delta\%R_{PNA\ G12D}/\Delta\%R_{PNA\ WT}$ ratio value is reported in Fig. 39.

Sample	Δ%R PNA G12D / Δ%R PNA WT	Sample	Δ%R PNA G12D / Δ%R PNA WT
gDNA G12D	1.21	**gDNA WT**	0.96
	-		0.93
	1.02		0.90
	1.02		0.93
	1.05		0.88
	1.22 1.77		0.89
	1.24 1.54		0.70
	1.08		0.86
	1.45 1.12		0.73
	1.25 1.17		-